sid.inpe.br/mtc-m21c/2022/01.04.19.58-TDI

TURBULENCE AND MAGNETIC FIELDS IN INTERSTELLAR REGIONS

Lorena do Carmo Jesus

Doctorate Thesis of the Graduate Course in Astrophysics, guided by Dr. Diego Antonio Falceta Gonçalves, approved in January 19, 2022.

URL of the original document:
<http://urlib.net/8JMKD3MGP3W34R/465F7R8>

INPE
São José dos Campos
2022

PUBLISHED BY:

Instituto Nacional de Pesquisas Espaciais - INPE
Coordenação de Ensino, Pesquisa e Extensão (COEPE)
Divisão de Biblioteca (DIBIB)
CEP 12.227-010
São José dos Campos - SP - Brasil
Tel.:(012) 3208-6923/7348
E-mail: pubtc@inpe.br

sid.inpe.br/mtc-m21c/2022/01.04.19.58-TDI

TURBULENCE AND MAGNETIC FIELDS IN INTERSTELLAR REGIONS

Lorena do Carmo Jesus

Doctorate Thesis of the Graduate Course in Astrophysics, guided by Dr. Diego Antonio Falceta Gonçalves, approved in January 19, 2022.

URL of the original document:
<http://urlib.net/8JMKD3MGP3W34R/465F7R8>

INPE
São José dos Campos
2022

Cataloging in Publication Data

Jesus, Lorena do Carmo.

J499t Turbulence and magnetic fields in interstellar regions / Lorena do Carmo Jesus. – São José dos Campos : INPE, 2022.
xviii + 126 p. ; (sid.inpe.br/mtc-m21c/2022/01.04.19.58-TDI)

Thesis (Doctorate in Astrophysics) – Instituto Nacional de Pesquisas Espaciais, São José dos Campos, 2022.
Guiding : Dr. Diego Antonio Falceta Gonçalves.

1. MHD turbulence. 2. Interstellar medium. 3. Polarization. 4. MHD simulation. 5. Statistics. I.Title.

CDU 524:537.84

MINISTÉRIO DA CIÊNCIA, TECNOLOGIA E INOVAÇÕES

INSTITUTO NACIONAL DE PESQUISAS ESPACIAIS
Serviço de Pós-Graduação - SEPGR

DEFESA FINAL DE TESE DE LORENA DO CARMO JESUS
BANCA Nº 003/2022, REG 130060/2016

No dia 19 de janeiro de 2022, as 14h, por teleconferência, o(a) aluno(a) mencionado(a) acima defendeu seu trabalho final (apresentação oral seguida de arguição) perante uma Banca Examinadora, cujos membros estão listados abaixo. O(A) aluno(a) foi APROVADO(A) pela Banca Examinadora, por unanimidade, em cumprimento ao requisito exigido para obtenção do Título de Doutora em Astrofísica. O trabalho precisa da incorporação das correções sugeridas pela Banca e revisão final pelo(s) orientador (es).

Título: "TURBULENCE AND MAGNETIC FIELDS IN INTERSTELLAR REGIONS**"**

Membros da Banca:

Dr. Francisco José Jablonski - Presidente - INPE
Dr. Diego Antonio Falceta Gonçalves - Orientador - USP
Dr. Oswaldo Duarte Miranda - Membro Interno - INPE
Dr. Carlos Alexandre Wuensche De Souza - Membro Interno - INPE
Dr. Grzegorz Kowal - Membro Externo - USP/EAH
Dr. Gabriel Armando Pellegatti Franco - UFMG/IF

Declaração de aprovação do Dr. Grzegorz Kowal anexa (9302228)

Documento assinado eletronicamente por **Diego antonio falceta goncalves (E)**, **Usuário Externo**, em 01/02/2022, às 13:58 (horário oficial de Brasília), com fundamento no § 3º do art. 4º do Decreto nº 10.543, de 13 de novembro de 2020.

Documento assinado eletronicamente por **Oswaldo Duarte Miranda**, **Coordenador do Gabinete do Instituto Nacional de Pesquisas Espaciais**, em 03/02/2022, às 17:52 (horário oficial de Brasília), com fundamento no § 3º do art. 4º do Decreto nº 10.543, de 13 de novembro de 2020.

Documento assinado eletronicamente por **Francisco Jose Jablonksi**, **Pesquisador**, em 04/02/2022, às 12:44 (horário oficial de Brasília), com fundamento no § 3º do art. 4º do Decreto nº 10.543, de 13 de novembro de 2020.

Documento assinado eletronicamente por **Carlos Alexandre Wuensche de Souza**, **Chefe da Divisão de Astrofísica**, em 08/02/2022, às 09:19 (horário oficial de Brasília), com fundamento no § 3º do art. 4º do Decreto nº 10.543, de 13 de novembro de 2020.

Documento assinado eletronicamente por **Gabriel armando pellegatti franco (E)**, **Usuário Externo**, em 11/02/2022, às 19:46 (horário oficial de Brasília), com fundamento no § 3º do art. 4º do Decreto nº 10.543, de 13 de novembro de 2020.

A autenticidade deste documento pode ser conferida no site http://sei.mctic.gov.br/verifica.html, informando o código verificador **8984055** e o código CRC **BF40CD30**.

Referência: Processo nº 01340.000031/2022-96 SEI nº 8984055

ACKNOWLEDGEMENTS

First, I would like to thank my supervisor Diego Falceta Gonçalves for all the help and support throughout my PhD. Thank you for all your patience and kindness. Also, my sincere thanks to Dr Lazarian's group at Wisconsin Madison University, specially to Dr Zhang and Dr Casanova for all their teaching and support in research.

To the best parents in the world, Claudete and Luiz, for supporting me in every moment, encouraging me to pursue my dreams, for all the advises and care. They are my absolute foundation in life. Also, my brother Andre and my niece Anna. I love you guys so much.

To my husband Mateus, without you this work would not be possible, you made me a stronger person. I have grown professionally and personally with you in every moment in my life that we have spent together. I couldn't be more grateful.

In memoriam of my best friend and research collaborator, Ivan Ferreira Soares, who passed away in the last year of my PhD. I thought I couldn't bear to finish this thesis with all the sadness I had to carry inside me after you left. You were the purest heart I ever met. I will never be the same without you.

To Dr Francisco Jablonski, my very dear friend, research collaborator, for your teaching, support, insightful conversations and kindness, without which this work would not have been possible. You are an amazing human being, I have no words that can describe how grateful I am for everything. I wish wines and happiness.

To all INPE employees, students and staff, especially to my classmates Eunice, Aysses and Isabel, Rodrigo, German, Ana and Manuel for all the hours of studies spent together, laughs, dancing lessons, beers, ice creams, to all the good and bad moments shared together inside and outside the Institute and for sharing the same love for astrophysics and wines. You guys are family to me. I would like to thank professors José Carlos, Flávio D'Amico, Alex, Milone, Oswaldo, Odylio, João Braga, Chico and Claudia Vilega. Also, I would like to thank Cesinha and Reitano for being so kind to me. I was almost saying that Palmeiras is my favorite football team because of you, Reitano. Almost.

Finally, special thanks to CAPES, for funding and investing in Science students who like me, are pursuing their dreams.

ABSTRACT

Magnetic fields and turbulence are ubiquitous in the interstellar medium and several astrophysical processes. However, despite the importance of magnetized turbulence, a full theoretical framework remains unavailable. Observations provide only limited line-of-sight information on densities, temperatures, velocities and magnetic field strengths and, therefore, understanding astrophysical turbulence is challenging. In addition, based on the recent discovery of the use of intensity and synchrotron polarization gradient vectors to obtain the morphology of the magnetic field, this thesis presents a new way to acquire information: the level of magnetization in different astrophysical environments. In order to perform that, we use magnetohydrodynamic, isothermal simulations of turbulence, with Alfvénic Mach numbers of $M_A \in [0.2, 1.7]$. From these numerical data, we generate synchrotron maps and two methods, named Top-Base and circular statistics, were applied to the distributions of polarization and intensity gradient angles. In addition, using an error analysis on the synthetic data via Bayesian statistics, both methods were analyzed under different conditions, such as: signal-to-noise ratio of the data, influence of the Faraday rotation effect, different measurements of the projection in the line-of-sight with respect to the magnetic field. The error analysis showed that the Top-Base method is not suitable for signal-to-noise ratios S/R $\lesssim 15$. For the circular statistics method, the determination of M_A can be applied down to S/R ~ 5. The Faraday rotation effect was also considered for different frequencies, showing an efficiency of both methods even for regions where the Faraday depolarization is intense. We also studied the effect of the line-of-sight projection in different configurations and obtained that M_A can be successfully recovered. We conclude that the new techniques can successfully reconstruct the magnetization level for different astronomical observations. This work opens an avenue for applying our new techniques to synchrotron data cubes and a large number of forthcoming data sets from diferent radiotelescopes, such as: Low-Frequency Array for Radio astronomy (LOFAR), the Square Kilometer Array (SKA) and the Five-hundred-meter Aperture Spherical radio Telescope (FAST).

Keywords: MHD turbulence. Interstellar medium. Polarization. MHD simulation. Statistics.

TURBULÊNCIA E CAMPOS MAGNÉTICOS EM REGIÕES INTERSTELARES

RESUMO

O efeito de turbulência e a existência de campos magnéticos são onipresentes no meio interestelar e em diversos processos astrofísicos. Entretanto, apesar de sua importância, uma teoria capaz de explicar as propriedades da turbulência magnetizada continua inexistente. Além disso, as observações astronômicas fornecem apenas informações limitadas sobre densidades, temperaturas, velocidades e intensidades do campo magnético projetados na linha de visada, o que torna a compreensão de turbulência magnetohidrodinâmica no contexto astrofísico ainda mais desafiadora. Baseada na recente descoberta da utilização dos vetores gradiente de intensidade e gradiente de polarização síncrotron para obter a morfologia do campo magnético, esta tese apresenta um novo modo de determinar o nível de magnetização em diferentes ambientes astrofísicos. Para isso, nós utilizamos simulações numéricas magnetohidrodinâmicas tridimensionais, turbulentas, apresentando os casos sub e super-Alfvénicos, com números Alfvénicos de Mach $M_A \in [0.2, 1.7]$. A partir dos resultados númericos, nós construímos mapas sintéticos síncrotron e dois métodos conhecidos como Top-Base e estatística circular foram aplicados às distribuições dos ângulos dos gradientes de polarização e intensidade. Além disso, utizando uma análise de erros via estatística bayesiana, ambos os métodos foram analisados em diferentes condições observacionais, tais como: relação sinal/ruido dos dados, influência do efeito de rotação Faraday, diferentes medidas de projeção da linha de visada com respeito ao campo magnético. Em relação à análise de erros, o método de Top-Base não é adequado para razões de sinal-ruído S/R $\lesssim 15$. Para o método de estatística circular, a obtenção de M_A é viável à razões sinal/ruído até S/R ~ 5. Em nossa análise, o efeito de rotação de Faraday foi considerado para diferentes frequências, apresentando uma eficiência de ambos os métodos mesmo para regiões onde a depolarizações de Faraday é intensa. Também analisamos o efeito de diferentes linhas de visadas com relação ao campo magnético médio e, para as diferentes configurações, ambas técnicas foram bem sucedidas. A partir destes resultados, pode-se concluir as novas técnicas propostas nesta tese podem reconstruir com sucesso o nível de magnetização para diferentes observações astronômicas. Este trabalho abre um caminho para a aplicação de nossas novas técnicas a cubos de dados síncrotron provenientes de diferentes facilidades observacionais, tais como: o Low-Frequency Array for Radio astronomy (LOFAR), o Square Kilometer Array (SKA), e o Five-hundred-meter Aperture Spherical radio Telescope (FAST), entre outros.

Palavras-chave: Turbulência magnetohidrodinâmica. Meio Interestelar. Polarização. Simulações numéricas. Estatística. Flutuações síncrontron.

LIST OF FIGURES

Page

LIST OF TABLES

Page

CONTENTS

Page

1 INTRODUCTION

Turbulence has been inferred as ubiquitous in the interstellar medium since the 1950's (WEIZSÄCKER, 1951a). The presence of complex density structures observed on different astrophysical environments resembles the same characteristics from chaotic motions in turbulent flows (JACKSON et al., 2003). In addition, many spectroscopic measurements of velocity dispersion in the local Universe reveal the Alfvénic nature of the turbulent motions (HOERNER, 1957). Thenceforward, turbulence is considered the most common state for many astrophysical processes, such as: transport of mass and angular momentum, star formation, fragmentation of molecular clouds, heat and cosmic ray transport, magnetic reconnection, accretion disks, stellar winds, the interstellar medium and intercluster medium, among others (see Elmegreen and Scalo (2004) for a review).

Turbulence is characterized by chaotic motions which lead to diffusion of matter and dissipation of kinetic energy. Consequently, the long-term deterministic local properties are modeled stochastically (LANDAU; LIFSHITZ, 1959). In addition, most of the turbulence studies concerned with non-conductive fluids, can described by the Navier-Stokes equations. Under the assumptions of homogeneity, isotropy, scale invariance and locality, Kolmogorov provided one of the fundamental theoretical bases to study the dynamics of incompressible and unmagnetized fluids. That work opened an avenue to characterize many properties of a turbulent fluid (KOLMOGOROV, 1941).

However, even with the advance with Kolmogorov's model of incompressible turbulence and its widespread applications, the complete comprehension of these phenomena remains perhaps one of the greatest unsolved problems of classical physics. Komolgorov's assumptions are not strictly suitable for a number of astrophysical fluids, given that most astronomical observations show that the Universe is composed by compressible and magnetized plasmas, demanding a new understanding of its physics. Different interstellar and star formation regions present highly compressible flows, with magnetic fields embedded in them. For example, our Galaxy is modeled as a superposition of regular and random magnetic field components. The regular field follows a large-scale spiral structure in the plane of the galactic disk, extending to higher latitudes out to the galactic halo. The random field is a complex component of the locally disturbed field, commonly present in molecular clouds and star forming regions. Overall, the magnetic field is considered a key ingredient to characterize the dynamics of the gas in those regions (KLESSEN, 2011).

Magnetized astrophysical flows are usually described as a magnetohydrodynamical (MHD) plasma. This new scenario deeply changes the physics of the problem and a robust theoretical model that fully describes magnetohydrodynamical turbulence is still not available. This is because astrophysical MHD turbulence is a complex nonlinear phenomenon that can occur in a multiphase medium with many energy injection sources. In addition, the Reynolds numbers of the astrophysical turbulence are typically very high, with a wide range of density and velocity, owing to astrophysical scales which are enormous compared to dissipative scales. For example, the turbulence in warm diffuse interstellar medium is usually is transonic, with nonthermal motions being $\sim 10\ km.s^{-1}$, densities around $0.02 - 0.4\ cm^{-3}$ and $Re \sim 500 - 1000$ (HILL et al., 2008). While in molecular clouds, the turbulence is highly supersonic, with Reynolds number reaching $\sim 10^7$, nonthermal motions of $\sim 10\ km.s^{-1}$ and densities around $10^2 - 10^4\ cm^{-3}$ (ORKISZ et al., 2017). It can be seen the huge difference on the turbulence properties in both regions. This is also observed in others astrophysical environments, which shows the turbulence not only difficult to be modeled, but also how its formation forms such different regions.

Conversely, even with the lack of information regarding this physical process, it is well accepted nowadays that turbulence is one of the dominant dynamical processes governing the structure and evolution of different phases of the interstellar medium and and important ingredient for many astrophysical processes, such as: galaxy evolution (*e.g.,* Mo et al. (2010)); transport of mass and angular momentum, star formation; fragmentation of molecular clouds (McKee and Ostriker (2007)); heat and cosmic ray transport (*e.g.,* Lazarian and Pogosyan (2006)), among others.

The best approach, which provided an outstanding progress in establishing an astrophysical turbulence framework, is the synergy combining theoretical knowledge, numerical simulations, and observational data via statistical studies. These combined provide important insights to such a complex scenario. It is important to notice that even though numerical simulations have undertaken improvements in terms of both resolution and ability to simulate the wide range of physics found in the interstellar medium, they are still not able to describe the regimes of Reynolds numbers and the dynamical range of the variables seen in such regions. However, even with limitations, this approach is still one of the best avenues for researchers to understand the nature of magnetized turbulence.

The main observational techniques used to study MHD turbulence are based on column densities and line velocities. These quantities can give insights on the energy

transport over different scales. However, despite the power spectrum being an useful tool, it does not provide a full description of the turbulence properties and the use of different statistical tools is necessary to obtain more information the complex scenarios involved. This can be understood by the role of projection effects and the lack of phase information, an important quantity for the complete description in Fourier space (BURKHART; LAZARIAN, 2011).

The use of statistical tools applied to both observations and synthetic numerical simulations helps to constrain appropriately the physical conditions of the problem. For instance, it is well established that MHD turbulence can be separately studied in terms of some physical parameters, such as: the sonic Mach number (M_S), important parameter to understand compressibility, defined as the ratio between the thermal velocity and turbulent velocity and the Alfvénic Mach number (M_A), the ratio of the thermal pressure to the magnetic pressure. Nowadays, the few available analytical models for MHD turbulence can be applied only to particular cases or ranges of these parameters. In this context, the numerical simulations help to understand which analytical model is suitable for the different astrophysical turbulence conditions. Statistical tools can provide additional information on the properties of the turbulent medium, such as the sonic and Alfvénic Mach numbers. They include the Delta Variance Analysis (STUTZKI et al., 1998; OSSENKOPF et al., 2008), Principal Component Analysis (HEYER; SCHLOERB, 1997; HEYER et al., 2008; CORREIA et al., 2016; ENSOR et al., 2017), Probability Density Functions (PDF), including the Tsallis variant (FEDERRATH et al., 2008; BURKHART; LAZARIAN, 2012; GONZÁLEZ-CASANOVA et al., 2018), the bispectrum (BURKHART et al., 2009), and topological techniques, such as: Genus (CHEPURNOV et al., 2008), the Velocity Channel Analysis (VCA), the Velocity Coordinates Spectrum (VCS) (LAZARIAN; POGOSYAN, 2004; LAZARIAN; POGOSYAN, 2006; LAZARIAN; POGOSYAN, 2012), among others.

Another important aspect regarding interstellar turbulence is understanding how the magnetic field can affect its properties. Measurements that can extract information about this quantity are: the Stokes parameters of the diffuse polarized synchrotron emission (*e.g.*, Kothes et al. (2010) Wolleben et al. (2010) and Mao et al. (2014)), optical starlight polarization (*e.g.*, Heiles (1996), Girart et al. (2006), Hull and Zhang (2019)), Zeeman splitting (*e.g.*, Bel and Leroy (1989), Crutcher et al. (1996) and Green et al. (2012)) and Faraday rotation towards background extragalactic polarized sources (*e.g*, Eck et al. (2011), Mao et al. (2012) and Wu et al. (2015)).

In particular, synchrotron fluctuations have also been explored to provide informa-

tion regarding the interstellar turbulence since this quantity presents robust statistical behavior (see Lazarian and Pogosyan (2012), Burkhart and Lazarian (2012) and Zhang et al. (2019)). Gaensler et al. (2011) also presented an outstanding work which shows the advantages of using polarization gradients, applied to the polarized galactic emission, to trace spatial patterns. Through comparisons made with numerical simulations, they demonstrate that turbulence in the warm-ionized medium has a relatively low sonic Mach number ($M_S < 2$). Similar quantities and studies were applied to infer conditions of the magneto-sonic turbulent medium, such as the generalized polarization gradient, the polarization directional derivative, the polarization directional curvature and the polarization wavelength derivative (HERRON et al., 2018b; HERRON et al., 2018a).

Another important entity which helps the understanding of the properties of astrophysical turbulence is the magnetic field structure. Techniques based on synchrotron analyses also have been successfully proposed to trace magnetic field orientation. These are based on the theoretical framework proposed by Lazarian and Pogosyan (2016) which states that Alfvén and slow MHD turbulence wave modes cascade the energy anisotropically. Consequently, synchrotron intensity and polarized intensity present gradients correlated with the direction of the magnetic field. Lazarian et al. (2017) tested numerically the efficiency of estimating the magnetic field direction using synchrotron intensity gradients and synchrotron polarization gradients. Both techniques are based on the same principle of the method introduced in González-Casanova and Lazarian (2017) for the velocity centroid known as the Velocity Gradient Technique (VGT).

VGT is a technique that can recover the magnetic field direction and strength in cold neutral regions from emission lines such those of HI and CO (**??**GONZÁLEZ-CASANOVA et al., 2019; HSIEH et al., 2019; HU et al., 2019c; HU et al., 2019b). Recently, González-Casanova and Lazarian (2019) showed that there is a good correspondence between the VGT technique and the dust polarization (from stellar polarimetry) in mapping the magnetic field direction in the whole galaxy. Soler et al. (2013) proposed the technique named as Histogram of Relative Orientations (HRO), which explores how the statistics of the relative orientations of the intensity gradients and magnetic fields change with column densities. The HRO technique is quite different from what was proposed by the VGT method. The VGT tool explores the point-wise statistics of the magnetic field and does not depend on additional polarization measurements, but on elements of the MHD theory. Hu et al. (2019a) compared the differences and advantages of using both techniques for different ISM conditions.

Synchrotron intensity and polarization gradients represent a new way to obtain information about the magnetic field in the magneto-sonic turbulent medium. These new techniques has been proved successful, providing information about the structure of the magnetic field. In particular, the use of these gradients produce estimates of the magnetic field geometry and intensity without the effects of Faraday rotation. Moreover, (LAZARIAN; YUEN, 2018) showed that considering Faraday depolarization, they can obtain the 3D distribution of the magnetic field in the emitting volume. By considering different observational frequencies, it was shown that synchrotron polarization gradients are capable of probing the magnetic field orientation at different distances from the observer, opening a way of producing 3D maps of magnetic fields in the Galaxy (see Ho et al. (2019)). In a comparison with other techniques such as Faraday Tomography, the synchrotron polarization gradients can infer the magnetic field properties using a smaller frequency range. This is due to the fact that the gradients are not subject to Faraday rotation (see Ho et al. (2019)).

This PhD thesis aims to study the properties of synchrotron gradients in order to find not only information about the magnetic fields, but also to explore correlations with other quantities that can provide direct information regarding the magnetization level in a magneto-ionic turbulent medium, such as the Alfénic Mach number. This parameter is extremely important to constrain the physics of the turbulence in the different scenarios on the interstellar medium. Several works have already produced results on estimating the Alfénic Mach number (see Tofflemire et al. (2011), Burkhart and Lazarian (2011), Maguire et al. (2020)), but they are based on indirect measurements. This stresses the improved sensitivity of the gradients statistical approach. In an effort to characterize the relevant parameters, we used different statistical analyses that can be applied to real observations as well. Under this general objective, we specifically intend to:

- Propose two methods (namely, the standard deviation method, and the top-based method) which are applied to synchrotron polarization and intensity measurements in order to retrieve the magnetization level of the large-scale magnetic field.
- Investigate the reliability of these methods for a range of values of signal-to-noise ratio, angular telescope resolution and magnetic field configuration projected in the line-of-sight.
- Finally, describe the influence of Faraday rotation on the methods considering different frequencies and telescope resolutions. Our study attests

that both techniques can be applied to the analysis of real observational data.

To achieve these goals, we will make use of a set of 3D, high-resolution MHD simulations for reconstruction of synthetic observable parameters. These techniques are based on simplified radiative transfer models applied to the data cubes generated in the simulations. Thus, in addition to a correlation study between the simulated parameters, we explore a synergistic study of the observable properties of these regions for comparison with real observational data. A more detailed description of the numerical simulation method is presented in the following chapters.

In terms of chapters, this thesis is divided as follows. In Chapter 2 we provide a general review on MHD theory and Alfvénic turbulence, presenting some fundamental concepts which provide a theoretical basis for the subjects explored later in the thesis. Chapter 3 presents an overview of observational information regarding interstellar magnetized turbulence and the advances in understanding its dynamics. Chapter 4 presents a brief review about how the 3D numerical MHD grid-based codes used in the thesis work, the initial setups and how the numerical quantities obtained can be scaled to physical units. Chapter 5 presents how the gradients and their orientation are numerically obtained, how the error bars on the analyses are estimated and how both statistical methods are applied in practice. Chapter 6 will present the correlation of the Top-Base and circular statistics with synchrotron intensity and polarization angles distributions and explore how different interstellar and physical conditions can influence in obtaining the Alfvénic Mach number for different magnetized regimes. Chapter 7 contains a general discussion of the results obtained and summarizes the main conclusions of this thesis and perspectives for future research on this field.

2 PLASMA PHYSICS AND TURBULENCE PHENOMENOLOGY

Plasma can be defined as a quasi-neutral gas with a large collection of charged and neutral particles that exhibit collective behavior (BELLAN, 2006). Almost all the different astrophysical environments that exist in the Universe are composed of plasma, including: stellar interiors and atmospheres of accretion discs around black holes, molecular clouds, supernovae, quasars, the interstellar medium, extragalactic jets and the gas in galaxy clusters and intracluster medium (GOOSSENS, 2003).

Many of these regions present a turbulent fluid behavior, with a high electrical conductivity and magnetic fields that pervade in different observed scales (BENZ, 2002). For such conditions, the MHD turbulence theory is essential to understand the different electromagnetic processes and phenomena (SOMOV, 2006). Turbulence can be defined as time-dependent, stochastic flow typically observed in fluids with low viscosity (BERESNYAK; LAZARIAN, 2019). Despite its complexity, researchers investigate turbulence because of its practical importance. The use of this theory to investigate the distinct regions of the Universe has been extremely important to obtain insights on their astrophysical properties (SCHEKOCHIHIN; COWLEY, 2007).

This chapter aims to present a general overview about MHD turbulence theory and some recent theoretical models used in the astrophysical context. However, in order to clarify the understanding of this subject, Section 2.1 will introduce a brief discussion of non-magnetized turbulent fluids. Hence, the basic characteristics of plasma physics and MHD theory will be presented on Section 2.2. Finally, Section 2.3 will introduce the phenomenology of MHD turbulence and the main recent theoretical frameworks used to comprehend the physics of astrophysical turbulence.

2.1 Non-magnetized fluids turbulence

Fluids can be defined as substances that when subjected to shear stress, defined as an internal tangential force per unit area, suffer a continuous deformation (LANDAU; LIFSHITZ, 1959). Their physical behavior differs from other states of matter, showing some unique characteristics, such as: viscosity (internal resistance of the fluid due to deformations caused by shear stress or tensile tension); thermal conductivity (transfer of heat capacity), mass diffusivity (gradient in the concentration of matter) (MCCOMB, 1990).

The mathematical description of macroscopic phenomena in a particular fluid is built under a number of assumptions. The first one is known as continuum hypothesis,

which considers the fluid as a continuous medium. Consequently, the local conservative properties of the fluid are volume-averaged, state functions, dependent on space and time coordinates (LEAL, 1980). In addition, there are some fundamental laws that can describe the dynamical state of these fluid quantities (TRITTON, 1988). For example, the momentum equation for incompressible fluids, determines the velocity field dynamics and the mass and transport properties, being expressed by:

$$\frac{\partial \mathbf{u}}{\partial t} + (\mathbf{u} \cdot \nabla)\,\mathbf{u} = \frac{\nabla P}{\rho} + \nu \nabla^2 \mathbf{u} + \mathbf{F}, \tag{2.1}$$

where $\mathbf{u}$ denotes the fluid velocity, ν represents the kinematic viscosity, P is the pressure and $\mathbf{F}$ expresses the fluid acceleration.

One can observe the complexity of obtaining exact solutions for Equation (2.1). This partial differential equation can be solved for suitable forms of the right hand term, specially due to the nonlinear term (advection term). In order to extract physical information from the Navier-Stokes equation additional assumptions must be considered. Another useful approximation is to assume that the perturbations are self-similar. Self-similarity implies that given the scaling transformation of flow fluid physical variables, the governing equation remains invariant (MATHIEU; SCOTT, 2000). For that purpose, we introduce the following transformation:

$$\mathbf{r} \to \frac{\mathbf{x}}{L_0}, \quad \mathbf{u} \to \frac{\mathbf{u}}{U_0}, \quad \nabla \to L_0 \nabla, \quad t \to \frac{t}{L_0/U_0}, \quad P \to \frac{P}{\rho U_0^2}, \quad \mathbf{F} \to \frac{\mathbf{F}}{F_0}. \tag{2.2}$$

where $\mathbf{r}$, $\mathbf{u}$, ∇, t P and $\mathbf{F}$ are now the non-dimensionalized quantities for length, flow velocity and pressure. Using this form, Navier-Stokes can be written as:

$$\frac{\partial \mathbf{u}}{\partial t} + (\mathbf{u} \cdot \nabla)\,\mathbf{u} = \frac{\nabla P}{\rho} + \frac{1}{Re} \nabla^2 \mathbf{u} + \mathbf{F}, \tag{2.3}$$

It is relevant to notice that the Navier-Stokes equation is important not only to describe how the flow circulation happens, since it presents terms that indicate the rate of temporal variation of $\mathbf{u}$, but also by expressing how some intrinsic properties of the material can influence the phenomenon of transport of the fluid. The second term on the left hand side is related to convection. Convection is a physical process that occurs in a flow of gas in which some property is transported by the ordered

motion of the flow. On the right hand side of the equation, the second term is related to the diffusion process. Diffusion is a physical process that occurs in a flow of gas in which some property is transported by the random motion of the molecules (HILLEBRANDT; KUPKA, 2009). In addition, there is a dimensionless quantity in Equation (2.3), known as the Reynolds number, expressed as:

$$Re = \frac{\rho U_0 L_0}{\nu} \equiv \frac{|\,(\mathbf{u}\cdot\nabla)\,\mathbf{u}\,|}{\nu\nabla^2\mathbf{u}}. \tag{2.4}$$

Equation (2.3) governs a general fluid, not specifying anything about turbulence and it is natural one not understand the relationship between the Navier-Stokes equation and this phenomenon. However, when we analyze the Reynolds number in terms of diffusivity and conductivity which act on different regimes, the intrinsic nature of the fluid is observed. A small value of Re corresponds to viscosity dominated flow, where perturbations are damped and the fluid exhibits laminar behavior. On the other hand, when the Reynolds number becomes sufficiently large ($Re \gg 1$), the non-linear term becomes dominant and the nonlinear interplay between scales of fluctuations occur faster than their decay resulting in more complicated structure (SRINIVASAN, 1967). The fluid physical quantities exhibit fluctuations that depend on the coordinates – position and time. These perturbations occur in both vector and scalar quantities that describe the fluid dynamics. When the perturbation evolves, the fluid becomes chaotic and unsteady and, consequently, turbulent regimes arise. This is an extraordinarily complicated process, which is still not fully understood, though many decades of intensive research made our knowledge on the field much clearer (LESIEUR, 1987).

It may be noted that even the most simplified mathematical description of this equation is not of trivial solution. Equation (2.1) is a non-linear and non-local expression. The incompressibility condition results in an infinite sound speed, and in an instantaneous propagation of any perturbation in the fluid. In addition, the nonlinear term in the Navier-Stokes equation introduces intrinsic effect of the turbulence, as nonlinearity generates instabilities and energy exchange between scales. This fact indicates the complexity of obtaining analytic solutions for the Navier-Stokes equations (LANDAU; LIFSHITZ, 1959). Despite these difficulties, some intrinsic characteristics of the fluid regime can be obtained when a statistical and stochastic approach is taken. The most famous is known as Kolmogorov's theory, which has been refined over the years, based on a series of initial hypotheses of energy transfer and energy cascade scales that dominate the fluid dynamic state and its physical properties,

where the phenomenon of turbulence occurs. In the next discussion, we will present a simplified idea of this famous theory.

Kolmogorov Turbulence

Kolmogorov (1941) described the Navier-Stokes equations considering $\mathbf{u}(\mathbf{x}, \mathbf{t})$ a stochastic distribution. Under the assumptions of homogeneity, isotropy, scale invariance and locality, Kolmogorov stated that energy injected into a three-dimensional (3D) turbulent flow, at a constant rate ϵ, would form eddies at large scale, L. These eddies break up into smaller eddies, due to the nonlinear term of the Navier-Stokes equation, thereby transferring their energy to smaller scales. This process continues until a length scale η is reached at which viscous dissipation dominates (FRISCH, 1995). At the equilibrium state, the energy dissipation rate would be equal to the injection one, therefore the transfer rate between scales must be constant, i.e. equal to ϵ.

Kolmogorov assumed that the instabilities formed in turbulent regimes drive local vorticities and large amplitude eddy fragments into smaller ones, creating a turbulent pattern. This concept was initially imagined by Richardson (1922) and mathematically described by Kolmogorov. One of the key arguments in this interpretation is the consideration that the energy transfer rate (ε) is constant and can be defined as: $\varepsilon = \left(\frac{\delta u_l}{\tau_l}\right)^{1/4}$, where δu_l is the velocity fluctuation amplitude at lengthscale l, and τ_l is the dynamical timescale for the energy transfer. Using this interpretation, the physical properties of the turbulence can be modeled with scaling laws and a well defined power spectrum (CHORIN, 1975). Kolmogorov derived the one-dimension velocity field spectrum with the following expression:

$$P_u(k) \propto \varepsilon^{2/3} k^{-5/3}, \tag{2.5}$$

where $k = \frac{2\pi}{\lambda}$ is the wavenumber, defined as the spatial frequency in the Fourier space. The locality assumption is what ensures that these wave perturbations can be defined at the local Fourier space. Also, the wavenumbers in Kolmogorov's interpretation, i.e, the wave interactions that generate the eddy cascade, should follow a well defined selection rule in which the large scale eddy k_1 decays into smaller eddies k_2, using the following form: $k_2 = 2k_1$.

Figure 2.1 - Illustration of turbulence energy wavenumber power spectrum.

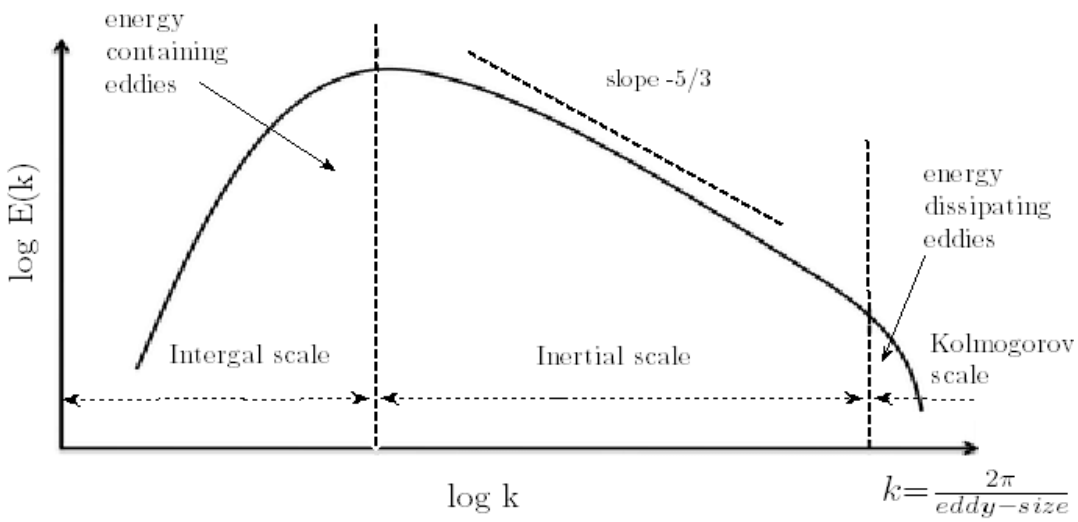

SOURCE: Frisch (1995).

The energy power spectrum proposed by Kolmogorov (1941) is shown in Figure 2.1. It can be seen that the first scale range, named integral range, is related to the largest scale that is the size of the domain of the problem, L. From this scale a characteristic velocity (which is the mean velocity u, used to define the large-scale Reynolds number) is derived. Furthermore, the largest motions (or eddies) produced in turbulence contain most of the kinetic energy, whereas the smallest eddies are responsible for the viscous dissipation of turbulent kinetic energy. The regime in which the turbulence velocity perturbations present a constant energy transfer rate is known as inertial range of scales, and is observed between the energy injection and the viscous damping scales (DAVIDSON, 2004). In this intermediate range, since the energy transfer is constant, the power spectrum can be expressed the same way as presented in Equation 2.5. The lower limit scale in Kolmogorov's spectrum is defined as: $\eta = (\nu/\epsilon)^{1/4}$, where ϵ is the kinetic energy dissipation rate by heat due to the effects of the viscosity ν on the fluid.

In addition, the theory also predicts the scaling laws for the moments of velocity spatial increments, known as velocity structure functions. They are consequence of the small-scale homogeneity assumption and self- similarity assumption, which imply that the physical properties do not change under a spatial translation operator and the fact that the small scales are associated with lengthscales much smaller than

the overall scale, often identified as the wavenumber corresponding to maximum energy. Consequently, the velocity increments can be expressed in term of structure functions. Kolmogorov also defined that this statistical function presents scaling laws that depend on the spatial increment vector and the energy transfer dissipation:

$$S_p = \langle [\mathbf{u}(\mathbf{x}+\mathbf{r},t) - \mathbf{u}(\mathbf{x},t)]^{\frac{p}{3}} \rangle \propto (\varepsilon l)^{\frac{p}{3}}, \tag{2.6}$$

with p being a positive integer. Also, due to homogeneity, the structure functions depend only on the separation vector $\mathbf{l}$, while isotropy can be used to further simplify this dependence on the absolute value $l = |\mathbf{l}|$ (FRISCH, 1995).

The Kolmogorov theory of turbulence has been successful in reproducing many different instances and therefore presents a vast literature. In the astrophysical context, this impressive work and its evolution refinement over the years presented several developments. For example, the density distribution of some molecular clouds studied by Larson (1981) corroborated Kolmogorov's density predictions. Also, Armstrong et al. (1995) presented a density power spectrum with a single Kolmogorov slope ranging for more than 6 orders of magnitude in lengthscale. Some observations of the solar wind turbulence also corroborate the Kolmogorov scale in density and velocity fluctuation in large scales (*i.e.*, Bruno and Carbone (2013), Shaikh and Zank (2010), Ghosh and Matthaeus (1990) and Treumann et al. (2019).

Conversely, over the past decades, the improvement of observational techniques showed that the turbulent nature of the interstellar medium is way more complex than the basics assumptions of Kolmogorov. Initially, as it will be presented in more details on the next chapter, the interstellar medium is essentially composed by plasma and dust with a interstellar magnetic field pervading in many scales. In the presence of the interstellar magnetic fields, the turbulence cascade is quite different from that assumed by Kolmogorov (CRUTCHER et al., 1987; FALCETA-GONÇALVES et al., 2014). In this scenario, the eddies are compressed by the field lines in the perpendicular direction only. Consequently, turbulence in magnetized medium is anisotropic, with the anisotropy being larger at smaller scales. Also, Kolmogorov's scalings fail for compressible turbulence as the shocks formed in this regime also become responsible for energy exchange between scales, losing the locality condition. The specific energy transfer is not constant in a fluid element and depends not exclusively on its velocity but also on its density (FALCETA-GONÇALVES, 2011).

The use of numerical simulations to reproduce the different complex scenarios confirms so far that the velocity and density distributions (and topology) in the in-

terstellar medium can be understood, in almost all cases, as a result of supersonic Alfvénic turbulence. Since this thesis is devoted to obtain statistical tools to constrain the properties of the interstellar turbulence, the next section will be devoted to explain the basic characteristics of a plasma and therefore present an overview of MHD turbulence. For more information regarding Kolmogorov's theory, in which this section was based, see Falceta-Gonçalves (2011) and Monin et al. (1977).

2.2 Magnetohydrodynamic theory

Due to the strong interaction with the electromagnetic radiation field, astrophysical plasmas display a complexity in structure and motion that far exceed what is found in other states of matter. For the description of plasma phenomena, there are three theoretical approaches with several different choices of approximations, and the best description depends on what information is available. The first one is known as kinetic theory and takes into account the individual motion of all particles. One problem with this theoretical description is that the equations governing the evolution of the individual particles distribution function are extremely difficult to solve. In the kinetic theory, the statistical description is based on the momentum distribution function for the particles under consideration. The problem consists in solving the appropriate kinetic equations that govern the evolution of the distribution function in phase space. The second approach is called two-fluid (electrons and ions) theory and treats the plasma as a mixture of two or more interpenetrating fluids, depending on the number of different species considered. In addition to the electrodynamic equations, there is a set of coupled hydrodynamic equations that are considered, such as: conservation of mass, momentum, and energy for each particle species in the plasma.

Finally, the last approach consists in treating the whole plasma as a single conducting fluid, governed by fluid dynamics and Maxwell's equations. This theory is usually referred to as magnetohydrodynamics (MHD). The MHD equations are applicable to the study of very low frequency phenomena in highly conducting fluids immersed in magnetic fields. Since magnetic fields are ubiquitous in space, and their role affects almost all astrophysical processes, the description using the MHD theory is usually well accepted to describe magnetized phenomena. This section will introduce the main properties of the MHD approach, being important to understand the application of this theory in the context of the cosmic fields, and how it affects the dynamics and evolution of different interstellar media. For more comprehensive introductions to astrophysical MHD, see Parker (1983), Kulsrud (2004).

Magnetohydrodynamic equations

As mentioned previously, the MHD approach is based on the assumption that the plasma is a conductive fluid, without considering the individual nature of each species of particles. In this theory, the fluid approximation is also considered: the local thermodynamic quantities can be meaningfully defined in the plasma, and variations in these quantities are slow compared with the time scale of the microscopic processes in the plasma. This assumption involves the same approximation used in deriving the equations of fluid mechanics and thermodynamics in statistical physics. Also, the hydrodynamic equations obtained in the kinetic plasma theory are coupled with Maxwell's equations. In addition, MHD theory also assumes similar number of electrons and ions, therefore it can be approximated by one fluid, which is a mixture of these two. Hence, in order to provide the governing equations in MHD theory, the physical quantities are approximated as macroscopical average values per unit volume of the fluid.

Also, one important aspect in the MHD theory that should be highlighted is the variation in the dynamic properties of the fluid due to the presence of a magnetic field. For steady-state situations, or slowly varying conditions, the dynamic MHD equations are very consistent and, in many cases, lead to important results that would not be easily obtained from the individual equations for each particle species. Some astrophysical properties related to magnetic fields can be explained only by MHD approach, which again, emphasizes the importance of understanding this theory. In addition, due to the number of variables in an astrophysical environment, several simplifying approximations are usually considered, in order to eliminate some terms in the MHD equations. Otherwise, there would be no mathematical closure to the governing equations.

For this reason, the next discussion will present the equations for MHD theory in the ideal case, where the effects of viscosity, resistivity and diffusion are disregarded. The ideal MHD equations will also be considered on the numerical simulations used in this thesis. The first equations that will be presented are the well-know equations in electrodynamics: Maxwell's equations.

Maxwell equations in the ideal MHD theory

In the electromagnetic theory, the spatial and temporal variations of either the electromagnetic field or its source, the electric charge density and current density are specified by Maxwell's equations:

$$\nabla \cdot \mathbf{E} = \frac{\rho_m}{\epsilon_0}, \tag{2.7}$$

$$\nabla \cdot \mathbf{B} = 0, \tag{2.8}$$

$$\nabla \times \mathbf{E} = -\frac{\partial \mathbf{B}}{\partial t}, \tag{2.9}$$

$$\nabla \times \mathbf{B} = \mu_0 \mathbf{J} + \frac{1}{c^2}\frac{\partial \mathbf{E}}{\partial t}, \tag{2.10}$$

where $\mathbf{E}$ and $\mathbf{B}$ denote the electric and magnetic fields in a plasma; ρ_m denotes the electric charge density; $\mathbf{J}$ is the electric current density and μ_0 is the permissivity of the material. The first Equation (2.7) is called electric Gauss law and states that the electric flux through a closed surface is proportional to the total charge within that surface. Equation 2.8 is known as Gauss's law for magnetism and gives information about the magnetic flux. It states that the total magnetic flux through any closed surface is zero. This equation has a important geometrical meaning and can be considered as an initial condition for subsequent equations. The third equation is known as Faraday's law, which describes the relationship between electric and magnetic fields variations. The fundamental concept behind this law is that changing the magnetic flux through a surface induces an electromotive force trough the same. The last equation is called Ampère's law and states that the magnetic field induced around a closed system is proportional to the electric current plus displacement current (rate of change of electric field) that the system encloses.

2.2.1 Generalized Ohm's law

In order to connect the electromagnetic quantities with the typical variables found in a fluid, Ohm's law is extremely important in the MHD theoretical formulation. In the approximation of ideal plasma as a conducting fluid, the generalized expression for Ohm's law can be written as (BOYD; SANDERSO, 2003):

$$\mathbf{E} + \mathbf{u} \times \mathbf{B} - \frac{\mathbf{J}}{\sigma} - \frac{1}{\sigma \nu_C}\frac{\partial \mathbf{J}}{\partial t} = \frac{m_i}{Ze\rho}\left(\mathbf{J} \times \mathbf{B} - \nabla P_e\right), \tag{2.11}$$

where σ denotes the conductivity, ν_C represents the electron collision frequency, m_i and Ze are respectively the ionic mass and charge and ∇P_e denotes the electronic pressure gradient.

In addition, our study via MHD simulations considers the simplest case, where the ideal MHD approximation is used. Therefore, as explained in this section, resistivity

effects are null and conductivity tends to infinity ($\sigma \to \infty$). Considering also the term related to null electronic pressure, one can rewrite Ohm's law for the ideal MHD case as:

$$\mathbf{E} + \mathbf{u} \times \mathbf{B} = 0 \tag{2.12}$$

This Equation is called idealized Ohm's law. Substituting the above expression in Equation (2.9), we obtain:

$$\frac{\partial \mathbf{B}}{\partial t} = \nabla \times (\mathbf{v} \times \mathbf{B}), \tag{2.13}$$

which is called induction equation.

Equation (2.13) describes how the magnetic field in a perfectly conducting fluid changes with time under the influence of a velocity field $\mathbf{v}$, evidencing the perfect coupling between the two physical quantities. This equation, together with the single transport fluid equations that will be presented in the next section, constitute the complete set of ideal MHD equations.

2.2.2 MHD Fluid transport equations

Using the approximation of the plasma as a single fluid, one can rewrite the fluid equations, considering the existent electromagnetic fields, in the following way:

- Ideal conservation of mass equation:

$$\frac{\partial \rho}{\partial t} + \nabla \cdot (\rho \mathbf{u}) = 0, \tag{2.14}$$

- Equation of motion describing the momentum evolution:

$$\frac{\partial}{\partial t}(\rho \mathbf{v}) + \nabla \cdot \left[\rho \mathbf{v}\mathbf{v} - \frac{1}{\mu_0}\mathbf{B}\mathbf{B} - \left(P + \frac{1}{2}\frac{B^2}{\mu_0} \right) \mathbf{I} \right] = \rho \mathbf{f}. \tag{2.15}$$

where $\mathbf{I}$ is Comparing the MHD fluid momentum equation with the momentum equation of a non-conducting fluid, one can note that there are additional terms. The first one is proportional to $\mathbf{BB}$ and describes a force due to the variation of magnetic field strength in the direction of the field. It is often called the magnetic curvature force, or tension. Also, the second term proportional to B^2 is related to

the magnetic pressure on the fluid. Equation (2.15), usually known as MHD Navier-Stokes equation, gives important informations regarding the peculiar properties of the magnetic field lines and magnetic pressure in the presence of a plasma fluid. The magnetic field in a conducting fluid acts somewhat like a deformable, elastic medium. Unlike an usual elastic medium, however, it is always under compression in two directions (perpendicular to the field) and under tension in the third (along the field lines), irrespective of the deformation. Also, using MHD Navier-Stokes equation, one can obtain that the magnetic field on the MHD plasma presents a tension that manifests itself more indirectly through the curvature of field lines.

- Ideal energy conservation equation

  For the MHD, the energy conservation equation may be quite complicated depending on the sources and energy loss processes that take place. A possible approximation for most cases is the adiabatic approximation:

$$\frac{d}{dt}\left(\frac{p}{\rho^{\gamma}}\right) = 0, \tag{2.16}$$

where p is the plasma pressure and γ the effective polytropic index, which for the case of mono-atomic gas, with no energy losses (or sources), resumes to the ratio of specific heats for an adiabatic equation of state ($\gamma = \frac{5}{3}$).

2.2.3 Linear waves in ideal MHD

It is crucial to examine the existence of wave modes in an ideal MHD fluid to understand the corresponding dynamics and the nature of the response created by the fluid after any external perturbations with respect to a steady state flow happen. In fact, there are many kinds of wave modes in plasma physics which depend on the frequency, species of oscillating particles, restoring force, boundary conditions, inhomogeneities, propagation angle with respect to the magnetic field, etc.

We have previously mentioned that the magnetic field of the ideal MHD plasma tangles the velocity field with the magnetic field lines, causing the plasma to be confined under a tension. Consequently, one of the possible modes of perturbation occurs when the plasma is slightly disturbed from the equilibrium conditions, causing the magnetic field lines to undergo transverse vibrations. This section gives a general overview for the particular case when the fluid motion and magnetic field line perturbations are perpendicular to the field lines. To study these conditions, we assume stationary ideal homogeneous conditions as the initial state of the single-fluid

plasma, with small perturbations in the mass density, thermal pressure, magnetic field and velocity field expressed as:

$$\rho = \rho_0 + \rho_1, \qquad p = p_0 + p_1, \qquad \mathbf{B} = \mathbf{B_0} + \mathbf{B_1}, \qquad \text{and} \quad \mathbf{u} = \mathbf{u_1}, \tag{2.17}$$

where the terms with subscript 0 denote the equilibrium quantities and those with subscript 1 correspond to the linear perturbations.

In order to obtain linear wave solutions for the small perturbations, we start with a linearization of the ideal MHD equations case using conditions (2.17) in Equations (2.14), (2.15) and (2.16):

$$\frac{\partial \rho_1}{\partial t} + \rho_0 \left[\nabla \cdot \mathbf{u_1}\right] = 0, \tag{2.18}$$

$$\rho_0 \frac{\partial \mathbf{u_1}}{\partial t} + \nabla p_1 - \frac{\nabla \times (\mathbf{B_1}) \times \mathbf{B_0}}{\mu_0} = 0, \tag{2.19}$$

$$\frac{\partial \mathbf{B_1}}{\partial t} = \nabla \times (\mathbf{u_1} \times \mathbf{B_1}), \tag{2.20}$$

$$\frac{\partial}{\partial t}\left(\frac{\rho_1}{\rho_0} - \frac{\gamma \rho_2}{\rho_0}\right) = 0. \tag{2.21}$$

Another important approximation introduced to obtain the above expressions stems from the fact that since only low frequency perturbations were considered, the cross-terms can be disregarded. Also, we can assume that all perturbed quantities vary like $\exp(-i\omega k + i\mathbf{k} \cdot \mathbf{r})$. Then, operations can be rewritten as:

$$\frac{\partial}{\partial t} \rightarrow -i\omega \quad \text{and} \qquad \nabla \rightarrow i\mathbf{k}. \tag{2.22}$$

Thus, by rewriting the operations as presented in (2.22), we obtain the following relations:

$$-\omega \rho_1 + \rho_0 \mathbf{k} \cdot \mathbf{v_1} = 0, \tag{2.23}$$

$$-\omega\rho_0\mathbf{u}_1 + \mathbf{k}p_1 - \frac{(\mathbf{k}\times\mathbf{B}_0)\,\mathbf{B_1}}{\mu_0} = 0, \tag{2.24}$$

$$\omega\mathbf{B}_1 + \mathbf{k}\times(\mathbf{u_1}\times\mathbf{B_0} + \mathbf{u_0}\times\mathbf{B_1}) = 0, \tag{2.25}$$

$$-\omega\left(\frac{\rho_1}{\rho_0} - \frac{\gamma\rho_1}{\rho_0}\right) = 0. \tag{2.26}$$

Assuming that $\omega \neq 0$, the above equations yield:

$$\rho_1 = \rho_0\frac{\mathbf{k}\cdot\mathbf{u_1}}{\omega}, \tag{2.27}$$

$$p_1 = \gamma p_0\frac{\mathbf{k}\cdot\mathbf{u_1}}{\omega}, \tag{2.28}$$

$$\mathbf{B}_1 = \frac{(\mathbf{k}\cdot\mathbf{u_1})\,\mathbf{B}_0 - (\mathbf{k}\cdot\mathbf{B_0})\,\mathbf{u_1}}{\omega}. \tag{2.29}$$

The substitution of expressions (2.27), (2.28) and (2.29) into the linearized equation of motion (2.24) results in the dispersion relation:

$$\left[\omega^2 - \frac{\mathbf{k}\cdot\mathbf{B_0}}{\mu_0\rho_0}\right]\mathbf{u_1} = \left\{\left[\frac{\gamma p_0}{\rho_0} + \frac{B_0^2}{\mu_0\rho_0}\right]\mathbf{k} - \frac{(\mathbf{k}\cdot\mathbf{B}_0)\,\mathbf{B}_0}{\mu_0\rho_0}\right\}(\mathbf{k}\cdot\mathbf{u}_1)\,. \tag{2.30}$$

Without losing generality, if we choose the equilibrium magnetic field in the z-direction component $\mathbf{B_0} = B_0\hat{\mathbf{e}}_\mathbf{z}$ and the vector $\mathbf{k} = k_x\hat{\mathbf{e}}_\mathbf{x} + k_y\hat{\mathbf{e}}_\mathbf{y}$ lies in the x-z plane, the relation (2.30) can be written in the following matrix form:

$$\begin{pmatrix} k^2v_a - k^2C_s^2\sin^2\theta & 0 & -k^2C_s^2\sin\theta\cos\theta \\ 0 & \omega^2 - k^2v_a\cos^2\theta & 0 \\ k^2C_s^2\sin\theta\cos\theta & 0 & \omega^2 - k^2c_s^2\cos^2\theta \end{pmatrix}\begin{pmatrix} u_x \\ u_y \\ u_z \end{pmatrix} = 0,$$

where $c_s = \sqrt{\frac{\gamma p_0}{\rho_0}}$ is the sound speed, θ is the angle between k AND $\mathbf{B}$ and v_A corresponds to the group velocity called Alfvén velocity, defined as:

$$v_A = \sqrt{\frac{B_0^2}{\mu_0 \rho_0}}. \tag{2.31}$$

In order to have non-trivial solutions for the equations, the determinant of the coefficients matrix should vanish. We therefore obtain the following dispersion relation:

$$\left(\omega^2 - k^2 v_A \cos\theta\right)\left[\omega^4 - \omega^2 k^2 \left(v_A^2 + c_s^2\right) + k^4 v_A^2 c_s^2 \cos\theta\right] = 0. \tag{2.32}$$

The solution of this equation admits three independent roots, corresponding to the different wave modes that can propagate through an MHD plasma:

$$\omega_A = \pm k v_A \cos\theta, \tag{2.33}$$

$$\omega_F = \pm\sqrt{\frac{k^2}{2}\left[(c_s^2 + v_A^2) + \sqrt{\left(v_A^2 + c_s^2\right)^2 - 4 v_A^2 c_s^2 \cos\theta}\right]}, \tag{2.34}$$

$$\omega_S = \pm\sqrt{\frac{k^2}{2}\left[(c_s^2 + v_A^2) - \sqrt{\left(v_A^2 + c_s^2\right)^2 - 4 v_A^2 c_s^2 \cos\theta}\right]}, \tag{2.35}$$

corresponding to the Alfvén mode, and the fast and slow magnetosonic modes, respectively.

The Alfvén mode is a transverse wave which involves movements in the plasma perpendicular to the magnetic field ($\mathbf{k} \perp \mathbf{u_1}$ and $\mathbf{u_1} \perp \mathbf{B_0}$). The other possible wave modes are known as fast and slow magnetoacoustic waves, occurring as velocity fluctuations occur along the magnetic field lines, but not parallel exclusively.

Regarding Alfvén mode waves, the studies of the dispersion relation can reveal some interesting properties: this type of plasma modes are incompressible in contrast with the other modes; also, the magnetic field amplitudes and the velocities are perpendicular to the direction of propagation, and all frequency perturbations propagate at the same speed. The wave mode perturbations are important to understand the phenomenology of the dynamics of the MHD turbulence, since highly non-linear perturbations on a plasma present Alfvénic nature. Before giving more details, it is important to introduce useful simplifications commonly used on MHD turbulence description, which are based on transforming the incompressible MHD equations,

by using variables which lead to a symmetrical form of these equations. The new variables are called Elsässer variables and will be explained on the next subsection.

2.2.4 Elsässer variables

Initially proposed by Elsasser (1950), these quantities can be interpreted as Alfvén wave perturbations propagating either in the direction (or opposite direction) of the background magnetic field, being defined as:

$$\mathbf{z}^{\pm} = \mathbf{u} \pm \frac{\mathbf{B}}{\sqrt{4\pi\rho}} \tag{2.36}$$

As shown in several studies of MHD turbulence, the transformation introduced by the use Elsässer fields provides a symmetrization of the MHD equations in terms of the perturbation along the magnetic field, and also allows the study of Alfvén perturbations, commonly found in the interstellar turbulence. The use of these variables on Elsasser (1950) was made by assuming incompressibility. However, it is well established that interstellar turbulence is highly compressible and inhomogeneous. As will be detailed on the next section, the presence of compressibility in MHD turbulence introduces new wave modes, *i.e.*, magnetoacoustic modes, which makes the study of MHD turbulence much more difficult, in comparison with the incompressible counterpart. However, Marsch and Mangeney (1987) showed that the compressible MHD equations (with a polytropic equation of state) can still be written in terms of generalized Elsässer variables, with variable density. Using the density and magnetic field in terms of Elsässer variables, the compressible MHD equations can be rewritten in terms of Alfvén velocity (2.31):

$$\frac{\partial ln\rho}{\partial t} + (\mathbf{v}\cdot\nabla)\, ln\rho = -\nabla\cdot\mathbf{v}, \tag{2.37}$$

$$\frac{\partial \mathbf{v}}{\partial t} + (\mathbf{v}\cdot\nabla)\,\mathbf{v} - (\mathbf{v_A}\cdot\nabla)\,\mathbf{v_A} = -\frac{\nabla p}{\rho} - \mathbf{v_A}\,(\mathbf{v_A}\cdot\nabla)\,, \tag{2.38}$$

$$\frac{\partial \mathbf{v}}{\partial t} + (\mathbf{v}\cdot\nabla)\,\mathbf{v_A} - (\mathbf{v_A}\cdot\nabla)\,\mathbf{v} = -\frac{1}{2}\mathbf{v_A}\,(\nabla\cdot\mathbf{v}) \tag{2.39}$$

$$\frac{d\,(\,ln\,\rho)^{-\gamma}}{dt} = 0, \tag{2.40}$$

$$\mathbf{v_A}\,(\mathbf{v_A}\cdot\nabla)\,ln\,\rho = -2\,(\nabla\cdot\mathbf{v_A})\,. \tag{2.41}$$

The first equation corresponds to the continuity equation, the second and the third are respectively the equation of force and Faraday's. The fourth and the fifth rep-

resent the polytropic energy equation and the expression of the solenoid magnetic field. We can also combine all these equations in only two expressions, after some algebra:

$$\frac{\partial}{\partial t} ln\rho + \left(\mathbf{z}^{\pm} \cdot \nabla\right) ln\rho = -\frac{1}{2} \nabla \cdot \left(3\mathbf{z}^{\pm} - \mathbf{z}^{\mp}\right), \tag{2.42}$$

$$\begin{aligned} \frac{\partial}{\partial t}\mathbf{z}^{\mp} + \left(\mathbf{z}^{\mp} \cdot \nabla\right)\mathbf{z}^{\mp} = \pm \frac{1}{4} \nabla \cdot \left(\mathbf{z}^{+} - \mathbf{z}^{-}\right) \left[\frac{\partial}{\partial t}\mathbf{z}^{\mp} + \left(\mathbf{z}^{\mp} \cdot \nabla\right)\mathbf{z}^{\mp}\right] ln\rho \\ - \frac{1}{8} \nabla \left(\mathbf{z}^{+} - \mathbf{z}^{-}\right)^2 - \left[c_s^2 + \frac{1}{8}\left(\mathbf{z}^{+} - \mathbf{z}^{-}\right)\right] \nabla ln\rho \end{aligned} \tag{2.43}$$

The two last equations prove to be very useful in deriving the framework for the study of compressible MHD turbulence which is of central interest in this thesis. More details on the use of Elsässer variables in MHD turbulent plasmas and their limitations when compressible turbulence is considered can be found in Magyar et al. (2019), on which the writing of this subsection is based.

2.3 MHD turbulence

As mentioned before, magnetic fields are ubiquitous in the universe. The presence of magnetic fields influences the properties of astrophysical turbulent fluids and the effects related to this state that can be observed on scales ranging from kilometers to megaparsecs. The presence of the magnetic field radically changes the properties of the flows, and the MHD turbulence approximation presents a powerful applicability to describe astrophysical fluids. In this section, we will briefly summarize the main characteristics of the MHD Alfénic turbulence, a commonly accepted theoretical approach to describe the processes of turbulence in the interstellar medium. In addition, we will present the main theories currently mentioned in the attempt to describe astrophysical turbulence: Iroshnikov-Kraichnan and Goldrieich-Shidhar theories. We also shall restrict our discussion to a general idea for compressible MHD turbulence, since this subject is still under construction. The following text is based on Tobias et al. (2011), Biskamp (2003), Galtier (2012) and Brandenburg and Nordlund (2011). For more details about recent developments of theoretical models for MHD turbulence and their applications in astrophysical context, the following readings are recommended: Galtier (2016), Lazarian and Pogosyan (2006), Lazarian (2005), Müller and Busse (2007), Kulsrud and Zweibel (2008), Bigot et al. (2008), Sridhar (2010) and Brandenburg and Lazarian (2013).

2.3.1 Alfvénic MHD turbulence

As mentioned in Section 2.1, the idea of a turbulent flow is related to a chaotic velocity field in space and time. These random motions occur when the velocity field evolution presents strong nonlinear perturbations. Differently from hydrodynamic turbulence, the presence of a magnetic field introduces further complexity in the plasma dynamics, since the isotropic assumption, used in many scenarios of hydrodynamic turbulence can not be considered anymore. In such systems, the Alfvénic turbulence approximation is used to understand the properties of the medium. This approach considers a mean magnetic field with a preferential direction, and any perturbation in the velocity field will be coupled to the magnetic field. The magnetic tension/pressure results in a decrease of the non-linear growth of perturbations, but only for motions perpendicular to the magnetic field lines. This is mathematically expressed by the Elsässer variables, presented on Section 2.2.4. In that formalism, the non-linear interaction takes place between two oppositely propagating Elsässer fields, expressed by: $\mathbf{z}^+$ and $\mathbf{z}^-$ and with respective Alfvénic velocities v_a and $-v_a$.

In this phenomenology, waves packets $\mathbf{z}^\pm$ propagate without distortion until they reach a region where $\mathbf{z}^\mp$ become nonlinear and perpendicular to the magnetic field. Nonlinear interactions are thus solely the result of collisions between counter-propagating Alfvén wave packets. When the turbulence is imcompressible, the Alfvénic MHD theory states that the non-linear interactions can be expressed in terms of Alfvénic modes. As said before, for compressible turbulence, additional complex wave modes including magnetosonic modes are considered. In other words, MHD turbulence starts when there are non-linear interactions between two weakly fluctuating linear modes propagating in opposite directions. The wave mode packets are distorted and split into smaller ones, resulting in a cascade of nonlinear interactions until the energy is converted into heat by dissipation.The end of the cascade process marks the end of the inertial range in the Kolmogorov's spectrum.

For the hydrodynamic case, the energy cascade occurs until a dissipation scale defines the Reynolds number Re being unity. For MHD turbulence, a resistive dissipation scale l_η is defined, associated with magnetic Reynolds number $R_m = lu_l/\eta$ (for ideal MHD case, η is equal zero and $R_m \to \infty$). When the non-linear interaction between the Alfvén wave packets is assumed to be weak, that is, a large number of collisions is required for the energy of a single wave packet to be transferred to smaller scales, the turbulence is called weak. In the opposite case, the turbulence is strong.

There is a parameter that measures the non-linearity of interactions, $\chi(l_\perp)$, defined

as the ratio of the collision crossing time of the wave packets $\tau_{cross} \sim l_{\parallel}/v_A$ and the eddy turnover time $\tau_{eddy} \sim l_{\perp}/u_{l\perp}$, where $\parallel$ and $\perp$ are the directions of the physical quantities with respect the mean magnetic field $\mathbf{B}$. The eddy turnover time can be used to determine when the turbulence can be considered weak or strong. Mathematically,

$$\chi(l_{\perp}) = \frac{l_{\parallel} u_{l\perp}}{v_A l_{\perp}} \tag{2.44}$$

The regimes for which $\chi(l_{\perp}) < 1$ (weak turbulence) and $\chi(l_{\perp}) \geq 1$ (strong) are considered in the scenarios used to explain MHD turbulence by several authors: Elsasser (1950), Dobrowolny et al. (1980), Iroshnikov (1964), Kraichnan (1965), Matthaeus et al. (1999), Pezzi et al. (2017) and Velli et al. (1989). Our next discussion will briefly introduce two theoretical models well accepted in MHD turbulence theory and currently used to explain many astrophysical processes: the Iroshnikov-Kraichnan and Goldreich-Sridhar models. Both cases consider incompressible turbulence, where Alfvénic modes are dominant.

2.3.2 The Iroshnikov-Kraichnan model

Assuming that the transfer of energy in the cascading process is spatially isotropic ($l_{\parallel} = l_{\perp} = l$), Iroshnikov (1964) and Kraichnan (1965) proposed an useful simplified model for a weak Alfvénic turbulent regime. Considering Elsässer variables and Equations 2.42 and 2.43, they found the interactions between the wave packets occurs with a well defined scaling law:

$$u_l \propto l^{1/4}. \tag{2.45}$$

This scaling law results in a $\chi(l_{\perp}) \propto l^{1/4}$. In addition, the corresponding energy power spectrum is

$$P_u(k) \propto k^{-2}. \tag{2.46}$$

The Iroshnikov-Kraichnan model has been well accepted to understand the turbulence existing both in the solar wind and in the interplanetary medium (see Bamert et al. (2008) and Ng et al. (2010) for more details). However, many observations of the solar wind turbulence suggest a more Kolmogorov-like turbulence, i.e., $\propto k^{-5/3}$ (MATTHAEUS; GOLDSTEIN, 1982; HELLINGER et al., 2013). Some authors proposed two turbulence cascade regimes for the magnetic and velocity field fluctuations.

Moreover, the data also reveal that the solar wind turbulence is highly anisotropic with respect to the local magnetic field (HORBURY et al., 2008).

2.3.3 The Goldreich-Sridhar model

Goldreich and Sridhar (1995) proposed a model for strong turbulence, based on anisotropic fluctuations and strong coupling between the wave modes. They assumed that motions perpendicular to the magnetic field lines are mixed on a hydrodynamic time scale. The cascade process occurs with a scaling law:

$$u_{\perp} \propto l^{-1/3} \tag{2.47}$$

The mixing motions couple to the wave-like motions parallel to the magnetic field, reaching a critical balance condition when $\chi(l_{\perp}) \sim 1$. The associated power spectrum takes the form:

$$P_u(k) \propto k^{-5/3}, \tag{2.48}$$

with anisotropy scale-dependence for the eddies:

$$l_{\parallel}^{-1} V_A \approx l_{\perp}^{-1} u_l. \tag{2.49}$$

The equations above imply that the smaller eddies have shapes more elongated in the direction of the local mean magnetic field. For this reason, anisotropy is measured in the reference frame of the local field. This theory is supported by several numerical simulations (see Cho and Vishniac (2000), Maron and Goldreich (2001), Cho and Lazarian (2002), Beresnyak and Lazarian (2010), Beresnyak (2011), among others). Actually, simulations show that both Iroshnikov-Kraichnan and Goldreich-Sridhar theories can be used to describe MHD turbulence, depending on the dynamical conditions of the fluctuations - which is basically dominated by the sonic Mach number.

2.3.4 Compressible MHD turbulence

Compressible magnetized turbulence is a highly non-linear phenomenon and its complexity arises with the formation of a hierarchy of density structures that are coupled to velocity and the magnetic field. In this scenario, different types of perturbations

or modes (Alfvén, slow and fast) are strongly coupled. The properties of compressible MHD turbulence are studied separating supersonic or subsonic regimes, since the generation of compressible modes is different in each case. There are still debate on how the scaling laws can be expressed in these regimes. However, due to the improvements of high resolution numerical simulations, significant evolution has been made in the understanding of compressible MHD turbulence.

Cho et al. (2003) showed that if the regime is subsonic, the turbulence can be decomposed in three modes: Alfvén, slow and fast modes. They found that the coupling of compressible and incompressible modes is weak in such regime and the Alfvén modes follow the Goldreich-Sridhar theory. In the supersonic regime, compressible modes can also be produced in the plasma. The weak turbulence treatment of compressible MHD for fast and Alfvén waves suggests that only a small amount of energy is transferred from magnetosonic fast waves to Alfvén waves at large modes. In this regime, Alfvén and slows modes follow Goldreich-Sridhar and Kolmogorov's energy spectra, when the gas-pressure is higher than the magnetic pressure (represented by a a plasma parameter $\beta > 1$). For the case when magnetic pressure is dominant ($\beta < 1$), the energy spectrum is steeper than the provided by Goldreich-Sridhar theory. For the fast modes, the energy spectrum presents an isotropic cascade and follows $P(k) \propto k^{-3/2}$.

The picture of Alfvén waves cascade to describe the incompressible MHD regime is not expected to change when compressible modes are present. However, this is an open physics problem and still debated. One thing that is clearly important in the context of the MHD compressible turbulence theory is the use of different statistical tools and high resolution numerical simulations to confront with analytical models on the subject. The use of the comparative approach not only improves the knowledge about the physics of the problem, but also has been fundamental to understand how the compressible MHD turbulence can be related to other phenomena in the interstellar medium. The study of statistical correlations among physical quantities helps physicists and astrophysicists to better understand the complex phenomenology. In the next chapter, the evolution in the understanding of turbulence in the interstellar medium, as well as a general review of the observational characteristics of the different phases of the ISM will be presented.

3 INTERSTELLAR TURBULENCE AND MAGNETIC FIELDS

3.1 Interstellar medium

The interstellar medium (ISM) can be understood as a dynamic environment among the stars, filled with charged particles, atoms, molecules and dust grains. The understanding of the properties observed in the ISM provides powerful insights regarding several important physical processes in the Universe, such as: Galaxy formation and evolution (*e.g.,* Mo et al. (2010)), the formation of stars (*e.g.,* McKee and Ostriker (2007)), cosmic nucleosynthesis (*e.g.,* Ryan (2002)), the origin of large complex molecules (*e.g.,* Seaton (1951)), prebiotic molecules (*e.g.,* Puzzarini (2020)), the abundance, structure and growth of dust grains (*e.g.,* Whittet (1988)) which constitute the fundamental ingredients of planetary systems formation, among others (see Draine (2011) for more examples).

However, despite its importance, the ISM structure and evolution is still poorly understood. The existence of a wide range of temperatures and densities which span different regions of the ISM indicates that characterizing the ISM is a multi-scale and multi-physics problem (DYSON; WILLIAMS, 2020). In order to address these different chemical and physical properties for each region observed, the ISM is typically studied as multi-phase medium. This idea was initially introduced by Field (1965) who proposed a simple two phases-model consisting of a cold and a warm neutral phase in static equilibrium. Nowadays, based on advances in observational techniques and high-resolution telescopes, the thermal and chemical state of the ISM is far from being considered in equilibrium and conventionally described in terms of four phases with similar properties (MCKEE; OSTRIKER, 1977). Each phase will be described on the next subsections.

3.1.1 Dense molecular regions

This ISM phase consists of regions with substantial condensation of the interstellar molecules where the star formation process occurs (TIELENS, 2005). Gravitationally bounded molecular clouds are in this phase and present low temperature ($T \sim 10$–$50\ K$), high values of columnar density ($n_H > 10^3\ cm^{-2}$) and visual extinction ($A_V > 3$) are part of categories which constitute this ISM phase (DRAINE, 2011). These regions are mainly composed of molecular hydrogen (H_2) and a rich mixture of other interstellar molecules (ROHLFS; WILSON, 2013). Even though H_2 is the most abundant element, its detection is not easy. There are several factors such as low cloud temperatures, homonuclear and symmetric nature of this molecule;

which make the probability of rotational/vibrational energy states extremely low and the spectral line intensity weak (GLOVER; CLARK, 2012). Rotational transitions for this molecule are also difficult to observe. Fortunately, the existence of other molecules presenting different critical densities and different optical depth allows to trace densities and temperature to varying scales in molecular clouds gas. Dust grains are also fundamental constituents of a molecular cloud. These particles have sizes varying between 0.05 – 0.25 μm and despite their low abundance compared to the atomic and molecular gas, their presence affects both thermodynamics and chemistry of molecular clouds (HOCUK et al., 2015). Besides, dust grains shield molecular clouds from the ultraviolet radiation field ubiquitous in the interstellar medium, preventing molecules from being photodissociated (ROBERGE et al., 1991).

3.1.2 The cold atomic and warm neutral phases

Most of the ISM neutral atomic gas is composed by hydrogen and the detection of this gas presents both emission and absorption lines. Due to the temperature and density conditions, the emission detection of this species occurs with a forbidden transition in 21 cm wavelength. This line results from the hyperfine structure, caused by the interaction of the magnetic moments of the electron and the proton within the atom. The main applications of 21 cm observations are based on the estimation of the mass, the distribution and the kinematics of cold and warm phases (CLARK, 1965).

Using HI emission and absorption analysis, it was found that neutral gas presents two stable phases, that exist in pressure equilibrium: the cold neutral medium (CNM) with moderate densities ($n_H \approx$ 10-50 cm^{-3}) and temperatures ($T \approx$ 100-300 K), and the warm neutral medium (WNM) with low densities and high temperatures ($n_H \approx$ 0.1-0.3 cm^{-3} and $T \approx 10000K$) (WOLFIRE et al., 2003). The WNM is mostly responsible for what is observed in HI emission, while CNM is detected in absorption against either continuum sources or in the background of HI emission (KALBERLA et al., 2010). The theoretical model for the existence of this two-phase neutral structure was investigated initially by Field et al. (1969) and Wolfire and Cassinelli (1986).

CNM is primarily associated with diffuse cold external atomic layers in molecular clouds which are result from the dissociation by UV photons in the external part of dense clouds (FAISON; GOSS, 2000). This region can be observed in diffuse clouds where the gas is not dense enough to significantly extinct the UV field over the size of the cloud (HEILES; TROLAND, 2003). On the other hand, the WNM is most broadly

defined as the neutral and dense component of ISM where penetrating far-ultraviolet radiation dominates the gas heating and thermal balance, typically observed in the external layers of denser clouds where the UV field has not yet been completely absorbed.

3.1.3 The warm ionized medium (WIM):

The existence of this ISM phase was initially proposed by Hoyle and Ellis (1963) and nowadays is well-established, being referred as the major component of the Galactic interstellar medium (HILL et al., 2008), occupying 30-40 % in the local interstellar medium (REYNOLDS et al., 1999). It consists of a plasma nearly fully ionized and diffuse gas with low-density ($\approx 0.1\ cm^3$) and temperatures between 6000–10000 K (MADSEN et al., 2006). The best tracer of the ionized medium (WIM) is $H\alpha$ line emission (FRISCH, 2001).

In addition, the WIM is associated with the photoionization radiation from hot stars. There are two distinct gases that can be detected due to photoionization process: a dense region called an HII region, and a lower density "intercloud" medium which is the WIM. The HII regions have densities ranging from $10^2 - 10^5\ \ cm^{-3}$, whereas typical densities in the WIM are much lower ($\approx 0.1\ cm^{-3}$) (CHURCHWELL, 2002). How the ionization is maintained in this region is still not well understood (GREENAWALT et al., 1997). The most likely source of ionizing photons are O and B-type stars, but it is unclear yet how the radiation is able to propagate across the kiloparsec size scales unabsorbed, given the distribution of the WIM (WOOD; MATHIS, 2004).

3.2 Interstellar magnetic fields

The local interstellar magnetic field has been measured *in-situ* by spacecrafts (see Wimmer-Schweingruber (2018) for more information) and on larger scales by electromagnetic radiation analysis of embedded charged particles, cosmic rays, gas, or dust (see Crutcher (2000), as an example). In-depth analysis extends from Earth (*e.g.,* Finlay et al. (2010)), the Sun and their neighborhood (*e.g.,* Babcock (1963)), solar planets (*e.g.,*, Lada et al. (1997)) stars (*e.g.,* Madsen et al. (2006)), molecular clouds (*e.g.,* Crutcher (2012)), pulsars (*e.g.,* Kaspi and Beloborodov (2017)), the Milky Way (*e.g.,* Haverkorn (2015)), nearby galaxies, distant galaxies (*e.g.,* Heald and Braun (2009)), quasares (*e.g.,* Furlanetto and Loeb (2001)), and even intergalactic space in clusters of galaxies (*e.g.,* Govoni and Feretti (2004)), among others.

Alfvén (1942) was the first one to propose that the existence of magnetic field threading the interstellar space could explain the cosmic rays confinement in our Galaxy. Nowadays, it is well established that interstellar magnetic fields pervade the Universe in different orders of magnitudes, being responsible not only for the acceleration and confinement of cosmic rays, but also the spatial distribution and energetic dynamics of different astrophysical environments (ALVES; FERRIERE, 2018).

Combined with non-thermal effects and cosmic rays, the magnetic field contribute significantly to the structure and evolution of the ISM (FERRIÈRE, 2005). Therefore, the determination of its structure is crucial. In disk galaxies, for example, the magnetic fields are modeled by two different superimposing field components. The large-scale regular field component is measured around $3-10\ \mu G$, detected mainly in the galactic disk plane (BECK, 2015). The second one is a locally disturbed magnetic field component, related to molecular clouds and star formation regions, detected in dimensions $\sim 10 - 100$ pc (HAN, 2006). Recently, magnetic fields with similar strengths and coherence were found in spiral galaxies and detected even in the hot plasma filling clusters of galaxies. For galaxies other than spirals, the information related to the geometry and topology of the magnetic field is poorly known.

With the development of astronomical instruments, estimating the magnetic field has become increasingly robust for the different conditions of the interstellar medium (GOODMAN, 1995). Nowadays, the main techniques used to estimate the magnetic field properties are the polarization resulting from interstellar dust, synchrotron polarization emission, Faraday rotation, dust polarization from the background stars radiation, and Zeeman effect on spectral lines (HEILES; TROLAND, 2003). These techniques are important due to the different conditions of temperature, density, varieties of molecular species and the nature of the grains that make the interstellar medium a complex region (CRUTCHER et al., 1993).

This section will address each of these techniques, their limitations and under what conditions they can be used. Finally, we also discuss recent techniques presented in the literature, known as velocity and synchrotron polarization gradients, and their promising advantages, since they not only estimate the intensity and geometry of the magnetic field, but also characterize other effects of the turbulent interstellar medium. The information presented in this section are based on Draine (2011), Crutcher (2012), Lequeux (2005), Falceta-Gonçalves et al. (2014), Falgarone and Phillips (1990), Crutcher (2012), González-Casanova and Lazarian (2017) González-Casanova and Lazarian (2017), Lazarian et al. (2017), Lazarian et al. ().

3.2.1 Polarization maps by dust emission and absorption

The discovery that the optical linear polarization of starlight presents a preferential direction was done by Hall (1949) and Hiltner (1949). Further investigations showed that these preferential directions are related to interstellar grains which are aligned with the Galactic magnetic field (see Andersson (2012), Lazarian and Prunet (2002) and Goodman et al. (1990)). Figure 3.1, on the left side, presents the relationship between the polarization degree in the optical and near infrared spectral ranges and extinction that corresponds to the amount of dust along the line of sight. In addition, the comparison between the dust (yellow color) and the synchrotron polarization emission (blue color) on the right side in Figure 3.1, shows that the angles between these two vectors, yellow and blue, are fairly orthogonal. The synchrotron polarization direction is well known to present the same direction of the magnetic field projected on the line of sight. Therefore, this comparison shows that both quantities are closely related.

Figure 3.1 - (a) The polarization fraction p as a function of extinction A_V indicating a correlation between polarization and dust contents. (b) The optical and near-IR polarization vector (blue bars) and synchrotron polarization vector (yellow bars). The map shows that both vectors are preferentially orthogonal.

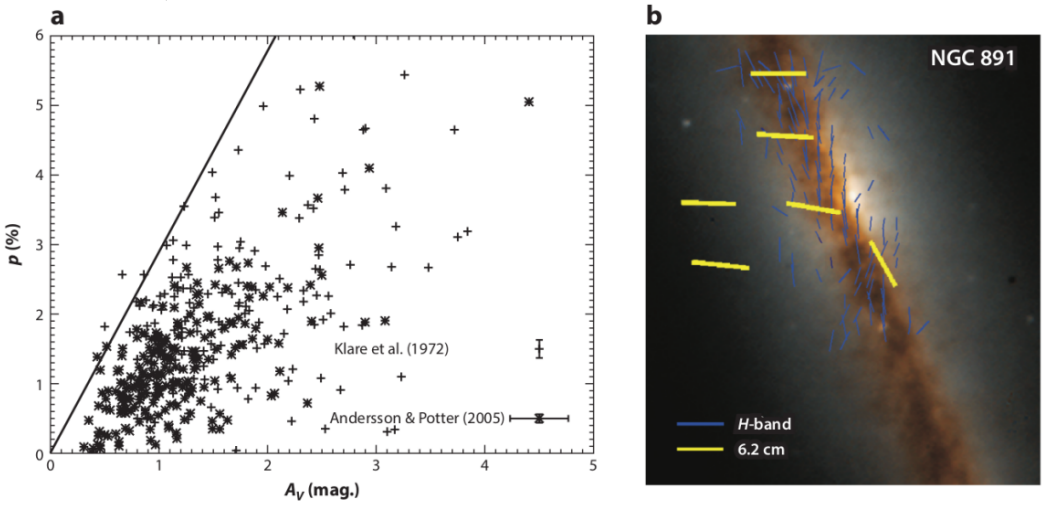

SOURCE: Andersson (2012).

Since the discovery of dust grain alignment with the magnetic field, a substantial progress has been made in order to understand the physics of this effect. The existing models agree that rotating non-spherical dust grains align with their shorter

axis parallel to the magnetic field direction (*e.g.,* Spitzer Lyman and Tukey (1951), Purcell (1979), among others). The most accepted theory that can explain the mechanism of dust alignment is known as radiative torques, introduced by Dolginov and Mitrofanov (1976) and reviewed in detail by Lazarian and Pogosyan (2006). In this magneto-mechanical alignment theoretical model, the dust grain gains rotational energy by a supersonic gas stream with the preferential direction of alignment remaining parallel to the magnetic field lines (see Andersson (2012) for more details). This theory is scale independent and might explain the rotation alignment in supersonic environments in which the alignment is typically observed (RAO et al., 1998).

Therefore, the information about the magnetic field can be decoded by estimating the polarization mechanism produced by dust grains. This polarization can be created by two different mechanisms. The first one occurs due to the dichroic extinction caused by dust grains in unpolarized radiation of background stars, which present maximum attenuation in the parallel direction of the projected component of then magnetic field in the plane of sky ($B_{\parallel}$). Consequently, the polarization vector detected in such regions is perpendicular to the magnetic field component ($B_{\perp}$). Figure 3.2 presents an illustration of this effect. This polarization effect is observed in the optical and near-IR wavelengths. Observations from the polarization maps in optical indicate that when the extinction is high, the intensity of the polarized emission is low, making this method imprecise for dense regions. In addition, polarized starlight provides an very good 2D spatial resolution, however, it depends on the density of background stars. Hence, the morphology of $B_{\perp}$ can be estimated with the determination of the polarization vector, being a useful method for studying the large-scale magnetic field structure in molecular clouds, where the dust grains are abundant. However, the accuracy of this method depends strongly on the visual extinction (A_V), being more effective for small values of A_V.

A second mechanism which produces polarized radiation is the thermal emission by grains when they are heated, being also perpendicular to $B_{\perp}$. The polarized emission is usually detected on millimeter and submillimeter wavelengths. The estimation of the polarization vector with this method is advantageous for studying magnetic field structure at larger values of A_V (even larger than 20) and is used to obtain information in denser regions of molecular clouds, such as clumps and cores. Figure 3.3 shows an example of dust and starlight background polarization extinction of molecular cores in the Orion giant molecular cloud. The observed polarized emission vectors have been rotated by 90°, to show the direction of the magnetic field. Li et al. (2009) indicated that the mean magnetic field direction in

Figure 3.2 - Illustration of the process of polarization of background star radiation due to the extinction caused by grains.

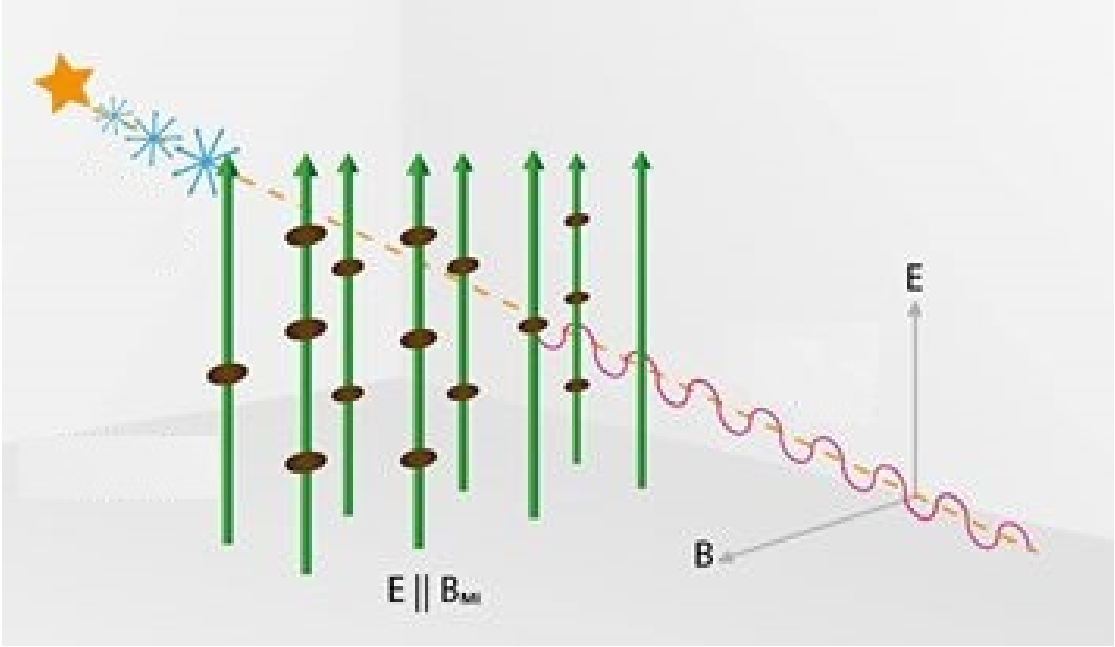

SOURCE: Adapted by Lazarian and Prunet (2002).

Orion's cores (except for OMC1 case) are well aligned with each other and with the mean field direction traced by optical starlight polarization in the more diffuse gas. These measurements are critical to understand the evolution of the large-scale Orion magnetic field, as well as the smaller regions where star formation occurs.

Figure 3.3 - Polarization map in the Orion molecular cloud region. Light blue vectors show optical data of the extinguished radiation of background stars. Emission of dust obtained in 350 μm measured with the Hertz Caltech Submillimeter Observatory is shown in red vectors. The polarized emission vectors have been rotated by 90°.

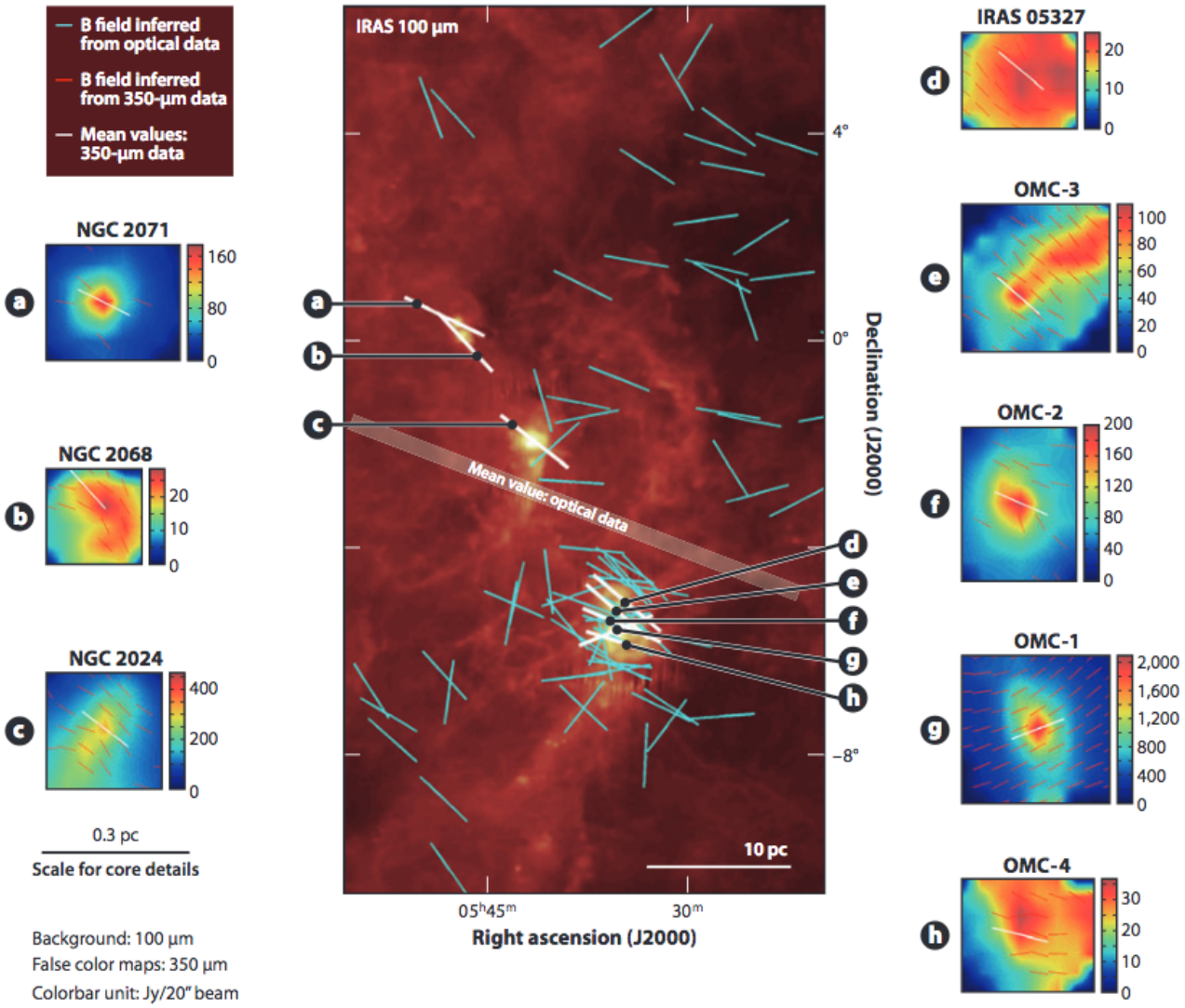

SOURCE: Li et al. (2009).

In addition, the degree of polarization depends very weakly on the magnetic field strength, so dust polarization vectors do not provide direct determination of the intensity of the magnetic field. Therefore, a statistical indirect method is necessary to estimate the strength of the field. Chandrasekhar and Fermi (1953) proposed a way

to estimate the strength of the magnetic field in the spiral arms of our Galaxy, based on the magnetic orientation of interstellar dust grains. The so-called Chandrasekhar-Fermi (CF) method is based on an assumed balance between the fluctuations of the gas density and the local magnetic field; assuming that interstellar turbulence is incompressible and isotropic, and also that there is equipartition between turbulent and magnetic energy. Chandrasekhar and Fermi derived an expression for the magnetic field strength in the plane of the sky as a function of the dispersion of magnetic field direction and velocity dispersion, mathematically described as:

$$B_{\perp} = \sqrt{4\pi\rho}\frac{\delta v}{\delta\theta}, \tag{3.1}$$

where $B_{\perp}$ denotes the average magnetic field projected in the sky, ρ is the density of the gas, δv is the velocity dispersion (obtained by spectroscopy) and $\delta\theta$ is the dispersion in polarization position angles.

Despite the importance of the CF technique, there are a number of limitations that can lead to an unrealistic estimation of the mean magnetic field. Several works attempted to improve the accuracy of this method throughout the years (see Crutcher (2012) for more details). For example, Ostriker (2003) attempted to calibrate the fact that polarization measurements do not sample tangled magnetic fields along the line of sight, using a smoothing method estimated via numerical simulations of interstellar clouds. Heitsch et al. (2001) numerically showed how limited telescope resolution can affect the estimation of $\delta\theta$, and proposed a smooth pattern fitting to correct this. Further, Falceta-Gonçalves et al. (2009) proposed a statistical method to separate only the turbulent contribution to $\delta\theta$ using higher order statistical analysis. Houde et al. (2009) added further refinements to the CF method with analytical analysis including the effects related to large-scales structured fields and a turbulent field, explicitly including integration over the telescope beam and along the line of sight of both the magnetic field structure and the polarized emission structure.

There are still significant uncertainties in the application of the CF technique. For example, the lack of information regarding $B_{\parallel}$ reduces the value of $\delta\theta$, causing an underestimation of this quantity. Besides, the estimation of density using spectroscopy as an additional technique increases the complexity of estimating mean magnetic fields with the CF technique. In addition, the choice of spectral lines for density estimation has to delimit specifically the sample region that represents the polarized region to not introduce biases. Also, since the estimation of the nonthermal and turbulent line widths is done along the line-of-sight, the retrieved values used

for these parameters may be incorrect. The efficiency of the grains alignment affects the determination of the magnetic field direction via polarization maps, since for high optical depths, the grains alignment with the magnetic field is suppressed. The theoretical assumptions of stationarity, homogeneity, and isotropy to derive the CF expression are also clearly not observed in most of the ISM. Also, how the complex thermodynamics and existence of self-gravity can affect the estimation of magnetic field morphology using polarization maps is still uncertain, and more analysis on the subject needs to be carried out.

3.2.2 Estimation of magnetic fields by Zeeman effect

The interaction between an atom or molecule with an external magnetic field splits the energy levels into different frequency line components. This is called Zeeman Effect, which is caused by the coupling between angular momentum $\mathbf{L}$ and the magnetic moment ($\boldsymbol{\mu}$), resulting in a set of discrete transitions (ZEEMAN, 1897). The magnitude of the energy splitting produced by Zeeman effect is directly proportional to the strength of the magnetic field (HERZBERG; SPINKS, 1950). Mathematically, it can expressed as

$$\Delta\nu_Z = \frac{eh}{4\pi mc} B_{LOS} \equiv Z B_{LOS}, \tag{3.2}$$

where e is the elementary charge, h is Planck's constant, m is the particle mass, c is the speed of light and, finally, B_{LOS} is the magnetic field in the line of sight. Z is known as the Bohr magneton, a parameter that depends on the atomic or molecular species. The effect manifests itself in two forms, depending on the number of frequency splits. The normal Zeeman effect occurs when the spectral line is split into three components: a simple triplet pattern consisting of one component with the energy level of the line in the absence of any external magnetic field and two other components shifted from it. This normal Zeeman effect happens when there is no spin magnetic moment on the molecule. The unsplit line is called the π component, which has the unchanged frequency. The two other split components are referred to as $\pm\sigma$ components. The σ components are generally elliptically polarized and the π component is unpolarized. The second case is known as anomalous Zeeman effect and occurs when the total spin is nonzero, resulting in double splitting. The anomalous Zeeman effect is not commonly observed in molecules present in molecular clouds. The split lines are governed by the selection rules of quantum mechanics. Also, in this case, the π component is linearly polarized, and the σ components are generally elliptically polarized. The polarization effect is also a consequence of the selection rules of quantum mechanics and the coupling of magnetic and angular

momenta that produce the Zeeman effect. The magnetic quantum number variation (μ_B) for the π component is 0 and ± 1 for the σ components. Considering the example of the solution of the Schrödinger equation for the hydrogen atom, in classical terms, $\Delta\mu_B = 0$ corresponds to an angular radiation pattern of a dipole oscillating parallel to the external magnetic field. Then, by a projection effect, the light emitted perpendicular to the magnetic field is linearly polarized, whereby the E-vector oscillates in the direction of the dipole and parallel to the magnetic field. Conversely, $\Delta\mu_B = \pm 1$ corresponds to two parallel dipoles oscillating with phase difference of 90°. The superimposition of the two dipoles produces a circulating current. Thus, in the direction of the magnetic field, the emission is polarized (KASTLER, 1946). More details on the physical processes related to this effect can be found in Schwabl (2005) and Ramos and Bueno (2006).

The Zeeman effect has provided astrophysicists with an important technique for obtaining information about the physics of the sun and stars (HALE, 1908). In addition, due to the fundamental nature of the Zeeman effect, the strength and direction of the magnetic field ($B_\parallel$) with respect to the line of sight provides a powerful tool specially for diagnosing star formation regions and interstellar clouds. The mean strength of the magnetic field depends on the estimation of the σ polarized component (CRUTCHER et al., 1993). The mathematical description of the circular polarization is done with the use of the Stokes parameter $\langle V(\nu)\rangle$, which is proportional to $B_\parallel$:

$$\langle V(\nu)\rangle = aI(\nu) + \left(\frac{ZB\cos(\theta)}{2}\right)\frac{dI(\nu)}{d\nu}, \tag{3.3}$$

where a is a scaling factor, or gain correction, if there are differences between circular left and circular right polarizations due to instrumental effects; θ is the angle between the field direction and the observer's line of sight. A fit of this equation to observational data can reveal the magnitude and direction of the $B_\parallel$, since the polarization direction is in the same direction as that variable.

However, the Zeeman effect technique applied to distinct environments such as interstellar and molecular clouds, clumps and cores, is limited, since it does not show up for all molecular and atomic species. Most of the common interstellar molecules have all their electrons paired (nonparamagnetic species) and therefore do not have strong Z factors (CRUTCHER et al., 1993). This fact makes the split components very weak and with small separations, depending on the physical conditions of the ob-

served region, being the main reason for the limitation. For example, in molecular clouds, the most common species detected by Zeeman measurements are: C_2H, SO, C_2S C_4H, CH, $C+$ in recombination lines, and the masers of OH, CH_3, SiO and H_2O (CRUTCHER, 2012). Figure 3.4 shows an example from Falgarone et al. (2008) for the DR21 molecular cloud. They carried out a CN Zeeman survey together with earlier CN Zeeman observations presented by Crutcher et al. (1996) and Crutcher et al. (1999), measuring 14 different positions of dense molecular cores observed with significant sensitivity.

Figure 3.4 - a) CN Zeeman Stokes I and V profiles towards DR21(OH). (b) CARMA map of velocity-integrated CN towards DR21(OH). Contours are CN isolevels, colors in the image represent dust continuum emission and the dotted circle is the footprint of the IRAM 30-m telescope beam.

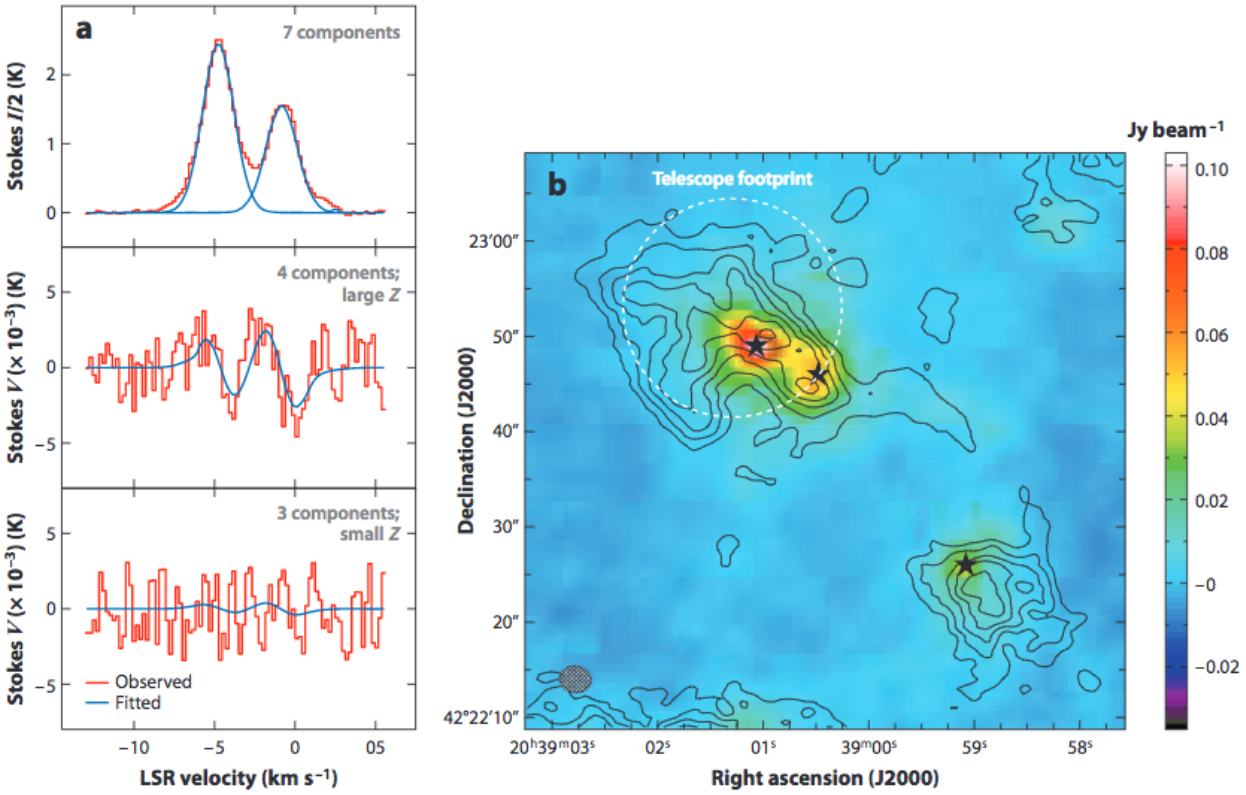

SOURCE: Crutcher et al. (1999).

3.2.3 Synchrotron emission and Faraday Rotation effect

Synchrotron emission is a polarized non-thermal radiation generated by relativistic electrons, moving in a helicoidal trajectory through a large-scale magnetic field (RYBICKI; LIGHTMAN, 1979). This radiation can be detected in many different astronomical environments, such as: active galactic nuclei (*e.g.,* Clausen-Brown et al. (2011) and Biermann and Strittmatter (1987)), radio galaxies (*e.g.,* Hardcastle (2013) and), the Milky Way (*e.g.,* Haverkorn (2015) and Wielebinski (2005)), intracluster medium (*e.g.,* Govoni and Feretti (2004) and Pfrommer and Dursi (2010)), almost all star-forming galaxies (*e.g.,*Klein and Graeve (1986) and Tabatabaei et al. (2007)), the warm neutral and ionized interstellar media (*e.g.,* Iacobelli et al. (2013) and Haverkorn and Spangler (2013)), supernovas (*e.g.,* Vink and Laming (2003) and Berezhko and Völk (2004)), spiral galaxies (*e.g.,* Beck (2015) and Shukurov (2005)), among other radio and x-ray sources.

The understanding of the physics of synchrotron emission production provides meaningful physical quantities that characterize the condition of the emitting region: the electron distribution, the strength of magnetic fields. Also, the degree of polarization is an important indicator of the field uniformity and structure, which makes their estimation a valuable technique specially for estimating the interstellar magnetic field in different interstellar phases (see Beck (2009) for more information). In addition, this emission produces a direct measurement of the magnetic field vector perpendicular to the plane of the sky, which again makes it a powerful technique to estimate the properties of $\mathbf{B}$. The population of electrons that emit synchrotron radiation is generally described by a power-law energy distribution given by

$$N(E)dE = KE^{2\alpha-1}dE, \tag{3.4}$$

where E is the energy of the electrons, $N(E)$ is the number density of electrons with energy between E and $E + dE$, K is a normalization constant, and α is the spectral index for the emission, $I \propto \nu^{\alpha}$. To determine the intensity of the synchrotron radiation, we assume that the ultra-relativistic electrons have a homogeneous and isotropic power-law energy distribution of the form of Equation 3.4, following the energy equipartition principle between the electrons and magnetic fields (see Beck (2005) for more details).

The emitted synchrotron intensity I, at frequency ν, is then given by Ginzburg and Syrovatskii (1965):

$$I(\nu) = \frac{e^3}{4\pi m_e c^2} \int_0^L \frac{\sqrt{3}}{2-2\alpha} \Gamma\left(\frac{2-6\alpha}{12}\right) \Gamma\left(\frac{22-6\alpha}{12}\right) \left(\frac{3e}{2\pi m_e^2 c^5}\right)^{-\alpha} K B_\perp^{1-\alpha} \nu^{-\alpha} dL', \tag{3.5}$$

where $B_\perp$ is the strength of the magnetic field perpendicular to the line of sight, Γ is the gamma function, e is the electron charge, m_e is the electron mass, and c is the speed of light. As shown by Equation 3.5, the synchrotron intensity is primarily dependent on the strength of the magnetic field perpendicular to the line of sight, and the spectral index can be measured from the variation of intensity with frequency. The typical sensitivity of telescopes/detectors and the large intensity of emission from several types of astronomical objects, together with the frequency dependence of the emission provide valuable information from this astrophysical process.

Synchrotron radiation also presents linear polarization, which is related to the total intensity (see Equation 3.5) by the polarization fraction, p, expressed as:

$$p = \frac{P}{I} = \frac{3\alpha - 3}{5 - 3\alpha}, \tag{3.6}$$

In order to describe the polarized emission that we measure, it is convenient to express this measurement in terms of the Stokes parameters, Q and U. They can be calculated from the polarization intensity and polarization angle, ψ, with the following expressions:

$$Q = P\cos 2\psi, \qquad U = P\sin 2\psi. \tag{3.7}$$

The polarization can be understood as complex configuration, $P = Q + iU$, which corresponds to a vector in the $Q - U$ plane. The polarization intensity and position angle are written in terms of the Stokes parameters as:

$$P = \sqrt{Q^2 + U^2} \qquad \psi = \frac{1}{2}\arctan\frac{Q}{U} \tag{3.8}$$

The polarization angle ψ is oriented perpendicular to the direction of the magnetic

field projected onto the sky, and by convention, measured anti-clockwise from North (see Gardner and Whiteoak (1966) and Saikia and Salter (1988) for more information on the polarization of synchrotron emission).

Another important physical phenomenon related to synchrotron emission in the interstellar medium is Faraday Rotation. When polarized radio waves propagate through a magneto-ionic medium, the left- and right-hand circularly polarized wave components experience different phase velocities (SPITZER, 1978). Since any linearly polarized wave can be expressed as a superimposition of one left- and one right-hand circularly polarized waves, the plane of polarization of the linear resultant rotates (TRIPPE, 2014). When the Faraday effect is present, the rotation in radio polarization emission becomes proportional to the projection of the magnetic field along the line of sight (OBEROI; LONSDALE, 2012). The Faraday effect is extensively used in astronomy to investigate the magnetic field properties (see Stone (1963) for more information).

Faraday rotation produces a polarization angle ψ that can be expressed as

$$\psi = \psi_0 + RM\lambda^2, \tag{3.9}$$

where ψ_0 is the synchrotron polarization angle without rotation, and λ is the wavelength of the radiation. In Equation 3.9, RM is the rotation measure, given by

$$RM = 0.81 \int_L^0 n_e B_\parallel dL', \tag{3.10}$$

where L is expressed in parsecs, n_e is the electron density in cm^{-3} , and $B_\parallel$ is the strength of the magnetic field parallel to the line of sight, in μG. The integration is performed along the line of sight to the observer, with $B_\parallel$ defined as positive when orientated towards the observer. From the equations above, when synchrotron polarization is observed at different wavelengths, the rotation measure can be estimated.

For a polarized source observed at multiple frequency bands, a single RM value can be fit to the polarization orientation as a function of frequency, and this RM represents the integrated product of the thermal electron density and the magnetic field along the line of sight. This observable is unique and is currently used not only to probe the orientation of the magnetic field but also its direction: when the RM is positive, the magnetic field is directed towards the observer. Faraday rotation provides a very sensitive mean of studying the magnetic field in a 3-D sense, and is

applied specially for the study of the warm ionized medium.

Figure 3.5 - Scheme summarizing how a linearly polarized electric field oscillates travelling through a magneto-ionic region between the source and the observer. The Faraday rotation occurs in the right-hand sense about the magnetic field. In this example, **B** is oriented towards the observer, and the Faraday rotation is counterclockwise in the plane of the sky. The polarization angle (ψ) convention in the plane of the sky is also shown in the Figure (measured counterclockwise from North; see inset in the upper-left corner).

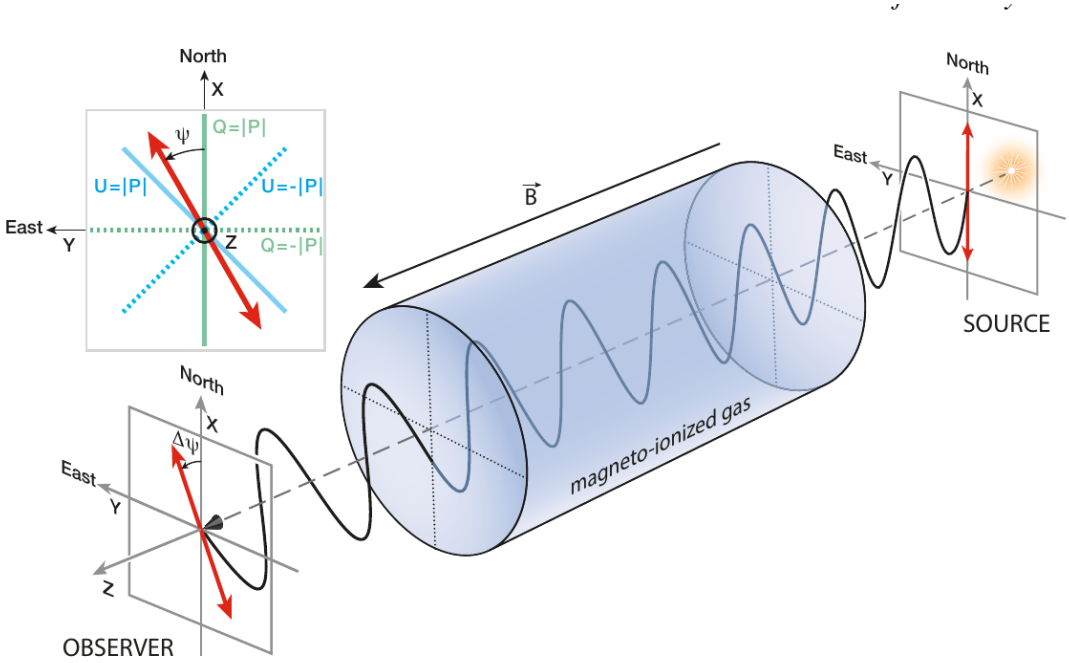

SOURCE: Ferrière et al. (2021).

3.3 Magnetized interstellar turbulence

Turbulence affects the structure and motions of nearly all temperature and density regimes in the interstellar gas. The first work that explains the interstellar gas evolution in the presence of turbulence was pioneered by Weizsäcker (1951b). Later on, direct and indirect signatures of turbulence were observed in different astrophysical environments, ranging from the smallest up to cosmological scales. This section will present a general discussion of the phenomenon, focusing on the most relevant topics for this thesis. More details related to interstellar turbulence can be found in:

Falceta-Gonçalves et al. (2014), Hennebelle and Falgarone (2012), Elmegreen and Scalo (2004), Scalo and Elmegreen (2004) and Klessen (2004).

The dynamical evolution of the ISM and its observational parameters cannot be characterized without the understanding of MHD turbulence (PADOAN; NORDLUND, 1999). Most of the studies on the turbulent interstellar gas are based on measurements of column densities and gas velocities statistical distributions. These two observational quantities provide important insights to determine the main turbulence features of the interstellar gas, usually measured by emission line and continuum emission of various atomic and molecular species (KRITSUK et al., 2017). The statistical analysis of these observational quantities reveals that the interstellar gas presents extremely irregular filaments of density with chaotic velocity fields that are consistent with a turbulent scenario (KLESSEN, 2004).

Despite its importance, characterizing astrophysical turbulent fluids is extremely difficult (BURKHART, 2021). Interstellar turbulence differs from the well-know Kolmogorov theoretical model in several important aspects. This theory considers isotropy and incompressibility as essential assumptions (SCHMIDT et al., 2009). As can be seen on the observational distributions, the interstellar turbulence is neither isotropic nor homogeneous (KRITSUK et al., 2017). The astrophysical fluids are highly compressible and magnetized. The existence of the interstellar magnetic fields breaks the isotropy, and the turbulence characteristics, in such scenario, depend on the direction of observation (BEATTIE et al., 2020). Most interstellar fluids are magnetized and ionized. MHD turbulence physics is often used as an approach to the study of different astrophysical environments (CHO et al., 2003).

Another important consideration is that interstellar turbulence, different from laboratory experiments – where the driving often comes from the interaction with boundaries – presents a fair independence of explicit boundaries and is easily subject to intrinsic instabilities. Consequently, the interstellar medium should be understood as a multi-phase medium with many nonlinear effects. Thus, a unique analytical theory capable of describing the different astrophysical scenarios is an open challenge in astrophysics.

Fortunately, the application of different synergistic approaches has been successful, enhancing the understanding of the physics of interstellar turbulence (BERESNYAK; LAZARIAN, 2019). The use of different statistical tools, observational data and high resolution MHD simulations helps astronomers to understand how physical quantities evolve in this chaotic environment (SCALO; ELMEGREEN, 2004). Observationally,

the main techniques used to study MHD turbulence are based on measurements of column densities and line velocity profiles. Analyses involving probability distribution functions and power spectra, indicate that both densities and velocities are far from Gaussian equilibrium distributions. The analysis of these quantities is useful to obtain information of how the turbulent energy transport occurs over different scales (*e.g.* Burkhart et al. (2009).

Figure 3.6 shows the probability density functions, obtained from visual extinction A_V, of four molecular clouds: two located at high galactic latitudes, Spider (top left) and Polaris (top right), and two at low latitudes, Monoceros R2 (bottom left) and Orion A (bottom right). For cases with no star formation (the Spider cloud), a description with a single log-normal probability density function is very well suited to describe the frequency of cases against A_V. As star formation begins to be more and more important (the Polaris cloud) the log-normal PDF is no longer the best option to describe the distribution, with a power law tail fitting well the observed data (SCHNEIDER et al., 2015), for high values of A_V. The same pattern happens for low latitudes: Monoceros R2 has low star formation, and a relatively less steep power law tail, while Orion A, with enhanced star formation has the smaller inclination in the power law tail. Many numerical works discussed that these distribution patterns can be explained under the assumption of MHD turbulence combined with self-gravity conditions (see Kowal et al. (2007), Burkhart et al. (2009) and Burkhart and Lazarian (2011) for more information).

Regarding turbulence velocity distributions, the spectral lines analysis also reinforce that turbulence is an omnipresent regime. For example, the HI hyperfine broad emission showed that warm cold medium in the Milk way is extremely irregular (KALBERLA; KERP, 2009). Also, CO and other molecular spectral lines emission indicate that molecular clouds present subsonic and supersonic turbulence features, depending on the scale that is observed (STARK, 1984). The dispersion velocities (σ_v) show large values for the different ISM phases and specifically for molecular clouds, this quantity presents a universal line-width and mass distribution scaling relation. Larson (1981) and Solomon et al. (1987) found the following dependence: $\sigma_v \propto l^{\beta}$, with $\beta = 1/2$. The value of β has been obtained for many other studies in molecular clouds from the Galaxy to neighboring satellite galaxies (*e.g.,* Heyer and Brunt (2004), Bolatto et al. (2008), Falgarone et al. (2009), Roman-Duval et al. (2011), among others). There is still some debate about the normalization and about slight variations in the slope. However, the common interpretation is the presence of turbulent gas motions that lead to these relations (see Heyer et al. (2009), Shetty

et al. (2012) and Hughes et al. (2013), for some examples).

Figure 3.6 - PDF of column density for four molecular clouds, derived from *Herschel* observations: two high latitude clouds, Spider (top-left) and Polaris (top-right), two other star-forming clouds, Monoceros R2 (bottom left) and Orion A (bottom-right). The left y-axis gives the normalized probability, the right y-axis is the number of pixels per log bin. The bottom x-axis is the visual extinction and the upper x-axis the logarithm of the normalized column density. The red line indicates a fit of a power law to the large values of A_V. The green curve indicates the expected log-normal PDF consistent with no star formation.

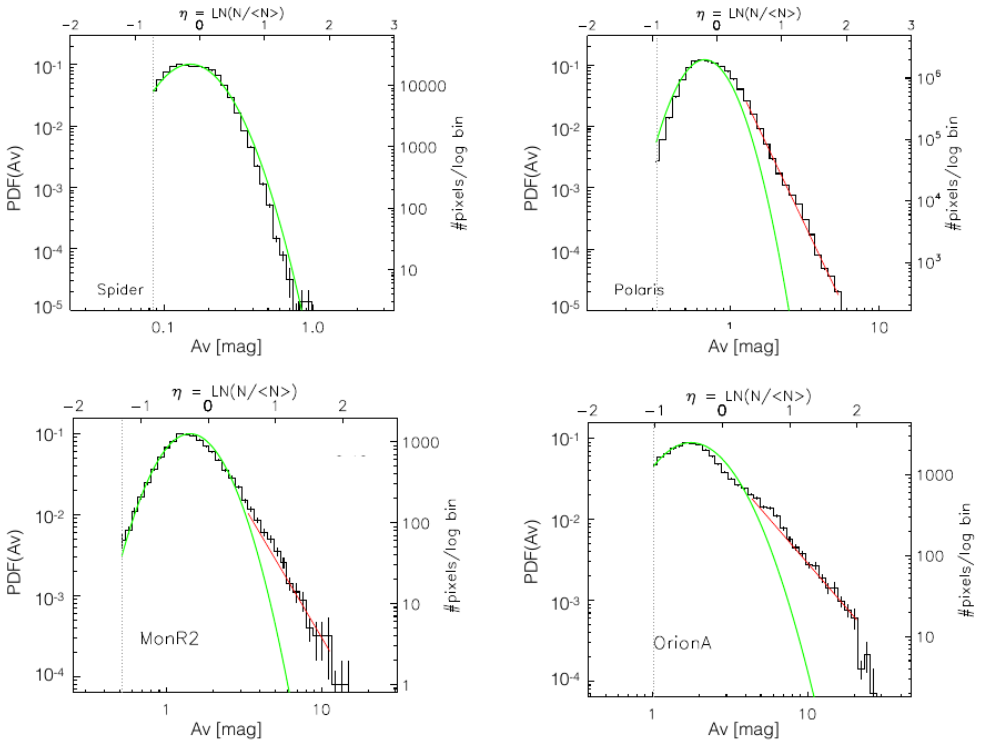

SOURCE: Schneider et al. (2015).

However, despite the use of power spectrum and probability density distributions of these quantities being useful tools for obtaining information about turbulence physics over different scales, they do not provide a full description of the turbulence properties. This can be understood by projection effects on the plane of the sky and the lack of phase information, an important quantity for a complete description in Fourier space. For this reason, more sophisticated statistical tools have been used

to provide information from observational quantities and their correlations with the properties of the turbulent medium.

One can say that the synergistic studies provided progress in our understanding of interstellar turbulence (see Cho et al. (2003), Schekochihin and Cowley (2007) and Beresnyak and Lazarian (2019) for details). The use of advanced analysis tools include high resolution simulations and refined statistics applied to high resolution observational data. This approach is not only insightful in the sense of understanding how different physical conditions affect interstellar turbulence, but also establish which analytical theory is suitable to characterize the different environments (see Cho et al. (2003) for more details). Figure 3.7 illustrates some galactic and extragalactic media and processes in which interstellar turbulence is crucial to understand the physical evolution and dynamics. We expect these regions to exhibit different turbulent features, which show up with different observational signatures (BURKHART, 2021).

Figure 3.7 - Illustration of some different astrophysical processes and environments that are related with MHD turbulence.

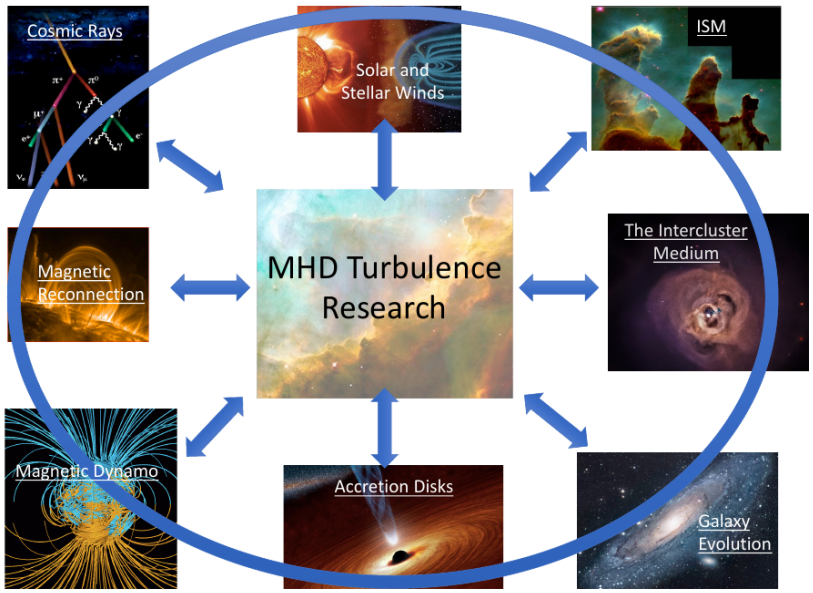

SOURCE: Burkhart (2021).

In addition, as explained in Chapter 2, the presence of magnetic fields heavily affects

the interstellar turbulence features. Hence, the comprehension of how the magnetic fields are correlated to other physical quantities is insightful not only to give guidelines to analytical models, but also to give hints on how to measure the relevant observational quantities (*e.g,* Falceta-Gonçalves et al. (2008) Iacobelli et al. (2013), Prosekin et al. (2016)). As mentioned in the previous section, one can directly study the properties of MHD turbulence with measurements such as: polarization, Faraday rotation and synchrotron fluctuations related to direction and gradients of the observables. Figure 3.8 presents on the left side an optical polarization map of the Musca Dark Cloud (PEREYRA; MAGALHÃES, 2004). As explained on Section 3.2, the polarization vectors present the same orientation as the magnetic field. On the right side of Figure 3.8, it is shown a polarization map superimposed on the column isodensity projection with similar physical conditions observed in the Musca Dark Cloud (FALCETA-GONÇALVES et al., 2008).

Figure 3.8 - Left side: optical polarization map of the Musca Dark Cloud (obtained from Pereyra and Magalhães (2004)). Right: synthetic polarization map obtained from a high resolution simulation of MHD turbulence (obtained from Falceta-Gonçalves et al. (2008)).

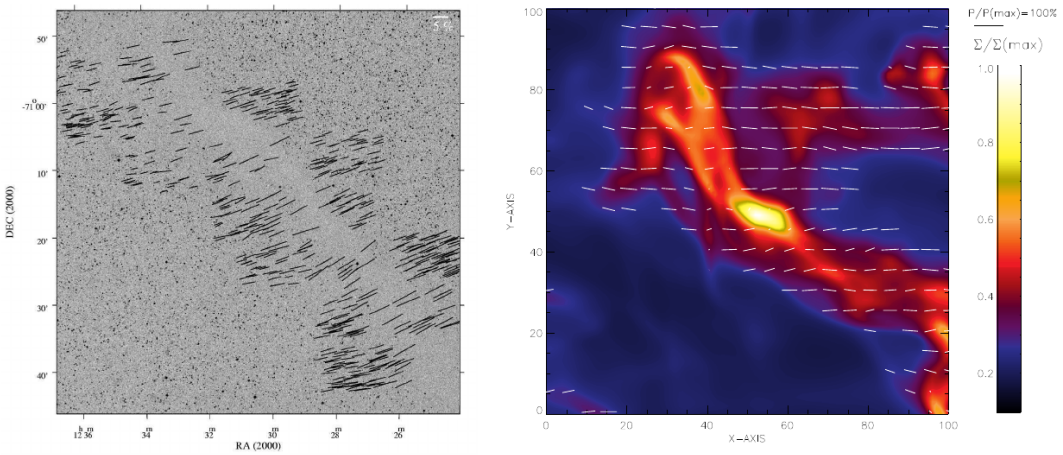

SOURCE: Falceta-Gonçalves et al. (2014).

In particular, synchrotron fluctuations have great potential to provide robust statistics that can be used to give insights on the magnetic turbulence properties (*e.g,* Lazarian and Pogosyan (2012), (BURKHART; LAZARIAN, 2012), Gaensler et al.

(2011)). Synchrotron intensity and polarization measurements are sensitive not only to the magnetic field morphology, but also to two important parameters that constrain MHD turbulence, in different regimes: the sonic and Alfvénic numbers. The following subsection will be devoted to examine in detail these parameters and show synchrotron measurements that have been critical in the context of interstellar turbulence.

3.3.1 Numerical simulations and physical parameters to describe interstellar turbulence

As mentioned in Chapter 2, the description of the astrophysical turbulence flow properties are based in statistical approaches. A useful way to simplify the study of MHD turbulence is to separate the different conditions, introducing parameters that provide clues to the comprehension of turbulence. A well known dimensionless parameter is the Reynolds number (Re), previously described in Chapter 2. For large Re values the flow becomes turbulent (FRISCH, 1995). The Reynolds number can be obtained in the interstellar measurements by the estimation of the size scale of the system, the line-of-sight non-thermal velocity obtained from spectral line observations, and the gas viscosity. The Reynolds number in the interstellar medium can be extremely large, around 10^9 (*e.g.,* Tauber et al. (1991). For instance, this value is larger than what can be reproduced by numerical simulations produced by current computational facilities, therefore the inertial range obtained from these will be order of magnitude shorter than that of the interstellar turbulence. The comparison between both must be done with caution.

Two other important parameters are the sonic Mach number ($\mathcal{M}_S$), defined as the ratio between the turbulent velocity and sound speed (KRUMHOLZ; BURKHART, 2016), and the Alfvenic Mach number ($\mathcal{M}_A$), which is the parameter that expresses the ratio of the turbulent velocity to the Alfven speed (TOFFLEMIRE et al., 2011). These parameters are defined by the following expressions:

$$\mathcal{M}_S \equiv \left\langle \frac{|\ \mathbf{v}\ |}{c_s} \right\rangle \qquad\qquad \mathcal{M}_A \equiv \left\langle \frac{|\ \mathbf{v}\ |}{v_A} \right\rangle \tag{3.11}$$

The Alfvén speed, v_A, represents the speed at which a signal can propagate along the magnetic field lines in the plasma of the ISM, and depends upon the strength of the magnetic field, and the density of the gas, as presented in Chapter 2.

In particular, the sonic and Alfvénic Mach numbers provide much coveted informa-

tion on the gas compressibility and magnetization of the media. The turbulent MHD physics can be studied into different conditions, using both parameters. Considering sonic Mach number: when the medium in which the velocity of the gas is less than the sound velocity, the regime is named as sub-sonic and $\mathcal{M}_S < 1$. Otherwise, when the velocity of the gas is larger than the sound velocity, the turbulent regime is known as super-sonic and $\mathcal{M}_S > 1$. For the Alfvénic Mach number: when the turbulent energy is smaller than the magnetic energy, $\mathcal{M}_A < 1$ and the turbulent medium is named sub-Alfvénic. For the case when the turbulent energy is larger than the magnetic energy, $\mathcal{M}_A > 1$ and the regime is know as super-Alfvénic. Normally, the MHD turbulence is studied and understood separately for each of these divisions, in order to constrain the different physical conditions existing in the different turbulent environments.

The understanding of turbulence in the interstellar medium is also carried out through different sub/super-subsonic sub/super-Alfvénic regimes. Many techniques have been developed. Many statistical techniques are aimed at obtaining these two parameters of turbulence in the interstellar medium and information on the physics of these regimes (BURKHART; LAZARIAN, 2011). They include the Delta Variance Analysis applied in simulated molecular clouds (*e,g.,* Stutzki et al. (1998); Ossenkopf et al. (2008)), Principal Component Analysis applied to spectral lines imaging studies (PCA; *e,g.,* Heyer and Schloerb (1997); Correia et al. (2016); Ensor et al. (2017)), Probability Density Functions (PDF) including the Tsallis Variant of the gas density and the magnetic field structure (*e,g.,* Federrath et al. (2008); Burkhart and Lazarian (2012); González-Casanova et al. (2018)), PDF of filamentary structures of HI column density (*e. g.,* Makarenko et al. (2018)), density bispectrum analysis (such as Genus; *e.g.,* Kowal et al. (2009); Chepurnov et al. (2008)), the Betti numbers calculation of the gas density fluctuations Makarenko et al. (2018), the Velocity Channel Analysis (VCA) and the Velocity Coordinate Spectrum (VCS) techniques for optically thick spectral lines in different absorbing media contexts (*e.g,* Lazarian and Pogosyan (2004); Lazarian and Hoang (2007), Lazarian and Pogosyan (2016)), among others.

These techniques present powerful methods to indicate the sensitivity of the sonic and Alfvénic numbers to different conditions of density, magnetic field and velocity. For example, the Alfvénic and sonic Mach numbers of a MHD turbulent region can be estimated applying the Tsallis formalism to fit the PDFs of density, velocity, and magnetic field strength, as shown by Tofflemire et al. (2011) for simulated regions of the diffuse interstellar medium. Since different observational techniques are nec-

essary to obtain these parameters, a physical quantity or method that could give straightforward information regarding both parameters could be valuable information of the environment.

3.4 Synchrotron fluctuations to understand interstellar turbulence

As mentioned previously, measurements of polarized synchrotron radiation and Faraday rotation provide an important insight into the perpendicular component of the magnetic field projected into the plane of the sky, and are powerful observational quantities to provide information of the interstellar turbulence. More recently, several authors have discussed the prospects of the use of radio polarization maps to study turbulence (*e.g.,* Haverkorn et al. (2004), Fletcher and Shukurov (2006), Beck (2008), Gaensler et al. (2011)).

The synchrotron measurements present information about the magnetic field, but they are also sensitive to the properties of the magnetoionic turbulence. A study related to this was presented by Shu (1977) who analyzed structure functions of polarization intensity and direction to estimate the difference between the slopes of these structure functions, in order to understand whether the observed emission was originated within or behind a region producing Faraday rotation. He showed that both information present similarities with the turbulent properties of the medium. Further, Haverkorn et al. (2008) used angular power spectra and structure functions of Stokes Q, U to probe the turbulence in the warm ionized medium, and Haverkorn et al. (2004) measured the structure function of observed rotation measure values to constrain the outer scale of turbulence in the warm ionized medium. Lazarian and Pogosyan (2012) also studied the correlation and structure functions of synchrotron intensity, and predicted that the fluctuations in synchrotron intensity show the imprints of anisotropy of MHD compressible turbulence. This anisotropy propagates in the same direction of the direction of the mean magnetic field.

In addition, many techniques based on synchrotron emission also have been successfully proposed to obtain information about the magnetic field of a turbulent medium. Lazarian and Pogosyan (2016) introduced two new techniques called Polarization Spatial Analysis (PSA) and Polarization Frequency Analysis (PFA) to extract information on the turbulent component of the magnetic field. These techniques are based on the calculation of the correlation functions of the complex polarization through an image map and provide information on the ratio of the strengths of the regular and random components of the magnetic field, the spectrum of the magnetic field fluctuations, and the correlation scale of Faraday rotation fluctuations. Lee et

al. (2016) numerically applied these techniques to mock polarized synchrotron emission maps and confirmed the theoretical prediction that synchrotron polarization fluctuations and magnetic field anisotropies are correlated. Zhang et al. (2016) used the PFA technique to obtain information on the statistics of the magnetic field and Faraday depth fluctuations.

Another important work that showed the great potential of the synchrotron quantities to provide robust statistics to understand the turbulence properties was presented by Gaensler et al. (2011). They showed the advantages of using polarization gradients applied to observations of the polarized Galactic emission, in order to trace spatial patterns. Using a comparison with simulations, it was demonstrated that turbulence in the warm-ionized medium has a relatively low sonic Mach number ($\mathcal{M}_S < 2$).

The polarization gradient calculated in Gaensler et al. (2011), $|\nabla \boldsymbol{P}|$, can be obtained by the following expression:

$$|\nabla \boldsymbol{P}| = \sqrt{\left(\frac{\partial Q}{\partial x}\right)^2 + \left(\frac{\partial U}{\partial x}\right)^2 + \left(\frac{\partial Q}{\partial y}\right)^2 + \left(\frac{\partial U}{\partial y}\right)^2}, \tag{3.12}$$

where the x and y axes are orthogonal directions in the plane of the sky, and have the property of being invariant under rotations and translations of the $Q-U$ plane. Rotations of the $Q-U$ plane can be caused by changing the reference frame used to measure the polarization angle, and so any physically meaningful quantity must be rotationally invariant in the $Q-U$ plane. Translations of the $Q-U$ plane can be caused by missing interferometer spacing when observing the sky, particularly missing 'zero-spacing' information that is provided by single-dish telescopes, and so translational invariance ensures that a quantity is robust to the limitations of interferometric techniques.

An image of a 18-square-degree patch of the Galactic plane, observed with the Australian Telescope Compact Array (ATCA) at a frequency of 1,4 GHz is shown in Figure 3.9 (MCCLURE-GRIFFITHS et al., 2001). The inset shows an expanded view of the structure of gradients and the blue vectors indicate the direction of the polarization gradients. In addition, comparing the filament structures of the observation with numerical simulations covering a range of sonic Mach numbers, they found that the structures seen in the warm ionized medium present a relatively low sonic Mach number. Gaensler et al. (2011) work is supported by Burkhart and Lazarian (2012),

who constructed mock polarization gradient images for polarized emission propagating through a Faraday rotating medium in simulations of MHD turbulence with different Mach numbers. They found that polarization gradient images for supersonic simulations present filaments with a double jump profile at the sites of shock fronts, while subsonic cases present filaments with single jump profile that are due to the random fluctuations in the rotation measure along the line of sight. Transonic simulations have both types of filaments present. In addition, they show that the skewness, kurtosis, and genus of the polarization gradient structures are sensitive to the sonic Mach number. Similar quantities and studies were presented by Herron et al. (2018b) and Herron et al. (2018a) to trace information from the magneto-ionic turbulent medium, such as generalized polarization gradient, polarization directional derivative, polarization directional curvature, polarization wavelength derivative. Iacobelli et al. (2013) analyzed the synchrotron fluctuation properties in a turbulent fluid using power spectra, and were able to constrain the outer scale of the turbulence and the ratio of random to total magnetic field strengths.

Figure 3.9 - Polarization gradient image of the Southern Galactic Plane Survey. The inset shows an expanded view of part of the image, with blue lines used to denote the direction of the polarization gradient.

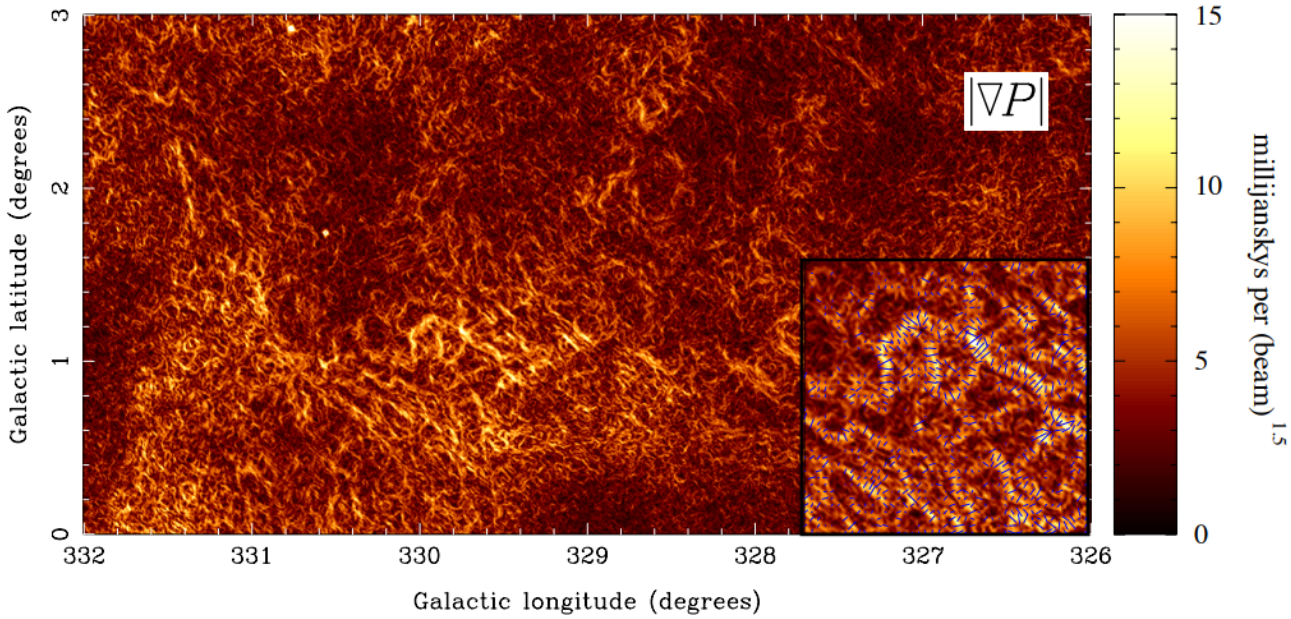

SOURCE: Gaensler et al. (2011).

Recently, Lazarian et al. (2017) and Lazarian et al. () extended the analysis of synchrotron gradient quantities to obtain information about a turbulent medium. They showed that using synchrotron intensity gradients (SIG) and synchrotron polarization gradients (SPG) one can obtain information about the magnetic field in the magneto-sonic turbulent medium. The new probes have been proven successful, providing information about the structure of the magnetic field.

These gradients successfully provide estimates of the magnetic field geometry and intensity without the effects of Faraday rotation. The estimation of the magnetic field structure using synchrotron gradients has the advantage of being a direct measurement. Moreover, synchrotron observational data are obtained using interferometric telescopes and with the existence of high resolution data of different regions of the interstellar medium, this measurements can be a powerful tool to understand the dynamics and origin of that medium. Since these techniques present a new approach in obtaining an accurate estimate of the interstellar magnetic field and are central points to this thesis, we will detail the subject in the next section.

3.5 Synchrotron gradients in turbulent medium

As mentioned previously, the use of different statistical techniques for the analysis of polarization gradients, presented by Gaensler et al. (2011) and also Burkhart and Lazarian (2012), showed that the use a complex polarized vector can be applied to determine the Alfvénic Mach number of the interstellar turbulence. Based on this breakthrough discovery and the work presented by González-Casanova and Lazarian (2017), which showed the relation between velocity gradients and the direction of the magnetic field, Lazarian et al. (2017) and Lazarian and Yuen (2018) presented a new theory capable of identifying the relation between the direction of the Synchrotron Intensity Gradients (SIGs), Synchrotron Polarization Gradients (SPGs) and the underlying magnetic field. This discovery presents a valuable application in the context of the interstellar turbulence. Since this thesis is devoted to explore the application of these tools, this section will present a general description of the theory of these synchrotron quantities in the context of MHD turbulence and the relationship with magnetic field.

The understanding of the synchrotron gradients relies on the modern theory of strong non-relativistic MHD turbulence presented by Goldreich and Sridhar (1995) (see more details in Chapter 2). This turbulent model is based on anisotropic fluctuations scaling, which propagate in the same direction of the mean magnetic field. Subsequently, Lazarian and Vishniac (1999) extended this work, showing that mag-

netic reconnection does not present an impediment for the motions of a magnetic fluid that mixes in the direction perpendicular to the local direction of the magnetic field. In this picture, the anisotropic turbulent eddies trace the local direction of magnetic flux tubes and consequently, measurements of velocity or/and magnetic field gradients should reveal the magnetic field direction. The perpendicular turbulent mixing results in the scale-dependent anisotropy of MHD turbulence and makes the essential distinction between MHD and hydrodynamic turbulence.

For sub-Alfvenic regime, the magnetic field is weakly perturbed in a range between the turbulence injection scale, L, and the transition scale $l_{trans} = LM_A^2$. For scales smaller than l_{trans}, the fast turbulent reconnection enhances the mixing of the eddies in the direction perpendicular to the local magnetic field. Lazarian and Vishniac (1999) (LV99) provided the eddy mixing theory description of MHD turbulence. The energy transfer (dissipative or cascade) via eddies mixing has a correspondence with the size of eddies. The relationship between the aforementioned eddy scales follows:

$$l_{\parallel} \approx L \left(\frac{l_{\perp}}{L} \right)^{2/3} M_A^{-4/3} \, , \tag{3.13}$$

where $l_{\parallel}$ and $l_{\perp}$ are the parallel and perpendicular eddy scales relative to the local magnetic field; $M_A = v_L/v_{\rm A}$ is the Alfvén Mach number, with v_L being the injection velocity, and $v_{\rm A} = B/\sqrt{4\pi\rho}$, the Alfvén speed (more details can be seen in LV99). Notice that Equation (3.13) is similar to that formulated for the trans-Alfvénic ($M_A = 1$) regime in Goldreich and Sridhar (1995), with a new dependence on M_A.

From Equation (3.13), one can infer that the anisotropy ratio of the eddies increases as the scales decrease. Therefore, simulations to investigate MHD anisotropies should be done at the smallest scales possible (as is the case of this work). According to González-Casanova and Lazarian (2017), velocity gradient $v_l/l_{\perp}$ increases as the scales decrease:

$$v_l/l_{\perp} \approx \left(\frac{V_A M_A^{4/3}}{L^{1/3}} \right) l_{\perp}^{-2/3} \, . \tag{3.14}$$

In the super-Alfvénic regime ($M_A > 1$), the magnetic field is weak. Consequently, the kinetic energy dominates and therefore the energy cascade follows closely the Kolmogorov description up to a scale

$$l_A = LM_A^3. \tag{3.15}$$

For scales smaller than l_A, the magnetic field modifies the dynamics of the medium and the turbulence cascade presents the same features as proposed by Goldreich and Sridhar (1995), where the anisotropy of the velocity field becomes similar to that of the sub-Alfvénic regime. In other words, the turbulence is hydrodynamic and the velocity gradients are weakly correlated with the magnetic fields. Also, the anisotropic perturbations are aligned with the local magnetic field. One can see that the intrinsic properties of the eddies imprinted by both regimes of Alfvénic turbulence imply not only the condition of a preferential direction along the local magnetic field, but also that the eddy velocity depends on the size of the eddies. The elongated eddies have the largest velocity gradient perpendicular to the their longest axis. Hence, it is expected that the direction of the maximum velocity gradient to be perpendicular to the local magnetic field.

The use of velocity gradient techniques to estimate the local magnetic field morphology was introduced by González-Casanova and Lazarian (2017) using numerical simulations and comparisons with other well-known techniques. In that work, the authors used velocity channel gradients to validate the new way to infer the magnetic field properties. Subsequent analysis showed that velocity gradients can also be obtained by other diagnostics such as the velocity centroid maps (VCG) and velocity channel maps (VChG). Within the VCG context, the calculation of gradients is performed using 2D spectroscopy maps of velocity centroids, while for the VChG technique the calculation of the gradients uses the intensities within the channel maps. Both VCGs and VChGs are readily available from the Doppler-shifted spectroscopic data. There is also an additional possibility named the intensity gradient (IG) technique, which is based on the intensity from both gas and dust emission. We note that the IG technique should be distinguished from the Histograms of Relative Orientation (HRO) technique, proposed by Soler et al. (2013), which requires polarimetry data to define the direction of the magnetic fields. The IG technique is a polarization-independent method and is a way of finding the magnetic field direction, using the sub-block averaging method. This gradient technique is more affected by shocks, providing information from regions in such a condition. However, the IG technique has the limitation of being a less reliable tracer of the magnetic fields in supersonic turbulent conditions.

In addition, Lazarian and Pogosyan (2016) predicted that synchrotron emission gra-

dients can also imprint turbulence signatures traceable by velocity gradients (locally aligned with the magnetic field). Using the argument that magnetic field and velocity are correlated in Alfvénic turbulence, attested that gradients of turbulent quantities that are direct related to the magnetic field should have the same property as the gradients of velocity. As gradients are linear operation then if we have a quantity that is an integral of magnetic fluctuations along the line of sight, as this is the case of synchrotron fluctuations. This work opened the venues to study the synchrotron emission from our Galaxy and beyond. Lately, Lazarian et al. (2017) and Lazarian and Yuen (2018) numerically confirmed that synchrotron intensity gradients and synchrotron polarization gradients can indeed be used to infer the magnetic field properties. Combining measurements of polarization with the synchrotron provides several ways to obtain synergy from the two measurements and increase the reliability of magnetic field tracing.

Since the synchrotron intensity gradients are not subjected to Faraday rotation, they do not require multiple frequency measurements to compensate for the effect. One additional advantage is that measuring intensity is easier than measuring polarization. Moreover, Lazarian et al. () showed that synchrotron polarization gradients combined with a multi-frequency technique Faraday tomography, can be used to trace the 3D magnetic field structure. These different observational techniques to study astrophysical magnetic fields are important since the interstellar medium presents distinct physical and chemical conditions. In this thesis, we particularly intend to explore the synchrotron gradients to infer other physical properties of the turbulent astrophysical fluids and their correlations.

4 GRADIENTS IN SYNCHROTRON EMISSION MAPS – MHD SIMULATIONS

The numerical simulations produced in this work were carried out with a multidimensional numerical code, called ZEUS-MP[1]. This code was first implemented by Hawley and Stone (1995). This chapter aims to describe the numerical code responsible for performing the high resolutions maps shown in this work; the parameters considered to reproduce different conditions of the interstellar medium and finally, the construction of synthetic maps of gradients of polarization and synchrotron intensity. The first section will present the MHD equations set in a conservative form, as used to perform the calculation of the data cubes simulations. The second section introduces an overview of each numerical method which in a simulation. Finally, the third section presents the regimes selection of simulation samples, representing conditions commonly observed in molecular clouds, such as cases where supersonic turbulent energy is dominant or weaker than magnetic field energy, simulations where auto-gravity is the ruling regime or regions where this effect can be neglected.

4.1 The ZEUS-MP numerical code

The simulations performed in this work result in three-dimensional data cubes, generated by spatial and temporal solutions of the MHD equations via a numerical approach. The ZEUS-3D code solves the equations of ideal, compressible MHD equations using a finite difference scheme and a von Neumann artificial viscosity to capture shocks structure. It is similar to different codes used by our group, developed for the study of problems such as: the intergalactic medium (e.g Kulesza-Żydzik et al. (2009) and Kulpa-Dybeł et al. (2011)), clusters of galaxies (*e.g.,* Falceta-Gonçalves et al. (2009) and Falceta-Gonçalves et al. (2010)), star formation (*e.g.,* Santos-Lima et al. (2012) and Pino et al. (2009)), magnetic re-connection (*e.g.,* Kowal et al. (2007) and Kowal et al. (2009)), cosmic rays (*e.g.,* Kowal et al. (2011) and Kowal et al. (2012)), among others.

There are four different versions of ZEUS. The first code initially developed by Norman et al. (1980) presented a numerical one-dimensional solution for the collapse and evolution of rotating interstellar gas clouds during star formation. The second version, ZEUS-2D, is a two-dimensional version, able to solve hydrodynamic, magnetohydrodynamic and radiative hydrodynamic equations (Stone and Norman (1992a), Stone and Norman (1992b), Stone et al. (1992)). The following version,

[1] `http://www.netpurgatory.com/zeusmp.html`

ZEUS-3D, is a three dimensional version of the previous ones. The latest, ZEUS-MP, is a parallelized three dimensional magnetohydrodynamic version, suitable for high resolution simulations of astrophysical problems. This code was developed at the Laboratory for Computational Astrophysics (LCA) of the National Center for Supercomputing Applications (NCSA) at the University of Illinois (KRITSUK et al., 2011). The algorithm is based on finite differences on a staggered mesh (see Stone and Norman (1992a) and Stone and Norman (1992b)). The temporal evolution is obtained through explicit flows between cells of the computational grid, known as Riemann solver approximation (see Toro (2013) for more information). It also includes a second-order-accurate, monotonic advection scheme (see Leer (1977) and Miyoshi and Kusano (2005) for more information). The advection is performed in a series of directional sweeps that are cyclically permuted at each time step. In addition, a linear reconstruction method (second order) is used to interpolate the core values of conservative variables. In order to emulate the interstellar turbulence, periodic boundary conditions and solenoidal turbulence injections are applied in our simulations. The code performs different resolutions in the MHD data cubes with values of density, velocity, magnetic field for different physical conditions defined by the user. An illustration of how the data cubes indicating different cells can be observed in Figure **??**.The next topics aim to describe the main steps for the numerical solution of equations.

4.1.1 Matrix form of MHD equations

The family of ZEUS codes was developed to integrate a set of conservation laws, which can expressed in the following way:

$$\frac{\partial \mathbf{U}}{\partial t} + \nabla \cdot \mathbf{T}(\mathbf{U}) = \mathbf{S}(\mathbf{U}) \tag{4.1}$$

where $\mathbf{U}$ corresponds to the set of conservative variables; and $\mathbf{T}(\mathbf{U})$ and $\mathbf{S}(\mathbf{U})$ correspond, respectively, to the flows (that is, the flow of the variable $\mathbf{U}$ per unit of time and area) and source term for each $\mathbf{U}$ component.

The simulations consider the case of turbulence generated by ideal MHD equations, presented in Chapter 2. In order to rewrite these equations according to Equation 4.1, one can express them as following:

$$\frac{\partial}{\partial t}\begin{pmatrix}\rho\\ \rho B\\ E\\ B\end{pmatrix} = -\nabla\cdot\begin{pmatrix}p\mathbf{v}\\ \rho\mathbf{v}\mathbf{v}-\frac{1}{\mu_0}\mathbf{B}\mathbf{B}-\mathbf{I}\left(P+\frac{\mathbf{B}\mathbf{B}}{4\pi}\right)\\ \left(E+P+\frac{\mathbf{B}^2}{8\pi}\right)\mathbf{v}-\frac{(\mathbf{v}\cdot\mathbf{B})\mathbf{B}}{4\pi}\\ \mathbf{v}\mathbf{B}-\mathbf{B}\mathbf{v}\end{pmatrix}+\begin{pmatrix}0\\ \rho\mathbf{f}\\ \rho\mathbf{v}\cdot\mathbf{f}\\ 0\end{pmatrix} \tag{4.2}$$

where ρ , $\mathbf{v}$ and p and denote density, velocity, and pressure, respectively and E is the energy. The term $\mathbf{f} = \mathbf{f_{turb}}$ is the external acceleration driving source in which turbulence is included. The pressure P is related to e through an equation of state.

For this work, the internal energy is considered to be lost from the system via radiation on timescales very much shorter than dynamical timescales, and P can be obtained by the following isothermal equation of state:

$$P = C_s\rho \tag{4.3}$$

Finally, the energy term E can be defined as the energy density of the gas and the family of ZEUS codes considers the simplest case of an adiabatic gas of non interacting particles, for which the equation of state takes the simplified form:

$$E = \frac{p}{(\gamma-1)} + \frac{\rho\mathbf{v}^2}{2} + \frac{\mathbf{B}^2}{8\pi} \tag{4.4}$$

As the space discretization is performed in terms of a grid of cubic elements, the set of Equations 4.2 can be mathematically expressed in terms of their Cartesian coordinates, taking the following form (see Stone et al. (2008) for the full mathematical derivation):

$$\frac{\partial\mathbf{U}}{\partial t} - \frac{\partial\mathbf{F}}{\partial x} - \frac{\partial\mathbf{G}}{\partial y} - \frac{\partial\mathbf{H}}{\partial z} = \mathbf{S}, \tag{4.5}$$

where $\mathbf{F}$, $\mathbf{G}$ and $\mathbf{H}$ correspond to the fluxes in the x, y and z directions, respectively. These flux terms can be represented in matrix form as:

$$\mathbf{F} = \begin{pmatrix} \rho v_x \\ \rho v_x^2 + P + B^2/2 - B_x^2 \\ \rho v_x v_y - B_x B_y \\ \rho v_x v_z - B_x B_z \\ (E + P + B^2/2)\, v_x - (\mathbf{B} \cdot \mathbf{v})\, B_x \\ 0 \\ B_y v_x - B_x v_y \\ B_z v_x - B_x v_z \end{pmatrix} \tag{4.6}$$

$$\mathbf{G} = \begin{pmatrix} \rho v_y \\ \rho v_y v_x - B_y B_x \\ \rho v_y^2 + P + B^2/2 - B_y^2 \\ \rho v_y v_z - B_y B_z \\ (E + P + B^2/2)\, v_y - (\mathbf{B} \cdot \mathbf{v})\, B_y \\ B_x v_y - B_y v_x \\ 0 \\ B_z v_y - B_y v_z \end{pmatrix} \tag{4.7}$$

$$\mathbf{H} = \begin{pmatrix} \rho v_z \\ \rho v_z v_x - B_z B_x \\ \rho v_z v_y - B_z B_y \\ \rho v_z^2 + P + B^2/2 - B_z^2 \\ (E + P)\, v_z - (\mathbf{B} \cdot \mathbf{v})\, B_z \\ B_x v_z - B_z v_x \\ B_y v_z - B_z v_y \\ 0 \end{pmatrix} \tag{4.8}$$

Because the physical properties of the gas are provided for the center of the volume element (cell) of the computational grid, it is important to emphasize that the calculation of the fluxes between cells is done after a numerical interpolation step. The interpolation procedure must ensure the continuity, and positivity of pressure and density.

The numerical integration of the above equations used by the ZEUS-MP code is obtained through a finite-volume formalism and a Godunov-type algorithm (see Toro (2013) and Bodenheimer (2006) for more information). This algorithm consists

of three main steps: (a) a reconstruction routine, where the values of the variables are interpolated from the center to the faces of each cell in the computational grid; (b) the solution of Riemann's problem for the left and right side flows in the cell interfaces; (c) by a temporal advance. A more detailed description of the ZEUS-MP code for each time step will be presented in the next discussions.

4.1.2 Numerical grid discretization

One of the initial steps to make grid-based algorithms solve a partial differential equation is the representation of the dependent variables on a numerical mesh. The continuous independent variable x is transformed into discrete values in each coordinate direction, considering a finite domain; the discretization is performed using a three-dimensional Cartesian grid of size $L_x \times L_y \times L_z$; with N_x, N_y and N_z being the number of cells in the three directions. These cells are indicated by indices (i, j, k), and the central position of each of them is defined by de equally spaced values of $\Delta x = L_y/N_y$, $\Delta x = L_y/N_y$ and $\Delta z = L_z/N_z$, respectively. The ZEUS-MP family is based in staggered meshes, which consider scalar variables (pressure, density, etc.) stored in the cell centers of the control volumes, whereas the velocity or momentum variables are located on the corresponding cell faces with a normal vector perpendicular to them, as presented in Figure 4.1.

Figure 4.1 - The variables in the ZEUS-MP code for one computational cell. The scalar quantities (*i.e.,* ρ and R) are located at the cell center, while vector quantities are face-centered.

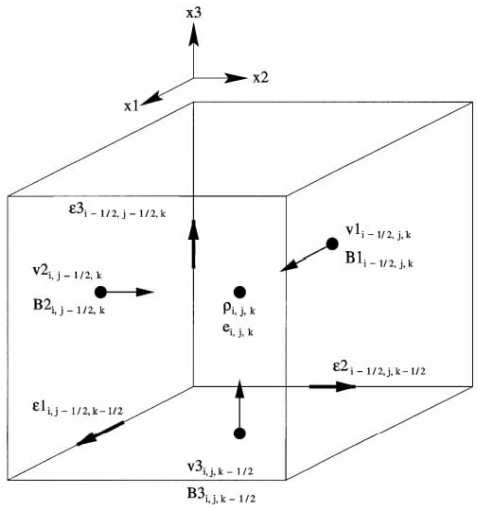

SOURCE: Hayes et al. (2006).

The time is discretized into N steps between the initial moment, t_0, and the final moment, t_f, defined by the user. Each instant of time will be indicated by the index n, so that the time step at a given instant will be defined as $\delta t^n = t^{n+1} - t^n$. It is important to notice that the choice of timestep can not be arbitrary, because otherwise, for long time steps, it is possible that all the material in a cell be advected through to neighbor cells in a single step. This could lead to errors, such as negative pressure and densities. Hence, the choice of the timestep must satisfy a stability constraint. The ZEUS family of codes obey the Courant–Friedrichs–Lewy (CFL) condition: $\Delta t \leq \Delta x / u_{max}$, where u_{max} is the maximum speed in the simulation domain. In the case of a 3D simulation, the CFL condition on the y and z dimensions must also be considered. Since u_{max} is time-dependent, the condition must be checked at each timestep.

4.1.3 Finite-volume scheme

The ZEUS-MP code is based on the operator-split solution procedure to solve Equations 4.2 (except the induction equation, that will be explained on the following subsections). This technique can be applied using two separate steps: transport and source steps. In the first one, the equations are updated in conservative form using higher-order upwind methods. For the source step, a simple finite differences scheme is used to evaluate the terms of Equations 4.2. Hence, the method separates the original equation into two parts over a time step, separately computes the solution for each part, and then combines the two separate solutions to form a solution for the original equation. The induction equation is updated with an entirely different method, since the operator of the split method cannot give an accurate solution for the magnetic field evolution.

The source step solves the MHD terms of Equations 4.2 computed through cell boundaries, without the induction equation (last equation of the matrix). Hence, the quantity $\mathbf{U}$ becomes a vector that depends on the mass density, momentum density, and energy density. The transport step is based on a formalism known as finite volume method, which considers that cells on the grid hold a single value for fluid properties given by the cell averaged values. Therefore, vector $\mathbf{U}$ can be obtained from a spatial average, expressed by:

$$
\begin{aligned}
U_{i,j,k}^{n+1} = & U_{i,j,k}^{n} - \frac{\Delta y}{\Delta t}\left(\mathbf{F}_{i+1/2,j,k} - \mathbf{F}_{i-1/2,j,k}\right) \\
& - \frac{\Delta x}{\Delta t}\left(\mathbf{G}_{i,j+1/2,k} - \mathbf{G}_{i,j-1/2,k}\right) \\
& - \frac{\Delta z}{\Delta t}\left(\mathbf{H}_{i,j,k+1/2} - \mathbf{H}_{i,j,k-1/2}\right)
\end{aligned} \tag{4.9}
$$

where:

$$
\mathbf{U}_{i,j,k}^{n} = \frac{1}{\Delta x \Delta y \Delta z} = \int_{z_k-1/2}^{z_k+1/2}\int_{j_k-1/2}^{j_k+1/2}\int_{x_k-1/2}^{x_k+1/2} \mathbf{U}\left(x, y, x, t^n\right) dxdydz \tag{4.10}
$$

corresponds to the spatial average (within each cell) of the conservative variables, while

$$
\mathbf{F}_{i-1/2,j,k}^{n+1/2} = \frac{1}{\Delta x \Delta y \Delta z} = \int_{z_k-1/2}^{z_k+1/2}\int_{j_k-1/2}^{j_k+1/2}\int_{x_k-1/2}^{x_k+1/2} \mathbf{F}\left(x_{i-1/2}, y, z, t\right) dydzdt, \tag{4.11}
$$

$$
\mathbf{G}_{i,j-1/2,k}^{n+1/2} = \frac{1}{\Delta x \Delta y \Delta z} = \int_{z_k-1/2}^{z_k+1/2}\int_{j_k-1/2}^{j_k+1/2}\int_{x_k-1/2}^{x_k+1/2} \mathbf{G}\left(x, y_{i-1/2}z, t\right) dxdzdt, \tag{4.12}
$$

$$
\mathbf{H}_{i,j,k-1/2}^{n+1/2} = \frac{1}{\Delta x \Delta y \Delta z} = \int_{z_k-1/2}^{z_k+1/2}\int_{j_k-1/2}^{j_k+1/2}\int_{x_k-1/2}^{x_k+1/2} \mathbf{H}\left(x, y, z_{i-1/2}, t\right) dxdydt, \tag{4.13}
$$

correspond to the temporal and spatial average fluxes (in the face of each cell) $\mathbf{F}$, $\mathbf{G}$ e $\mathbf{H}$. The indexes $i \pm 1/2$, $j \pm 1/2$, $k \pm 1/2$ indicate the positions of the conservative variables on the faces (or interfaces) of each cell.

4.1.4 Divergence of B

The ZEUS code presents an accurate method to obtain the induction equation solutions using an innovative algorithm based on Constrained Transport (CT), which is a robust method in which the magnetic field values are treated both in the center and in the faces of each cell of the computational grid, preserving the divergence-free condition for each cell imposed by Maxwell's equations. The Method of Charac-

teristics (MoC) is a second order interpolation scheme which uses quantities that are upwind with respect to the MHD wave modes. As presented in Chapter 2, the magnetic field is responsible for new degrees of freedom to a physical system, and different wave modes need to be considered in a MHD fluid. For example, Alfvén waves couple directly to the magnetic induction equation and, when treated numerically, require knowledge of the fluid's quantities upwind. Therefore, these modes are computed in a separate step. In order to solve this problem, the MoC approach uses Stokes' theorem to express the rate of change of magnetic flux across a surface **S**; the magnetic field solution can be expressed in terms of a electromotive force ε (see Evans and Hawley (1988) for the mathematical description):

$$\begin{aligned} B^{n+1/2}_{x,i-1,j,k} =& B^{n}_{x,i-1,j,k} - \frac{\Delta t}{\Delta y}\left(\varepsilon^{n+1/2}_{z,i-1/2,j+1/2,k} - \varepsilon^{n+1/2}_{z,i-1/2,j-1/2,k}\right) \\ & - \frac{\Delta t}{\Delta z}\left(\varepsilon^{n+1/2}_{y,i-1/2,k+1/2} - \varepsilon^{n+1/2}_{y,i-1/2,k-1/2}\right), \end{aligned} \tag{4.14}$$

$$\begin{aligned} B^{n+1}_{y,i,j-1,k} =& B^{n}_{y,i,j-1,k} - \frac{\Delta t}{\Delta x}\left(\varepsilon^{n+1/2}_{z,i+1/2,j-1/2,k} - \varepsilon^{n+1/2}_{z,i-1/2,j-1/2,k}\right) \\ & - \frac{\Delta t}{\Delta z}\left(\varepsilon^{n+1/2}_{x,i,j-1/2,k+1/2} - \varepsilon^{n+1/2}_{z,i,j-1/2,k-1/2}\right), \end{aligned} \tag{4.15}$$

$$\begin{aligned} B^{n+1}_{z,i,j,k-1} =& B^{n}_{z,i,j,k-1} - \frac{\Delta t}{\Delta x}\left(\varepsilon^{n+1/2}_{y,i+1/2,j,k-1/2} - \varepsilon^{n+1/2}_{y,i-1/2,j,k-1/2}\right) \\ & - \frac{\Delta t}{\Delta y}\left(\varepsilon^{n+1/2}_{x,i,j+1/2,k-1/2} - \varepsilon^{n+1/2}_{x,i,j-1/2,k-1/2}\right), \end{aligned} \tag{4.16}$$

where

$$B^{n}_{x,i,j-1,k} = \frac{1}{\Delta y \Delta z}\int_{z_k+1/2}^{z_k+1/2}\int_{y_{j+1/2}}^{y_{i-1/2}} B_y(x_{i-1/2}, y, z, t^n)dydz, \tag{4.17}$$

$$B^{n}_{y,i,j-1,k} = \frac{1}{\Delta x \Delta z}\int_{z_k+1/2}^{z_k+1/2}\int_{x_{j+1/2}}^{x_{i-1/2}} B_y(x, y_{i-1/2}, z, t^n)dxdz, \tag{4.18}$$

$$B^{n}_{z,i,j,k-1} = \frac{1}{\Delta y \Delta z}\int_{y_{j+1/2}}^{y_{k-1/2}}\int_{x_{j+1/2}}^{x_{i-1/2}} B_z(x, y, z_{i-1/2}, t^n)dxdy, \tag{4.19}$$

correspond to the spatial means (in the face area of each cell) of the three components of the magnetic field, and

$$\varepsilon^{n+1/2}_{x,i,j-1/2,k-1} = \frac{1}{\Delta x \Delta t} \int_{t^{n+1}}^{t^n} \int_{x_{i+1/2}}^{x_{i-1/2}} \varepsilon_x(x, y_{j-1/2}, z_{k-1/2}, t) dx dt, \tag{4.20}$$

$$\varepsilon^{n+1/2}_{y,i-1/2,j,k-1} = \frac{1}{\Delta y \Delta t} \int_{t^{n+1}}^{t^n} \int_{y_{i+1/2}}^{y_{i-1/2}} \varepsilon_y(x_{j-1/2}, y, z_{k-1/2}, t) dy dt, \tag{4.21}$$

and

$$\varepsilon^{n+1/2}_{z,i-1/2,j-1/2,k} = \frac{1}{\Delta z \Delta t} \int_{t^{n+1}}^{t^n} \int_{z_{i+1/2}}^{z_{i-1/2}} \varepsilon_z(x_{j-1/2}, y_{k-1/2}, z, t) dz dt, \tag{4.22}$$

correspond to the temporal and spatial means (along the edges of each cell of the ε component.

4.1.5 Reconstruction method

The reconstruction of the primitive variables inside the computational grid cells, starting from the central values or from the faces (or both), is obtained according to the Total Variation Diminishing method (TVD). In this approach, a monotonic function condition is satisfied. This prevents the creation of spurious errors in the proximity of the interfaces between the cells. The three well-known type of piecewise representations are: constant, linear and parabolic. In ZEUS-MP, a linear piecewise scheme is used, with a linear interpolation between cell centers. Once reconstruction has been done, we have a cell interface with a discontinuity in the value of the quantities across the cell boundaries. Based on this quantities, we have to compute the flow. This is usually referred to as a Riemann problem.

4.1.6 Riemann problem using HLLD solver

Central schemes can be considered as Riemann problem due to the straightforward central-difference approximation of the space derivatives to determine the advection terms of the hyperbolic Equations 4.1. These numerical fluxes, also named Riemann solvers, are known to be an important tool in the context of numerical schemes for conservation laws, and consist of a piecewise initial values for two constant states, separated by a jump discontinuity. Over the years, attention has been to the the scheme by the numerical fluid dynamics community, in order to develop an efficient Riemann solver. A well-known solver used for the MHD equations is the HLLD - an improvement of the classical HLL (Harten, Lax, Van Leer) solution - Toro (2013),

and is based on separating the flux term into four intermediary states $\mathbf{Q}_L^*$, $\mathbf{Q}_L^{**}$, $\mathbf{Q}_R^*$ and $\mathbf{Q}_R^{**}$, divided in five waves $\mathbf{S}_L$, $\mathbf{S}_L^*$,$\mathbf{S}_M$. $\mathbf{S}_R^*$ and $\mathbf{S}_R$, as illustrated in Figure 4.2.

Figure 4.2 - The eigenvalues of waves generated by the local solution of the Riemann problem at the cell interfaces, using the HLLD solver.

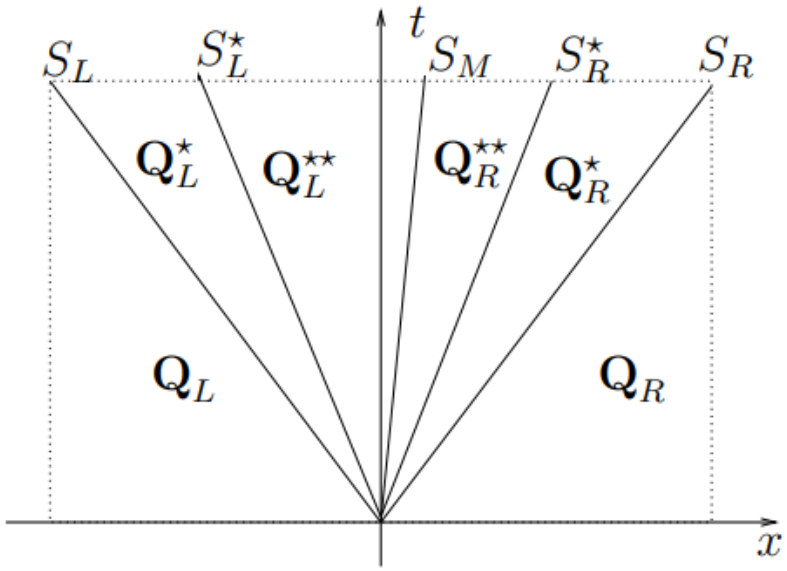

SOURCE: Adapted by Miyoshi and Kusano (2005).

Figure 4.2 illustrates the structure with four intermediate states and the five waves used for calculating the numerical flow in HLLD. Also,it can be noted that the eigenvalues obtained from Equation 4.2 are the same MHD waves obtained in Chapter 2. The function that calculates the numerical fluxes using HLLD solvers is given by:

$$\mathbf{F}_{i+1/2}^{n-1/2} = \begin{cases} \mathbf{F}_L & \text{if } S_L > 0 \\ \mathbf{F}_L^*, & \text{if } S_L \leq 0 \leq S_L^*, \\ \mathbf{F}_L^{**}, & \text{if } S_L^* \leq 0 \leq S_M, \\ \mathbf{F}_R^{**}, & \text{if } S_M \leq 0 \leq S_R^*, \\ \mathbf{F}_R^*, & \text{if } S_R^* \leq 0 \leq S_R, \\ \mathbf{F}_R & \text{if } S_R < 0 \end{cases} \tag{4.23}$$

In the above equations, S_L and S_L correspond to the smallest velocity to the left and the greatest velocity to the right of the discontinuity, respectively. The complete description of the calculation of each flux state, and wave division for numerical MHD solutions can be obtained in Miyoshi and Kusano (2005). More information regarding Riemman problem for partial differential equations can be seen in Toro (2013).

4.2 Initial and boundary conditions

This work used numerical simulations with a three-dimensional box with periodic boundary conditions, considering an ideal MHD system. In order to reproduce different conditions of the interstellar medium, and statistically analyze the properties of the synchrotron gradients, high resolution MHD numerical simulations were carried out. The computational domain is $792 \times 792 \times 792$ in Cartesian coordinate system (x,y,z). Each data cube keeps spatial and temporal information regarding density, velocity and magnetic field for every cell.

In this code, the root mean square (rms) of the density is maintained approximately unity, so that v can be viewed as the velocity measured in units of the rms velocity of the system with the Alfvénic velocity in the same units. Also, the rms velocity induced by turbulence in the box is close to unity (in code units), i.e, for the cases studied, the turnover time of the energy-carrying eddies. Finally, the magnetic field can be decomposed into two parts: the uniform background $\mathbf{B}$ and a fluctuating $\mathbf{b}$ field. We initially set $\mathbf{b} = 0$, with $\mathbf{B}$ along the x direction.

The turbulence is driven solenoidally, at a spatial scale about 2.5 times smaller than the box size, L (in all the simulations, $L = 1$, in code units), by adding a turbulent term in the forcing part of Equation 2.15. This scale defines the injection scale in the Fourier space of our models, to minimize the influence of the forcing on the generation of density structures. Density fluctuations are generated later on by the interaction of MHD waves. Density structures in turbulence can be associated with the slow and fast modes (CHO; LAZARIAN, 2002).

Since our focus is to obtain information regarding the magnetization level in a MHD turbulent scenario, we present numerical models of compressible turbulence for a broad range of Mach numbers. The statistics of density fluctuations in MHD turbulence is basically related to the sonic Mach number M_S. The modeling of shocks reveals that supersonic motions lead to compression that, in the isothermal approximation, result in the $\delta\rho/\langle\rho\rangle \sim M_S^2$ relation. This is the main cause for the broad

Table 4.1 - Simulation parameters.

M_S	M_A	$\beta = 2M_A^2/2M_S^2$	Description
7.31	0.22	0.002	Sub-Alfvénic
6.10	0.42	0.01	Sub-Alfvénic
6.47	0.61	0.02	Sub-Alfvénic
6.14	0.82	0.04	Trans-Alfvénic
6.03	1.01	0.06	Trans-Alfvénic
6.08	1.19	0.08	Trans-Alfvénic
6.24	1.38	0.10	Super-Alfvénic
5.94	1.55	0.14	Super-Alfvénic
5.80	1.67	0.17	Super-Alfvénic
6.55	1.71	0.19	Super-Alfvénic

log-normal PDF of density fluctuations in isothermal turbulence (see Kowal et al. (2007), for more information). On the other hand, M_A is linked to the dispersion and decorrelation length of B fluctuations (BEATTIE et al., 2022). Larger M_A result in shorter decorrelation lengths (i.e., larger power at short wavelength fluctuations) and larger amplitudes of perturbations compared to the mean field. Small values of M_A, on the contrary, are related to large decorrelation lengths and small amplitudes of $\delta B/\langle B\rangle$. In order to avoid combined effects of density fluctuations in the statistics of polarization vectors, this work made use of models with similar M_S, and consequently, a similar PDF of density fluctuations. Regarding M_A, the models were divided into three groups corresponding to sub-Alfvénic ($B > 1.0$), trans-Alfvénic ($B \sim 1.0$) and super-Alfvénic ($B < 1.0$) turbulence. The numerical parameters are listed in Table 4.1, in a sequence of ascending values of mean magnetization given by β. The domain $M_A < M_S$ corresponds to the simulations with magnetic pressure larger than the thermal pressure (and consequently $\beta > 1$), while the domain $M_A > M_S$ corresponds to the cases where the thermal pressure is larger than the magnetic pressure. The relatively large values of M_S in Table 4.1 is justified since the range of smaller values was explored in previous works, such as: Yuen and Lazarian (2017), Lazarian et al. (2017), Lazarian and Yuen (2018), among others.

The viscosity and diffusion were not set explicitly in our models. The scale at which the dissipation starts to act is defined by the numerical diffusivity of the scheme. However, the numerical scheme used in the ZEUS-MP code is considered to be of relatively low diffusion (NORMAN et al., 1980). It is important to highlight that numerical diffusion depends not only on the adopted numerical scheme but also on the "smoothness" of the solution, so it changes locally in the system. In addition,

it is also a time-varying quantity. However, the dissipation scales can be estimated approximately from the velocity spectra. The estimation of diffusity in the same models considered in this work can be found in Cho and Lazarian (2010).

4.3 Scaling setup conversion to real physical unities

The results obtained in this work are expected to be applicable to the interstellar medium. Hence, in the context of the choice of appropriate values of density, temperatures and other physical quantities, scaling is very important to confront with astronomical observations. The simulations used are isothermal, and self-gravity is neglected, therefore the solutions may be understood as scale-free. In this sense, we expect the physical quantities can be re-scaled (BURKHART et al., 2009). An example of such scaling can be seen in Hill et al. (2008). Under an isothermal assumption, those authors set temperature, length, and density of simulated data to match the average values observed in the warm and hot ionized media. It is important to highlight that the scaled models obtained in this work matched the warm ionized medium very well with respect to what is expected in these regions. A similar scheme of scaling in analogous simulations was used by Falceta-Gonçalves et al. (2008).

We aim to analyze the properties of synchrotron gradients in a turbulent context and find ways to estimate the magnetization level. In order to achieve this objective, the synthetic synchrotron emission maps were obtained. The construction of the maps and the calculation of the gradients from synchrotron quantities will be explained in the next chapter. However, before this explanation, it is important to note that depending on some physical conditions, the synchrotron quantities can be severely affected (see Equations 3.4 to 3.8, Subsection 3.2.3). For example, low values of electronic density can affect the statistical properties of the Faraday depth, a quantity that can affect the estimation of synchrotron polarization.

In order to avoid this, we set real observed average values observed in the interstellar medium for the physical quantities that can influence the calculation of synchrotron emission intensity, synchrotron polarization and Faraday decorrelation. The calculation of these quantities considers a typical box length scale $L_{box} = 1$ kpc. The scale factor for the mean gas density is $n \sim 0.03\ cm^{-3}$, and the mean magnetic field B_{ext} along the x direction has a strength of $10.3\,\mu$G and zero for the z and y directions. The three fluctuating components of the magnetic field were initially set to dispersions $\sigma_x = 2\,\mu$G, $\sigma_y = 3\,\mu$G and $\sigma_z = 2\,\mu$G, similar to that found in the ISM ($\sim 2\,\mu$G). We emphasize that the regular field, local to the simulated volume, would only contribute to the polarized intensity of the synthetic observations, unlike those

observed in external galaxies. Polarization measurements in external galaxies are performed with comparatively lower spatial resolution. They are mostly sensitive to the ordered component of the magnetic field within the beam, or to the large-scale regular fields, and therefore, in external galaxies, the ordered fields are observed to be about three times weaker than the turbulent fields. The fact that the MHD simulations are isothermal and we have assumed that there is no ultraviolet radiation field in the simulated volume makes the ionization fraction, $f_{ion} = 0.5$ for neutral hydrogen, constant throughout the volume and time evolution, and can be used to compute the free electron density. We also assume that the thermal electron number density, n_e, is proportional to n. An initial simulation was run with $n_e \sim 0.01\ cm^{-3}$. To investigate the case in which Faraday rotation is important, a simulation with $n_e = 0.13\, cm^{-3}$ ($\sim 100\,\%$ ionization fraction) was run. We expect stronger Faraday depolarization in this case and this is discussed in Section 6.3. Values of n_e considered in this work are expected in region of hot and warm ionized media (see Pynzar' (2016) and Cordes and Lazio (2003)).

Since this work also intends to investigate how Faraday rotation affects the results obtained using synchrotron polarization gradients, the synchrotron gradients are computed at different observational frequencies. The real physical values considered above avoid low Faraday depolarization effects. For example, for the simulation with $M_A = 0.2$, the Faraday rotation depths at 1.0 GHz ranges from -1.5 to 3.3 $rad.m^{-2}$, with a mean value of 0.7± 0.1 $rad.m^{-2}$. For $M_A = 1.0$, the values range from -18 to 26 $rad.m^{-2}$, and the mean is $5 \pm 1\ rad.m^{-2}$. Next chapter will be devoted to present the construction of the mock synchrotron maps.

5 SYNTHETIC SYNCHROTRON GRADIENTS DIRECTIONS: TOP-BASE AND CIRCULAR STATISTICS METHODS TO OBTAIN ALFVÉNIC MACH NUMBER

This chapter is devoted to the calculation of the intensity and polarization synchrotron gradients, which are obtained from synthetic maps of simulated data, and how these quantities provide the magnetization level and associated Alfvén Mach number. Two methods will be described for obtaining the relevant quantities, but before presenting them we describe how to obtain the synchrotron polarization and intensity maps. The following section explains how the synchrotron gradients orientations were calculated. Finally, the third section will introduce the two methods: Top-Base and circular statistics to directly obtain quantitative values for the Alfvén Mach number. Finally, to demonstrate the statistical reliability of the methods, an error analysis within a Bayesian framework will be presented in the last section. This chapter and Chapter 6 present the main results obtained on this thesis (CARMO et al., 2020).

5.1 Synthetic synchrotron emission maps

Using the output of the MHD simulations converted to physical units, the synthetic observations of synchrotron polarization and intensity emission are obtained from the data cubes, following Equations 3.4 to 3.8. The values assumed for input physical conditions are those typical for the diffuse interstellar medium. One of the results obtained for different values of electron density will be presented on the next discussions, in order to show the consistency of the analysis and the wide applicability of the results in the interstellar medium.

The numerical calculation of the intensity and orientation of the magnetic field is obtained locally for each cell (see explanation on the next section), which are then integrated along the line-of-sight (LOS) to produce a 2D image. An isotropic pitch angle distribution for the particles was assumed to obtain the mock synchrotron maps, with a power-law energy distribution of the electron population given by:

$$n_{\rm CRE}(E)dE = n_{\rm CRE}E^{2\gamma-1}dE \ , \tag{5.1}$$

where $n_{\rm CRE}(E)$ is defined as the number density of relativistic electrons with energies in the range between E and $E + dE$. The spectral index ($\gamma = 2$) was chosen following Lazarian and Pogosyan (2012), the first work that showed how gradients of polarization can be used to characterize the magnetic field. This choice allows a

direct comparison of our results to theirs.

The maps were constructed by assuming that there is a source region where both synchrotron emission and Faraday rotation effect occurs simultaneously. Under this consideration, the synchrotron intensity is obtained using real physical parameters described in Section 4.3. The equation used to numerically obtain the synchrotron intensity is the same as considered in Waelkens et al. (2009):

$$I(\mathbf{X}) \propto \int_0^{L_z} n_{\rm CRE} B_\perp^\gamma(\mathbf{X}, z) dz \ , \tag{5.2}$$

where L_z is the distance between the source region and observer, $\mathbf{X} = (x, y)$ is the two-dimensional position vector in the plane of the sky, $I(\mathbf{X})$ is the synchrotron intensity and $B_\perp = \sqrt{B_x^2 + B_y^2}$ is the magnitude of the perpendicular component of the magnetic field projected on the sky. On the left panel of Figure 5.1, the total synchrotron emissivity is shown as an example of the 3D synthetic emission obtained from the simulations. The right panel shows the 2D projected map of the total synchrotron intensity, $I(\mathbf{X})$, obtained by integrating the intensity along the z-direction in the cube (the direction of the line of sight). Since we have assumed a constant density of electrons, all the structures that show up are due to variations of the synchrotron emissivity caused by fluctuations of the magnetic field component in the plane of the sky.

Regarding the polarization maps, it is important to note this emission is partially linearly polarized (RYBICKI; LIGHTMAN, 1979), being susceptible to a birefringent effect known as Faraday rotation, as explained in Subsection 3.2.3 (*e.g.,* Haverkorn et al. (2004), Heiles and Haverkorn (2012), Zhang et al. (2016)). This magneto-optical effect causes the plane of polarization to rotate as radiation propagates along the plasma. In this work, maps with and without Faraday rotation will be produced, to compare how this effect can influence the results of the analysis involving synchrotron gradients orientations.

Figure 5.1 - The left side panel presents the 3D synchrotron emissivity per cell of the simulation. Synchrotron emissivity was computed assuming a constant electronic density in the volume. On the right panel, the 2D synchrotron intensity map obtained from the integration along the line of sight is presented, without considering Faraday rotation.

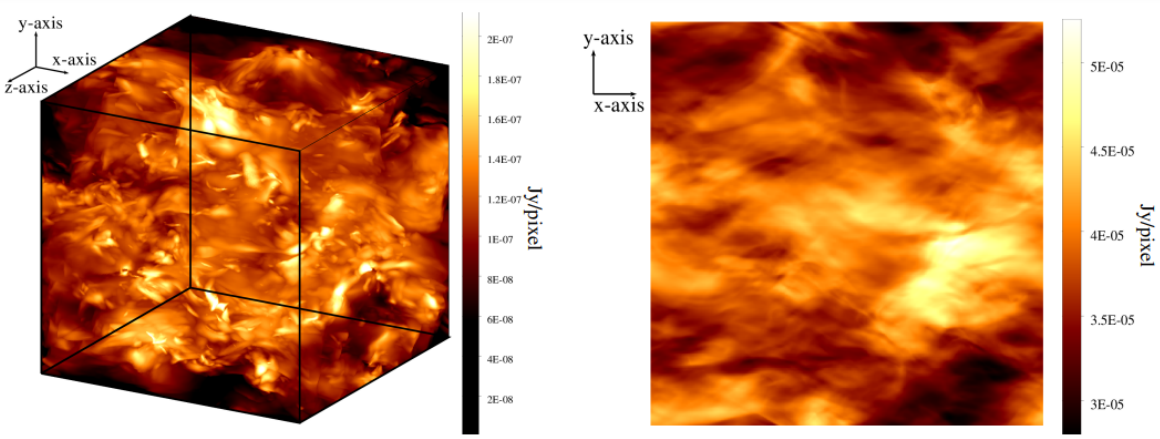

The intensity of the emission in the polarized synthetic maps, $P(\mathbf{X}, \lambda^2)$, at a given wavelength λ, was obtained by the following expression:

$$P(\mathbf{X}, \lambda^2) = \int_0^{L_z} P_i(\mathbf{X}, z) e^{2i\lambda^2 \theta_0(\mathbf{X}, z)} dz \,, \tag{5.3}$$

where the associated intrinsic polarization angle is $\theta_{\mathbf{0}}(\mathbf{X}, \mathbf{z})$ and

$$\phi(\mathbf{X}, z) = \theta_0(\mathbf{X}, z) + \lambda^2 \Phi(\mathbf{X}, z) \,, \tag{5.4}$$

with $\theta_0(\mathbf{X}, z)$ the intrinsic polarization angle:

$$\phi(\mathbf{X}, z) = \frac{\pi}{2} + \tan^{-1}\left(\frac{B_y}{B_x}\right) ., \tag{5.5}$$

and Faraday depth, $\Phi(\mathbf{X}, z)$, can be expressed as :

$$\Phi(\mathbf{X}, z) = 0.81 \int_0^{L_z} n_e(\mathbf{X}, z') B_z(\mathbf{X}, z') dz' \,, \tag{5.6}$$

where n_e is the number density of thermal electrons (in cm^{-3}), considered constant

in the simulations, and B_z is the LOS component of magnetic field (in μG), with the distance measured in parsecs.

The intrinsic polarization for each cell can be obtained in terms of stokes parameters. Assuming the polarization as a complex vector $P = Q + iU$, the intrinsic Stokes parameters Q and U are:

$$Q_i = pn_e \left(B_x^2(z) + B_y^2(z)\right) \qquad U_i = 2pn_e B_x(z) B_y(z), \tag{5.7}$$

Both cases, with and without ($\Phi(\mathbf{X}, z) = 0$) Faraday rotation were studied in this work. The expressions for Q and U can be found on synchrotron numerical works such as: Waelkens et al. (2009), Lazarian et al. (2017) and Lazarian and Yuen (2018). More details regarding the Stokes parameters can be found in Subsection 3.2.3, and for more information, see Lee et al. (2016). The numerical calculation of the synchrotron polarization and intensity gradients orientations is done using expressions 5.2, 5.3 and 5.7.

Figure 5.2 shows the representation of the polarization and intensity gradients vectors compared to the synchrotron polarization vector rotated by 90°. It is well established that synchrotron polarization can determine the direction of the magnetic field. The difference between the synchrotron gradients method to determine the properties of the magnetic field is the fact that, different from the conventional technique of synchrotron polarization vectors, the efficiency of the former is not distorted by Faraday rotation, and according to Lazarian et al. (), the resulting gradients are well correlated with other physical quantities.

Figure 5.2 - The synchrotron intensity vector, in red, and synchrotron polarization vector, in blue (rotated by 90°), for both sub-Alfvénic (top left) and super-Alfvénic (top right) simulations. The bottom panel shows a case with an intermediate Alfvénic Mach number. The $x-$ and $y-$scales are expressed in kiloparsecs.

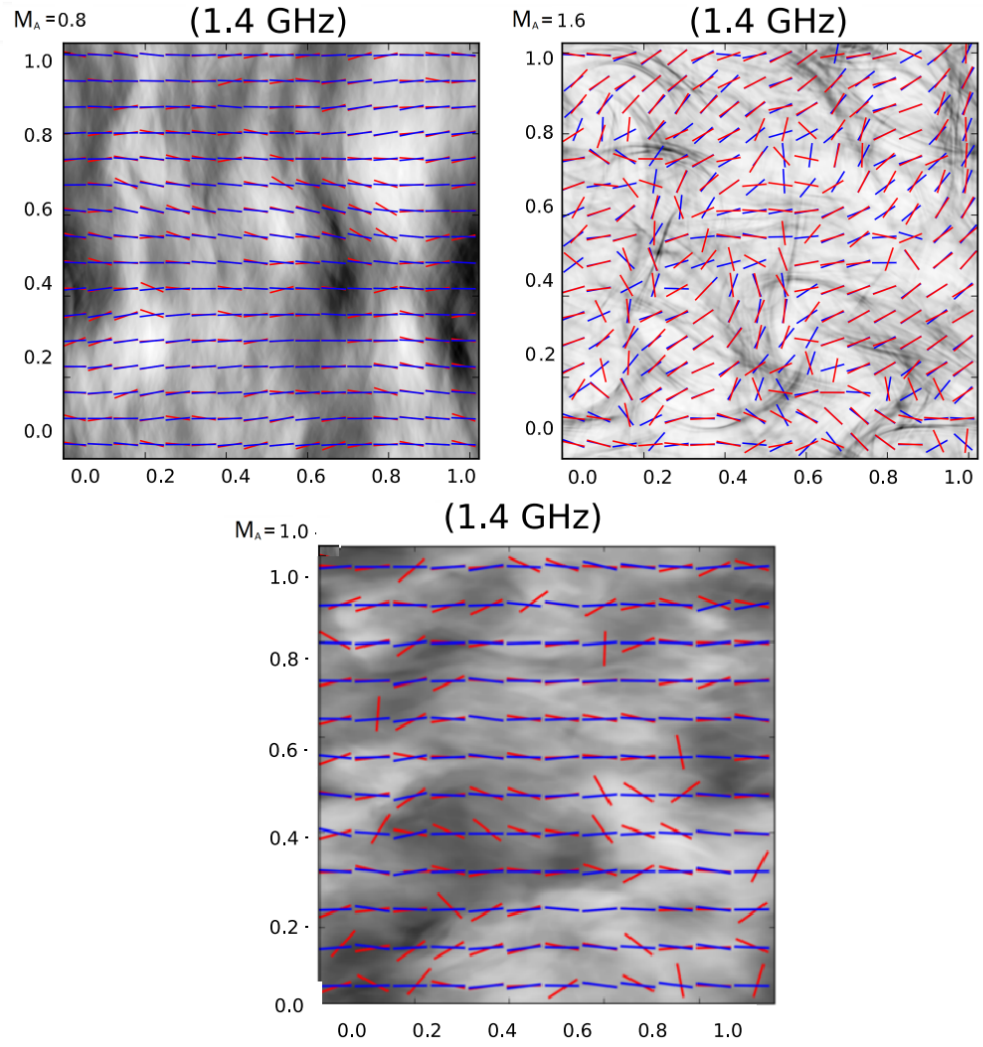

5.2 Synchrotron gradients maps and gradients angles distribution by Sobel operator

The 2D synchrotron gradients maps are calculated in this work using the same definition adopted by Soler et al. (2013), Lazarian et al. (2017) and Lazarian and

Yuen (2018). Both quantities are given by:

$$\nabla I = \left(\frac{\partial I}{\partial x}\right)^{l} \hat{x} + \left(\frac{\partial I}{\partial y}\right)^{l} \hat{y} \qquad \nabla P = \left(\frac{\partial P}{\partial x}\right)^{l} \hat{x} + \left(\frac{\partial P}{\partial y}\right)^{l} \hat{y}, \tag{5.8}$$

where ∇I denotes the synchrotron intensity gradient and ∇P is the synchrotron polarization gradient. The superscript l is related to the size of the area on which the gradient is calculated. In order to obtain the gradients with a certain precision and minimize the error caused by the discretization on the derivative calculation, this work used the same numerical approach adopted by Yuen and Lazarian (2017). The code is based on Soler et al. (2013) which uses a Sobel filter to calculate the gradients for each pixel on the projected intensity and polarization maps.

The Sobel operator performs a 2D spatial gradient measurement in images, using an edge-detection algorithm. The numerical procedure detects local discontinuities in the image, which typically occur on the boundary between pixels, reducing the noise introduced by them. The Sobel operator kernel is a 3×3 matrix that allows the calculation of the derivatives in a finite differences scheme with a Gaussian smoothing mask, and can mathematically be expressed by:

$$G_x = \begin{pmatrix} -1 & 0 & +1 \\ -2 & 0 & +2 \\ -1 & 0 & +1 \end{pmatrix} \qquad G_y = \begin{pmatrix} -1 & -2 & -1 \\ 0 & 0 & 0 \\ +1 & +2 & +1 \end{pmatrix}. \tag{5.9}$$

Note that this operator places an emphasis on pixels that are closer to the center of the mask. Also, it is important to highlight that the Gaussian noise reduction filter is is achieved by averaging over the vicinity of each pixel. The calculation to obtain ∇I_{sync} and ∇P_{sync} is equivalent to a convolution of the 2D maps with the Sobel Kernel, that is,

$$\nabla I_x = I \star G_x \qquad \nabla I_y = I \star G_y, \tag{5.10}$$

where, ∇I_x, ∇I_y, ∇P_x and ∇P_y are the are the x and y derivative components of intensity and synchrotron gradients, respectively, and $\star$ is the notation for convolution calculation. The magnitudes of the synchrotron intensity, $\nabla I\,(x, y)$, and polarization

$\nabla P\,(x, y)$ gradients, are calculated as follows:

$$\nabla I\,(x, y) = \sqrt{\nabla I_x^2 + \nabla I_y^2}. \qquad \nabla P\,(x, y) = \sqrt{\nabla P_x^2 + \nabla P_y^2}. \tag{5.11}$$

Also, the angle direction for each gradient can be calculated as:

$$\theta_{\nabla I} = \frac{1}{2}\arctan\left(\frac{\nabla I_x}{\nabla I_y}\right) \qquad \theta_{\nabla P} = \frac{1}{2}\arctan\left(\frac{\nabla P_x}{\nabla P_y}\right). \tag{5.12}$$

The plane of linear polarization and intensity gradient are oriented to be perpendicular to the direction of the magnetic field projected onto the sky. Hence, both $\theta_{\nabla I}$ and $\theta_{\nabla I}$ are measured anti-clockwise from North, the same way that the polarization angle vector is measured.

As mentioned before, the use of the gradients to explore the direction of the magnetic field was studied in previous works. In the context of turbulence, a gradient from a single pixel and its neighbors contains little statistical information and does not indicate the magnetic field direction reliably. However, the distribution of gradient orientations presents a well defined Gaussian profile, considering appropriate sizes of sub-regions in the image. Yuen and Lazarian (2017) proposed the sub-block averaging method, *i.e.,* obtaining a Gaussian fit to the directions distribution in selected sub-blocks, to statistically define the mean magnetic field in the corresponding sub-region.

As discussed by Hu et al. (2019c), using the code from Yuen and Lazarian (2017) to determine the size of sub-blocks allows the recovery of the gradients directions to a 95% confidence level. When the fitting error gets its minimum value, the corresponding sub-block size is the optimal selection. Using this well-tested code, the gradient angles and magnitudes can be obtained for each pixel. Figure 5.3 shows one example of ∇I and ∇P maps for a data cube with sub-Alvénic regime ($M_A = 0.8$), with Faraday rotation considered, in the frequency range of 100, 1.4, and 0.1 GHz.

The relationship between ∇I, ∇P, and the direction of magnetic field was discussed by Lazarian et al. (2017), Lazarian and Yuen (2018), Hu et al. (2019c), Hu et al. (2019b) and Zhang et al. (2019), and also summarized by Equations 5.10, 5.11 and 5.12. In this work, the attention will be devoted to characterize the distributions of angles and how these distributions are related to M_A. In an effort to investigate the correlations, two methods will be presented in the following section. Before that, the method for obtaining the uncertainties related to the quantities relevant for this

work will be explained.

Figure 5.3 - ∇I (top left) and ∇P images for a subsonic simulation with $M_A = 0.8$ (see Table 4.1) projected along the line-of-sight. The ∇P images were produced considering Faraday rotation, at frequencies of 100 GHz (top right), 1 GHz, and 0.1 GHz (bottom panels). The $x-$ and $y-$scales are expressed in kiloparsecs.

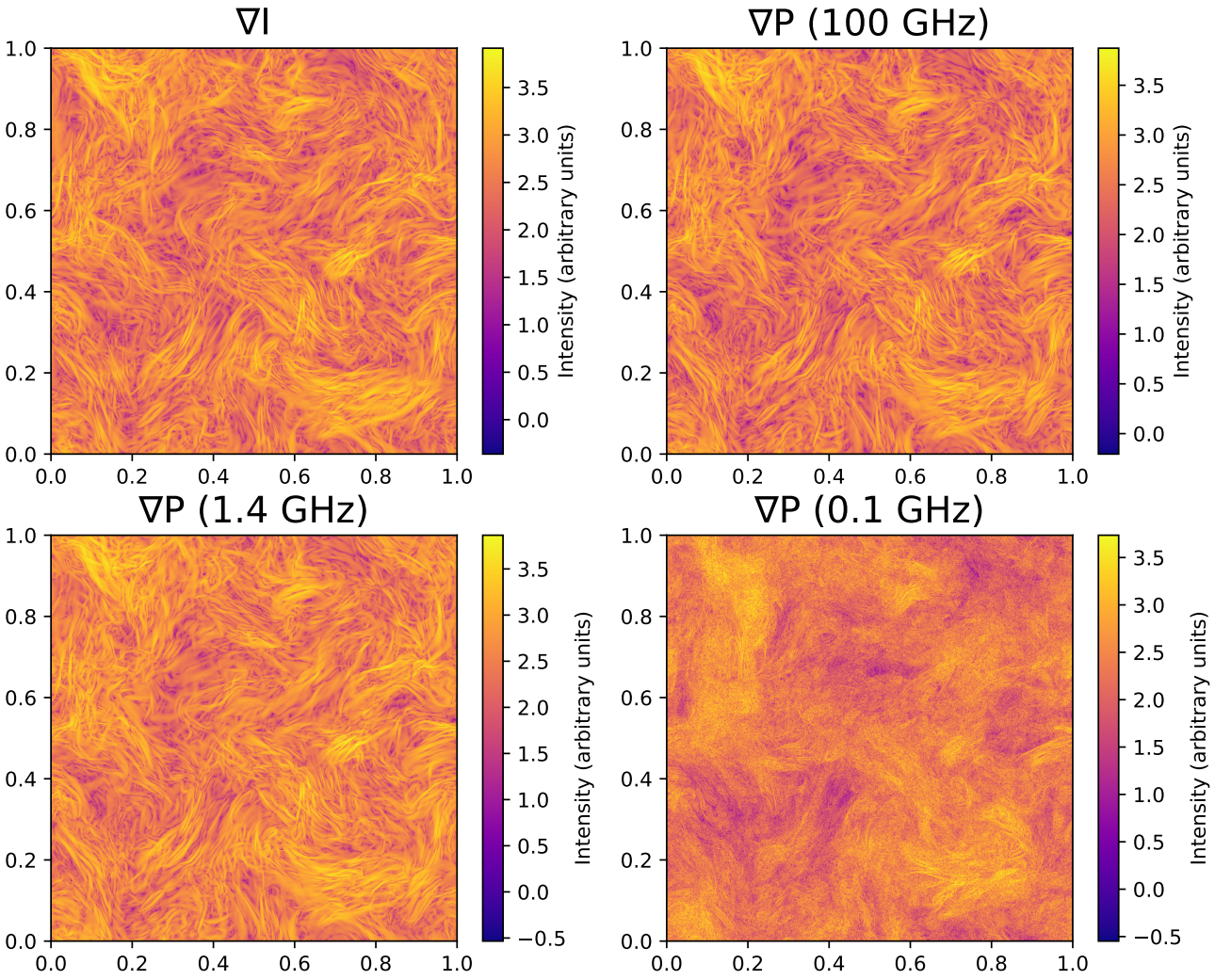

5.3 Error analysis

In order to analyze the relationship between two variables one can assume a probabilistic view of the problem in which a variable Y depends strictly on an observable

X, as follows:

$$Y = \beta X + \epsilon \, , \tag{5.13}$$

where β corresponds to the parameters of the model – in this case a linear one – and ϵ to the errors (which are assumed to be normally distributed). To find the best predictive model one can use Least Squares or a Maximum Likelihood approach to obtain β and ϵ. However, the same problem can be analyzed on a Bayesian framework, with advantages. In this approach, the model is seen as a probability distribution:

$$Y = \mathcal{N}(\beta X, \sigma^2) \, , \tag{5.14}$$

where Y is now a random variable that is normally distributed, with its mean being the linear predictor (βX) and with a variance of σ^2. β and σ correspond to distributions themselves given by:

$$\beta = \mathcal{N}(\mu_\beta, \sigma_\beta^2) \tag{5.15}$$

$$\sigma = |\mathcal{N}(\mu_\sigma, \sigma_\sigma^2)| \, . \tag{5.16}$$

Both Equations (5.15) and (5.16) are known as priors and they quantify the initial guesses in each linear model, characterized by a mean and standard deviation. Because all the variables correspond to probability distributions, at the end of the fitting process one can learn about the probability distributions of the parameters that give the best fit to the data (posterior distributions). The fitting process uses a Markov Chain Monte Carlo (MCMC) procedure that takes into account the information contents of the priors to obtain Y (SHARMA, 2017). The Bayesian analysis allows us to quantify any previous knowledge on our variables (priors) and to quantify the errors of the analysis (from the width of the posterior).

The independent variable is the Alfvén Mach number that is directly obtained from the MHD simulations, while the dependent variable is the Top-Base ratio, T/B, circular variance, V, or circular standard deviation, S. We first check, using the Bayesian Information Criterion, if a power-law is the simplest model to describe the relationship between the two quantities. We use a single power-law for the Top-Base method and two for the variance and standard deviation; one power-law for each Alvénic regime. The power-laws are fitted as a linear model, and the assumed

distribution and parameters for all priors are:

$$Y = \mathcal{N}(\beta M_A, \sigma^2), \tag{5.17}$$

$$\beta = \mathcal{N}(-1, 1)\ , \tag{5.18}$$

$$\sigma = |Cauchy(0.1, 2)|\ . \tag{5.19}$$

All the results (see Section 5.4) from the analysis done with a Bayesian approach use `Pymc3` (SALVATIER et al., 2016). `Pymc3` is a powerful Python package that implements Bayesian statistical model and fitting algorithms, including MCMC. Its flexibility and extensibility make it applicable to a large suite of problems. It runs a MCMC sampling to obtain the dependent variables and correspondent posterior distributions. For all fits we used 20,000 samples for each chain, with 16 chains running in parallel; the number of iterations to tune-up is 2,000. With the parameters selected we obtained a very robust convergence in all the chains (see Sharma (2017), Chapter/Section 3.7).

5.4 Top-Base and circular statistics method for synchrotron gradients orientations

In order to obtain the magnetization level after estimating the gradients ∇I and ∇P, we investigated how the related quantities are correlated with the Alfvén Mach number. The Top-Base and circular standard deviation methods, used to obtain the correlation with the synchrotron gradient angles distributions with M_A, will be explained on this section. It is important to highlight that different other methods, such as structure function, power spectra and other moments were tested to obtain ways to estimate M_A. However, any of them were effective as the two method that will be presented.

The first method used to obtain M_A is named as Top-Base method. In such technique, initially the distribution of gradient angles histogram is fitted with a Gaussian profile superimposed on a constant baseline B (see Figure 5.4), in the form:

$$F(\theta) = A\, e^{-\alpha(\theta-\theta_0)^2} + B, \tag{5.20}$$

where A is the amplitude, α controls the angle spread, θ is the direction of either ∇P or ∇I, with θ_0 being the mean value estimated. It is important to highlight that the estimation of the angle orientation θ for the gradients calculated on each cell

is the same of that explained in Section 5.1. Finally, using the fitting points, both values from the Gaussian peak and the baseline are determined.

Figure 5.4 - The histograms of angle distributions for synchrotron polarization gradients ($\theta_{\nabla P}$, top panels) and synchrotron intensity gradients ($\theta_{\nabla I}$, bottom panels) for three different Alfvén Mach numbers. The gradients where estimated after a smoothing kernel was applied to the data. The red dashed line corresponds to a Gaussian fit which allows us to estimate the Top (T) and Base (B) of the distributions that are used to estimate the magnetic field in the Top-Base method.

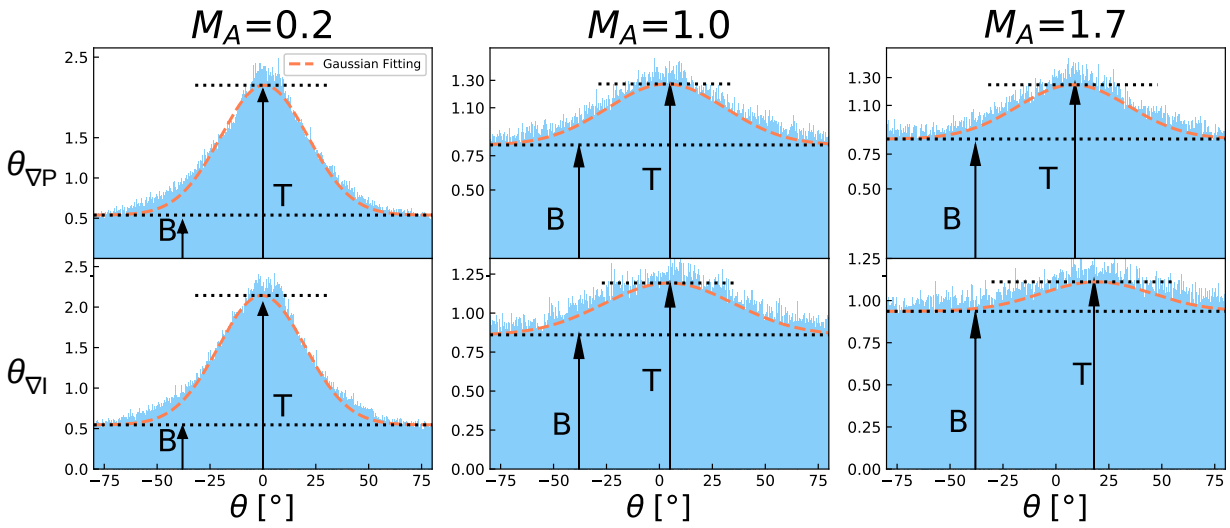

As seen in Figure 5.4, both ∇P and ∇I present well marked peaks for $M_A \leq 1$, while for $M_A > 1$ the peak is less pronounced. As M_A increases, the Top-Base ratio decreases as the gradients gradually loose correlation with the magnetic field. A similar behavior happens to velocity gradients and velocity channel gradients in the context of the VGT, as exlained in Yuen and Lazarian (2017). This is expected since for $M_A > 1$, the turbulent magnetic field become more isotropic and the gradients orientation gets less correlated with the magnetic direction.

Other method that presents correlation with M_A is based on an additional approach that analyses the angle spread from the synchrotron polarization and intensity gradients direction. Since the angles have a 2π periodicity, we use circular statistics instead of linear statistics. On the circle, measurements at 0° and 360° represent the

same direction whereas on a linear scale they would be located at opposite ends of a scale. For this reason circular data require specific analysis methods. More information about circular statistics can be found in Pewsey et al. (2013), (FISHER, 1995) and Batschelet (1981). In this statistics, one definition is circular variance, written as:

$$V = 1 - R \,, \tag{5.21}$$

where R is the mean resultant length defined as:

$$R = \frac{1}{N} \left\{ \left(\sum_{i}^{N} \cos\left(2\theta_i\right) \right)^2 + \left(\sum_{i}^{N} \sin\left(2\theta_i\right) \right)^2 \right\} \,, \tag{5.22}$$

and θ_i is the angle of either ∇P or ∇I for each cell with N as the total number of data points. The angle gradients are calculated with the same coordinates convention as for ψ. The circular standard deviation is defined as:

$$S = \frac{1}{2} \left\{ -2\ln\left(R\right) \right\}^{1/2} \,. \tag{5.23}$$

The factor of 2 in Equation (5.22) is related to the fact that synchrotron gradients are calculated in the interval 0 and 180. Unlike in linear statistics, the variance is bound for the interval $[0, 1]$ (FISHER, 1995). $V = 1$ means a flat distribution and $V = 0$ is the case if all angles are co-aligned. On the other hand, S is measured in the interval $[0, \infty)$, having properties similar to the linear standard deviation. Furthermore, because the standard deviation is not constrained, it is more susceptible to fluctuations, in particular in the super-Afvénic regime. Figure 5.5 shows the dependence of T/B, V and S with M_A for both ∇I and ∇P angle distributions. The well-defined power-law relationships (Table 5.1) can be used to directly estimate the magnetization level from the gradients. As seen, both the Top-Base and the standard deviation methods work well in the full range of magnetizations probed.

Table 5.1 - Power-Law relationships for the 3 different methods. The linear fitting uses a Bayesian approach to estimate the parameters and uncertainties.

Method		∇P	∇I
T/B		$1.6^{+0.01}_{-0.02} M_A{}^{-0.55^{+0.02}_{-0.01}}$	$1.4^{+0.03}_{-0.02} M_A{}^{-0.65^{+0.01}_{-0.02}}$
V	Sub-Alfvénic	$0.93^{+0.05}_{-0.08} M_A{}^{0.23^{+0.06}_{-0.07}}$	$0.90^{+0.06}_{-0.04} M_A{}^{0.20^{+0.08}_{-0.09}}$
	Super-Alfvénic	$0.95^{+0.05}_{-0.07} M_A{}^{0.04^{+0.03}_{-0.04}}$	$0.89^{+0.08}_{-0.04} M_A{}^{0.12^{+0.03}_{-0.02}}$
S	Sub-Alfvénic	$1.05^{+0.08}_{-0.09} M_A{}^{0.28^{+0.05}_{-0.04}}$	$1.04^{+0.01}_{-0.01} M_A{}^{0.24^{+0.06}_{-0.04}}$
	Super-Alfvénic	$1.22^{+0.03}_{-0.01} M_A{}^{0.16^{+0.10}_{-0.09}}$	$1.05^{+0.02}_{-0.02} M_A{}^{0.31^{+0.05}_{-0.07}}$

Figure 5.5 - The relationships between the Top-Base ratio (T/B, *Top panel*), the circular variance (V, *Middle panel*) and the circular standard deviation (S, *Bottom panel*) with respect to the Alfvén Mach number for both ∇I (*cyan*) and ∇P (*brown*). The regions $M_A < 1$ (sub-Alfvénic) and $M_A > 1$ (super-Alfvénic) are treated separately for V and S. The trend lines are estimated using a Bayesian approach, that allows realistic uncertainty estimates, in this case 1σ, for both ∇I and ∇P. The relevant parameters of the power-law fits can be found in Table 5.1.

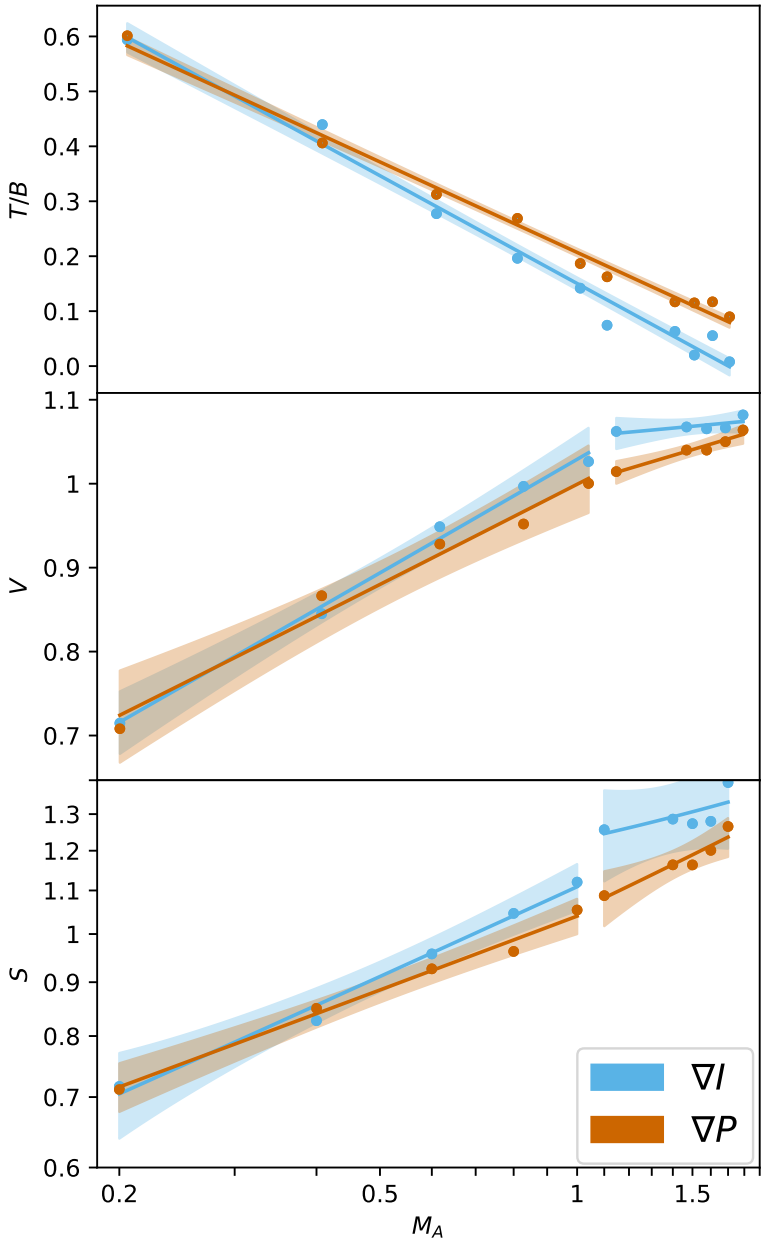

6 THE CORRELATION BETWEEN SYNCHROTRON GRADIENT DIRECTIONS AND M_A FOR DIFFERENT OBSERVATIONAL CONDITIONS

A compact version of the discussions in this Chapter is presented in Carmo et al. (2020).

6.1 Signal-to-noise considerations

Real observations have intrinsic noise. In order to understand the effects of noise on both T/B and S presented in Figure 5.5, we added zero-mean Gaussian white noise to the synthetic maps on a pixel by pixel basis. This is trivially done for I. If the noise has standard deviation σ_N and the total pixel map intensity is I, S/N $= I/\sigma_N$. However, adding zero-mean Gaussian noise pixel by pixel to Q and U is tricky, since the result can be both positive and negative, and therefore the average flux over these maps can be zero. In order to provide a realistic description, we define the S/N in total intensity and compute the noise distribution for that. Then we use the same noise distribution statistics for the Stokes Q and U maps.

A 2D Gaussian kernel with a spatial $\sigma = 2$ pixels is used to smooth the maps for the evaluation of ∇I and ∇P. The results are presented for S/N = [2, 5, 10, 15, 50, 100] in the total intensity map.

The ∇I and ∇P power-laws as functions of M_A in the presence of noise can be obtained by the same procedure described before, using a Bayesian analysis approach which allows a fair estimate of uncertainties. We obtained both gradients for 10 values of M_A and 6 different S/N ratios. We applied the procedure for the Top-Base ratio and the circular standard deviation methods. Figure 6.1 shows the effects of the S/N on the synchrotron gradients considering the ∇I case. We found the same behavior for the ∇P case. Notice that sub- and super-Alfvénic regimes are treated separately.

For the circular standard deviation method, it is clear that for S/N $\gtrsim 5$ the method behaves well and one can properly derive the Alfvén Mach number (for the sub-Alfvénic regimes). For the super-Alfvénic regime a single value of S can correspond to multiple values of the Mach number. Considering 1σ errors, only an upper limit to the magnetic field strength can be obtained. The relationship between S and M_A with 1σ errors for ∇I is:

$$M_A = \begin{cases} 0.84^{+0.11}_{-0.09}\ S_I^{3.6^{+0.3}_{-0.3}}\ , & \text{if } M_A < 1\ . \\ 0.93^{+0.10}_{-0.04}\ S_I^{3.8^{+0.7}_{-0.5}}\ , & \text{if } M_A \geq 1\ , \end{cases} \tag{6.1}$$

and for ∇P :

$$M_A = \begin{cases} 0.85^{+0.09}_{-0.11}\ S_P^{4.2^{+0.7}_{-0.8}}\ , & \text{if } M_A < 1\ . \\ 0.85^{+0.07}_{-0.05}\ S_P^{3.2^{+0.4}_{-0.6}}\ , & \text{if } M_A \geq 1\ . \end{cases} \tag{6.2}$$

We see in Figure 6.1 that T/B versus M_A is more sensitive to the S/N ratio, and should be used only in cases of S/N $\gtrsim 5$.

Figure 6.1 - Power-law fits of the circular standard deviation (S, *Top panel*) and Top-Base ratio (T/B, *Bottom panel*) as functions of the Alfvén Mach number for the SIG. The different colors correspond to different S/N ratios, with a case without noise (only possible in computer simulations) added. The regions $M_A < 1$ (sub-Alfvénic) and $M_A > 1$ (super-Alfvénic) are treated separately. In the top panel, only the uncertainties (1σ and 2σ) for the trend lines of S/N= 2 and S/N=100 are shown, for better visualization. The power-law fits and uncertainties are estimated with a Bayesian approach. The ∇P (not shown) has a similar behavior as the ∇I with respect to the effects of noise levels.

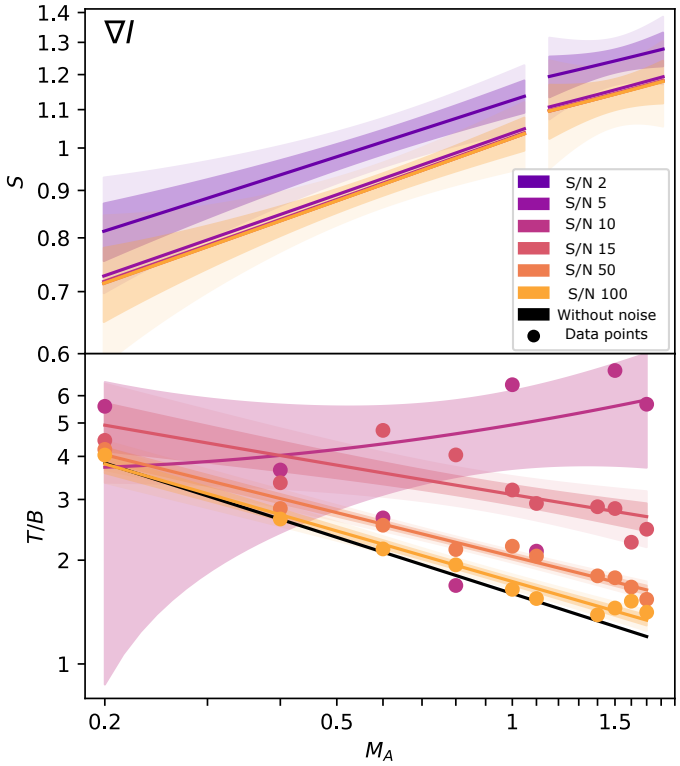

6.2 Influence of the mean magnetic field direction

It is important to understand how the projection effects may change the results from synchrotron gradient direction techniques. The mean magnetic field $\langle B \rangle$, is oriented parallel to the x-axis and varies with respect to the LOS with an angle α (i.e., rotates

around the y-axis). The LOS and the mean magnetic field are perpendicular for $\alpha = 0°$, and parallel for $\alpha = 90°$. Considering different values of α, the 3D data cubes produce the following projected quantities: $B_x = \langle B \rangle \cos\alpha$, and $B_z = \langle B \rangle \sin\alpha$. Thus, approaching 90° gives the largest ($\sin 90° = 1$) mean field contribution to the Faraday depth. Figure 6.2 indicates a schematic visualization of a cube rotation around de $y-$axis, indicating the direction of the mean magnetic field (red arrows) and the LOS (black arrows). In order to guarantee a consistent integration path along the LOS for any α, a periodic replication of the basic simulation cube is used in the calculations (e.g., Falceta-Gonçalves et al. (2008),Zhang et al. (2019).

Figure 6.2 - Illustration of a cube rotation around the $y-$ axis to obtain different directions of the mean magnetic field (red arrows) with respect to the same line of sight (black arrows).

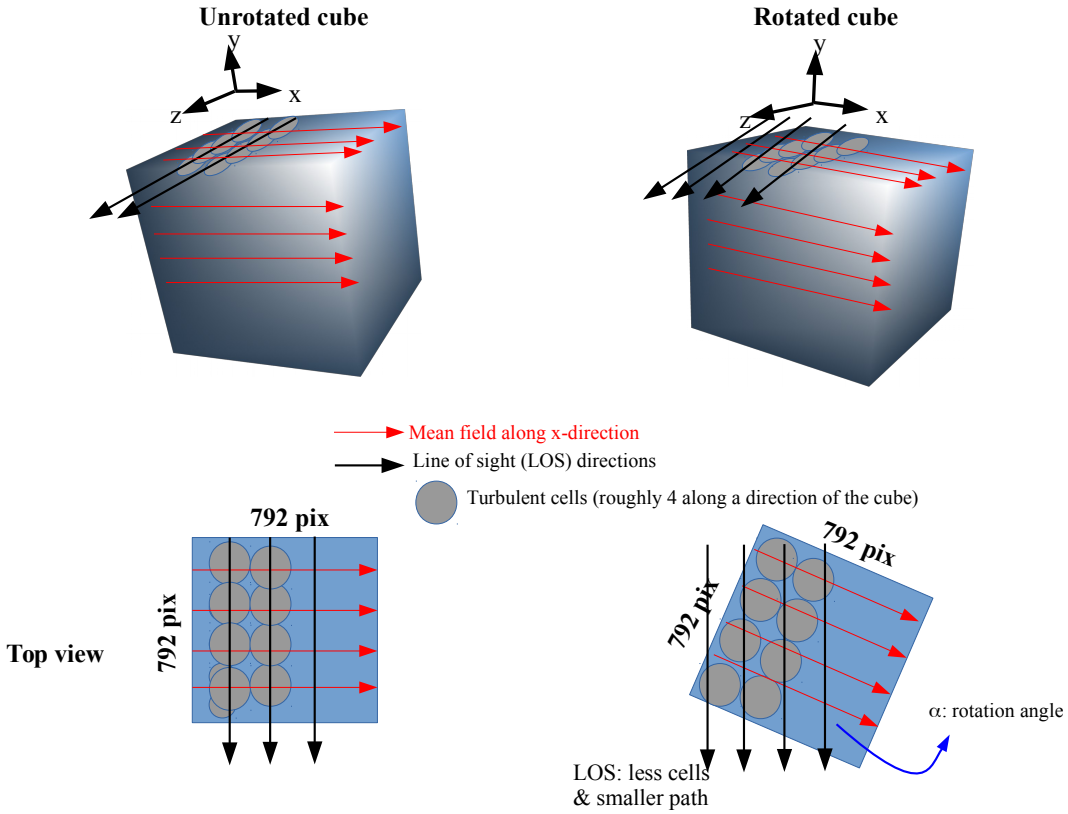

Figure 6.3 shows the relationship between circular standard deviation for different angles α and the Alfvén Mach number for both ∇I and ∇P. Notice that now, we are

considering the combined effects of both constant and random components of the magnetic field, without Faraday rotation. We explore different angle configurations, $\alpha = 80, 70, 50$ and $30°$. Figure 6.3 shows that decreasing angles α show a slight improvement in terms of the associated uncertainties. This behavior is expected since the synchrotron gradients measure the apparent direction of the magnetic field on the plane of the sky. If the plane of the sky component of the mean magnetic field is weak, the turbulent component will become relatively more important, and the gradients are not going to provide the projected direction accurately.

Figure 6.3 - Power-law fits of the circular standard deviation, S, for ∇I (*Top Panel*) and ∇P (*Bottom Panel*) as a function of M_A for different angles α. The trend lines are estimated using a Bayesian approach which allows the estimation of the uncertainties in this case, 1σ. Only the uncertainties for $80°$ (purple) and $30°$ (yellow) cases are presented. The regions $M_A < 1$ (sub-Alfvénic) and $M_A > 1$ (super-Alfvénic) are treated separately. Faraday rotation effects are not considered on this analysis.

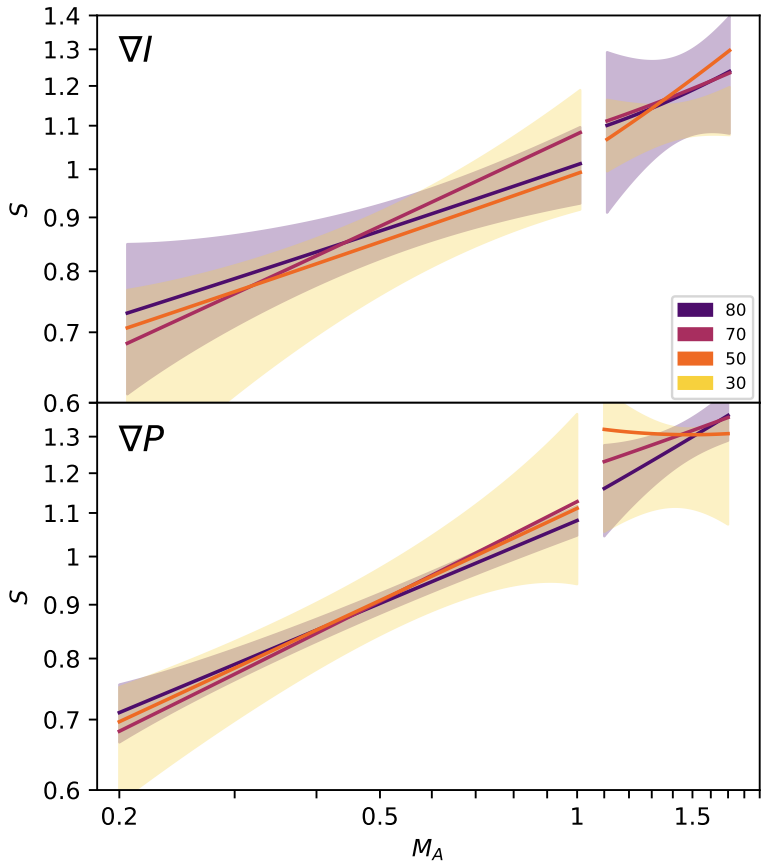

6.3 Faraday rotation effects

Synchrotron emission is susceptible to Faraday rotation effects that have been disregarded so far. Our synthetic polarization maps taking into account Faraday rotation use the same dataset and input physical assumptions used in Zhang et al. (2019). The thermal electron density and magnetic field strength are set to $n_e \sim 0.03\ cm^{-3}$ and $B_{\parallel} \sim 10.3\ \mu G$. As shown in that work, Faraday rotation depends on frequency, as expected, and on the Alfvénic regime of the turbulence. To summarize the relevant statistics in the two different regimes, the rotation measure calculated for $M_A = 0.2$ and $n_e = 0.13\ cm^{-3}$ ranges from -13.0 to 60.3 $rad.m^{-2}$, with a mean value of 7.7±0.1 $rad.m^{-2}$, while for $M_A = 1.0$, it ranges from -2 to 140 $rad.m^{-2}$ and the mean value is 60±1 $rad.m^{-2}$.

A compact way of visualizing the effects of the progressively larger Faraday rotation for lower and lower frequencies is the use of the alignment measure (AM) which describes the correspondence between ∇I, ∇P and the polarization vector quantity (see González-Casanova and Lazarian (2017)). The definition of AM is

$$AM = 2\langle \cos^{\mathbf{2}} \phi \rangle - 1. \tag{6.3}$$

AM is analogous to the Rayleigh reduction factor in the dust alignment theory suggested by Greenberg et al. (1968). ϕ is the angle between the measured magnetic field direction and the intrinsic magnetic field. When $AM = -1$, the magnetic field is perpendicular to ∇P or ∇I. When $AM = 1$, they have a perfect alignment, whereas random orientations result in $AM \sim 0$. Lazarian et al. (2017) showed that AM and ∇I are in the range $0.78 - 0.95$, respectively, at 1 GHz.

AM versus frequency is shown in Figure 6.4, which compares AM with ∇I and ∇P, and polarization vector (green). It can be seen that even though in low frequencies Faraday depolarization effects become stronger and could introduce noise-like substructures in the Stokes Q and U parameters, on small scales, different from what happens with the traditional technique to estimate the magnetic field direction via polarization vector, the statistics of the synchrotron intensity and polarization gradients are still well correlated with the magnetic field, presenting good alignment. It can be concluded that the presence of Faraday rotation does not affect the applicability of the use of ∇P to estimate the magnetic field direction (at least for frequencies $>$ 1 GHz).

Figure 6.4 - AM as a function of frequency for the range $0.1 - 10\,GHz$, from sub- and super-Alfvénic simulations. Small scale noise-like structures in the synthetic synchrotron polarization intensity maps were smoothed with a $\sigma = 2$ pixels Gaussian kernel.

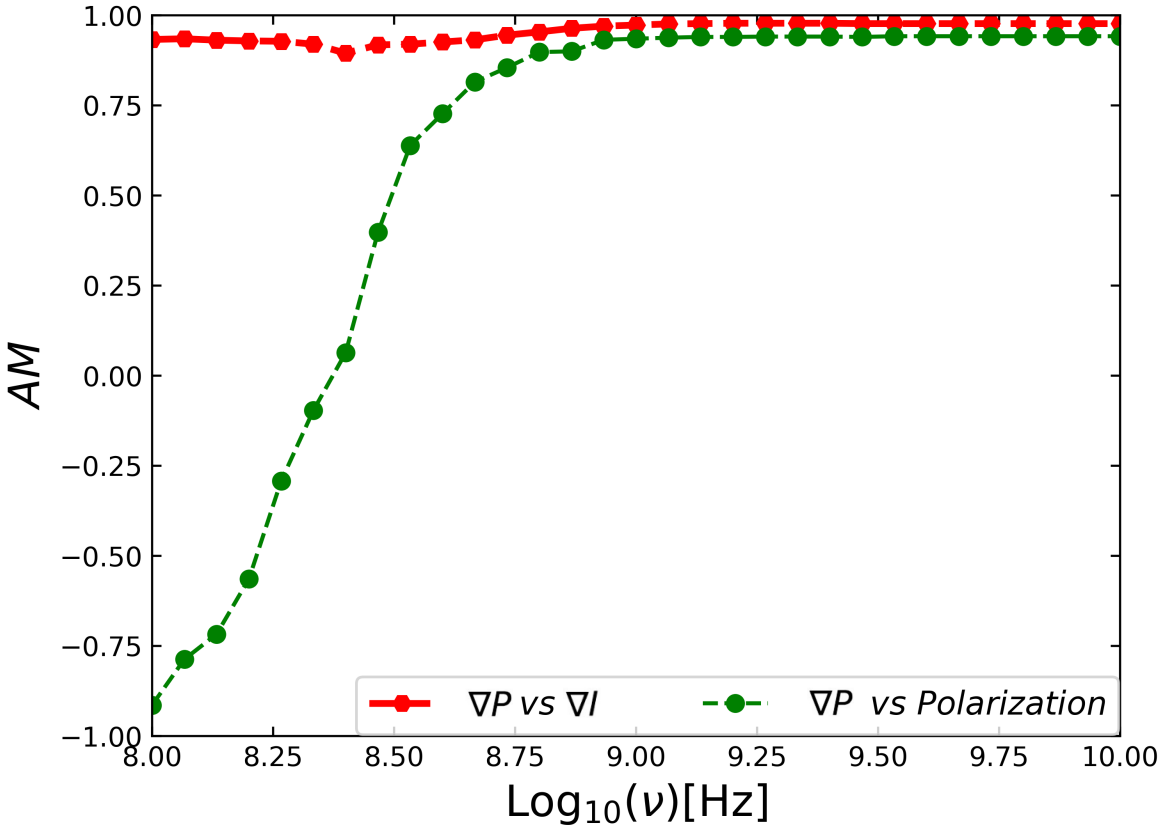

Figure 6.5 shows the relationship between S and the Alfvén Mach number for different frequencies. It is clear that regardless the frequency, ∇I can measure very well the magnetization level, especially in the sub-Alfvénic regime where the correlation is more pronounced. Also, there is no dependence of the result with the mean density of the medium. The reason for this is the fact that the intensity map is insensitive to Faraday rotation, and its consequent depolarization. Also, being an intensity normalized function, S calculated for ∇I is also insensitive to varying n_e.

Figure 6.5 - Power-law fits of the circular standard deviation, S, for SIG (*Top Panel*) and SPG (*Lower Panels*) as a function of M_A. The regions $M_A < 1$ (sub-Alfvénic) and $M_A > 1$ (super-Alfvénic) are treated separately. The different colors correspond to different frequencies to show the effects of Faraday rotation. The trend lines are estimated using a Bayesian approach, that allows realistic uncertainty estimates. In this case, 1σ errors are shown for the 1.4 GHz and 100 GHz frequencies, which are extreme cases. The lower panels show cases for two different electronic densities.

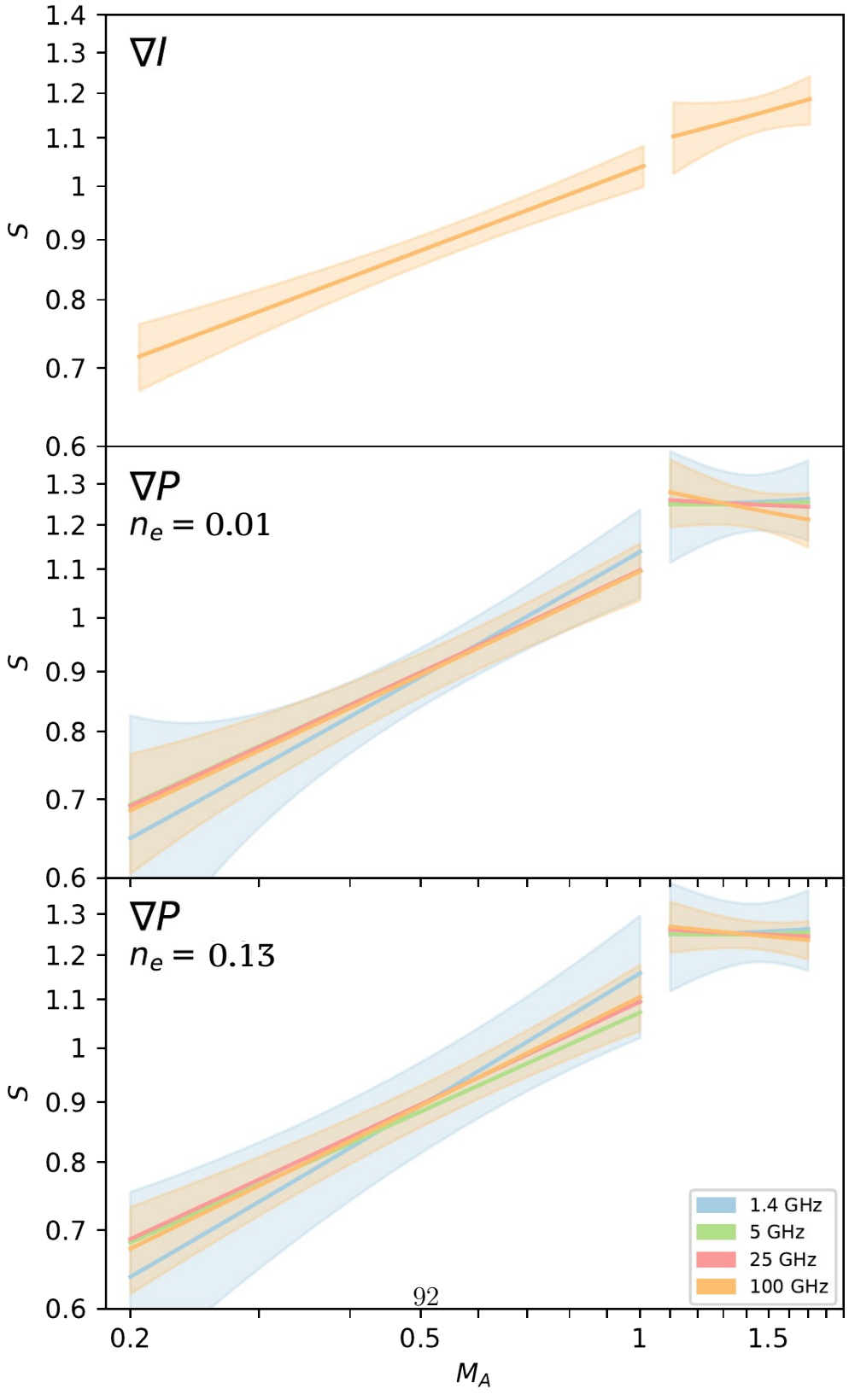

A different situation happens for the polarization maps, and consequently for the ∇P statistics. Synchrotron polarization suffers Faraday depolarization along the line-of-sight, and depends on the observational wavelength and the density of the medium. For this reason, to check these effects, we have calculated the S parameter of ∇P for two different values of density, namely $n_e = 0.01$ and 0.13 cm^{-3}, and frequencies between 1.4 to 100 GHz. We found that in the sub-Alfvénic regime, lower frequencies tend to show a larger correlation between S and $M_{\rm A}$. However, as can be seen in Figure 6.5, all lines shown lie within the 1σ uncertainty region from each other, with no significant change in slope in a range of ~ 2 orders of magnitude in frequency. A factor of 3 in mean density also does not result in significant change in the slope or the absolute value of S[1]. For the super-Alfvénic regime, it is still possible to use a linear trend to model the magnetization level with ∇I but the power-law description breaks up for the ∇P case. Given these uncertainties, only upper limits to the magnetic field strength would be obtained from ∇P in the super-Alfvénic regime.

Overall, it is evident that the ∇I and ∇P angle distributions can measure the magnetization level, considering the range of parameters probed in this work. Future work may explore and extend this analysis to even higher magnetic field values and consequently higher values of Faraday rotation effects, in order to check its validity for other regimes.

6.4 Telescope resolution

Another important observational aspect that must be studied is the finite telescope resolution, which can introduce additional uncertainties to the techniques explored here. In order to account for data averaging within the telescope beam, we use a Gaussian smoothing kernels on the maps. Four different values for the full-width-at-half-maximum (FWHM) of the smoothing kernel (2, 4, 8 and 16 pixels) were examined to estimate the effects of progressively degraded resolution with respect to the original data.

The relationships presented in 6.1 and 6.2 for ∇I and ∇P, respectively, are the reference for the comparison. The same procedure to obtain the dependency between parameters was applied, now considering different values of smoothing. We found that the Top-Base method is limited for FWHM < 8. For larger values, this technique

[1]Notice that we plot S versus $M_{\rm A}$, which is dependent on $n^{1/2}$. Therefore, for the same S value, the magnetic field intensity estimated from the bottom-panel of Figure 6.5 will be $\sqrt{3}$ larger than its value obtained from the mid-panel.

does not present a good linear correlation with M_A. However, both circular variance and standard deviation methods present good linear correlations even for the largest value of FWHM considered in the beam smoothing experiments. Table 6.1 presents the best fit power-laws for different values of FWHM. As can be seen, for all the cases considered there is no significant degradation with respect to the nominal values.

Table 6.1 - Power-Law relationships to obtain M_A for circular variance statistics, considering different values of smoothing. The linear fitting used to obtain the expressions bellow considers a Bayesian approach to estimate the parameters and uncertainties.

FWHM		∇I	∇P
2	Sub-Alfvénic	$0.84^{+0.12}_{-0.10}\ S_I^{3.6^{+0.3}_{-0.4}}$,	$0.85^{+0.09}_{-0.11}\ S_P^{4.2^{+0.8}_{-0.8}}$
	Super-Alfvénic	$0.93^{+0.11}_{-0.05}\ S_I^{3.8^{+0.7}_{-0.6}}$	$0.85^{+0.07}_{-0.05}\ S_P^{3.2^{+0.4}_{-0.7}}$
4	Sub-Alfvénic	$0.84^{+0.12}_{-0.12}\ S_I^{3.6^{+0.3}_{-0.5}}$,	$0.85^{+0.09}_{-0.12}\ S_P^{4.2^{+0.9}_{-0.8}}$
	Super-Alfvénic	$0.93^{+0.12}_{-0.06}\ S_I^{3.8^{+0.8}_{-0.7}}$	$0.85^{+0.07}_{-0.06}\ S_P^{3.2^{+0.6}_{-0.7}}$
8	Sub-Alfvénic	$0.83^{+0.14}_{-0.15}\ S_I^{3.7^{+0.4}_{-0.6}}$,	$0.83^{+0.09}_{-0.12}\ S_P^{4.4^{+1.0}_{-0.9}}$
	Super-Alfvénic	$0.94^{+0.12}_{-0.06}\ S_I^{3.9^{+0.8}_{-0.7}}$	$0.85^{+0.08}_{-0.09}\ S_P^{3.4^{+0.8}_{-0.7}}$
16	Sub-Alfvénic	$0.83^{+0.14}_{-0.15}\ S_I^{3.7^{+0.5}_{-0.8}}$,	$0.83^{+0.11}_{-0.13}\ S_P^{4.4^{+1.1}_{-0.9}}$
	Super-Alfvénic	$0.95^{+0.21}_{-0.11}\ S_I^{3.9^{+0.9}_{-0.9}}$	$0.86^{+0.11}_{-0.12}\ S_P^{3.4^{+1.1}_{-1.0}}$

7 DISCUSSION, CONCLUSIONS AND PERSPECTIVES

In this thesis, we have investigated ways to obtain information about the magnetization level in different magneto-ionic regions. In an effort to achieve this, large numerical simulations using magnetohydrodynamic equations were performed. This chapter summarizes the main results obtained in our work, presenting also a discussion regarding the use of synchrotron gradient orientations for obtaining M_A. Finally, a discussion on current and future work expected to be done upon the finding of this thesis is presented.

7.1 Summary

Recent developments in the study of synchrotron gradients show that these quantities provide a reliable way to trace the magnetic field direction in turbulent plasmas. A synergistic analysis combining MHD simulations, statistical analysis and observational data provides a potential way to characterize the interstellar turbulence and magnetic field distributions. The works of Zhang et al. (2019), Zhang et al. (2019), Hu et al. (2019a) and Hu et al. (2019b) used such combination to study polarization and velocity gradients (from emission lines) aiming to explore the different properties of the ISM. We have analyzed possible correlations of angle distributions and other parameters that are essential to describe astrophysical turbulence and the associate distributions. In order to pinpoint M_A, in this thesis, we addressed the following key points:

- Regarding the effects of S/N ratio in the results, in Section 6.1 we showed that for values $\mathrm{S/N} < 10$, the Top-Base method presents limitations. Fortunately, the circular standard deviation method is still well correlated with M_A, even for lower values of the S/N ratio. Since meaningful measurements of synchrotron emission at radio wavelengths have a threshold around $\mathrm{S/N} = 5$, the application of the standard deviation method is viable even at this limit. In order to have a fair assessment of the accuracy of the results, we used a Bayesian approach, together with a MCMC sampling scheme for investigating the relationships among M_A and the relevant indicators in Section 5.3.

- We also addressed the effects of the orientation of the mean magnetic field with respect to the LOS, and checked whether it can limit the applicability of the technique. As shown in Section 6.2, the statistics of the gradients, as a proxy to estimate M_A, is preserved for a broad range of angles.

- Following Zhang et al. (2019) who tested the effect of the alignment of the synchrotron gradients with the local magnetic field when the emission is subject to Faraday depolarization, in our work, we also considered the influence of weak Faraday depolarization regimes in order to test if the techniques explored here can still be applied to estimate the magnetization level. For both low and high frequencies, the ∇P angles are weakly affected by Faraday rotation. The results also indicate that the use of gradients is valid for regimes where the conventional polarization vector approach does not behave well.

Our work opens venues to the study of the magnetization level via the synchrotron emission in our Galaxy and beyond. Combining measurements of ∇P with ∇I provides several ways to obtain synergy from the two measurements and increases the reliability of the results. Since ∇I are not subjected to Faraday rotation, they do not require multiple frequency measurements to compensate for the effect.

7.2 Combined use of gradients in turbulence

The discovery of unknown properties of gradients provides another way of using the associated information to study properties of the magnetized interstellar medium. Other gradient studies showed the correlation between velocity gradient orientations with the sonic Mach number, via studying the amplitudes of these quantities. The combined study using both velocity and synchrotron gradients can provide both M_A, M_S, as well as the magnetic field direction. Recovering these parameters from astrophysical observations is important to characterize the different properties of several astrophysical processes, such as: star formation, cosmic ray acceleration, and cosmological foreground subtraction. As explained before, both M_A and M_S are extremely complex to retrieve from observations. The statistical tools presented in this work and in Yuen and Lazarian (2017) can be applied to observations, and this is a promising next step starting from our work.

7.3 Synchrotron gradients directions to obtain 3D magnetization level

As presented by Lazarian and Yuen (2018), synchrotron polarization gradients can also be used to probe turbulence and the distribution of magnetic field directions in a 3D view. Using the properties of this quantity to measure the local magnetic field direction and its dependency with frequency, the angle orientation in 3D can be obtained. Using the angle distribution from this technique, M_A can be obtained in a volume. Figure 7.1 shows the 3D magnetic field vector constructed for the data cube

with $M_A = 0.61$ at $\nu = 1.01$ GHz using the same technique presented by Lazarian and Yuen (2018). As can be seen, the 3D directions from the gradients are close to what is obtained from the magnetic field vector in the original data.

Figure 7.1 - The three-dimensional magnetic field morphology plotted in blue with the 3D reconstructed gradients in red, using the same recipe presented by Lazarian and Yuen (2018). The data cube refers to a simulation with $M_A = 0.61$. The sudden jumps in some particular locations are better treated in Hu and Lazarian (2022).

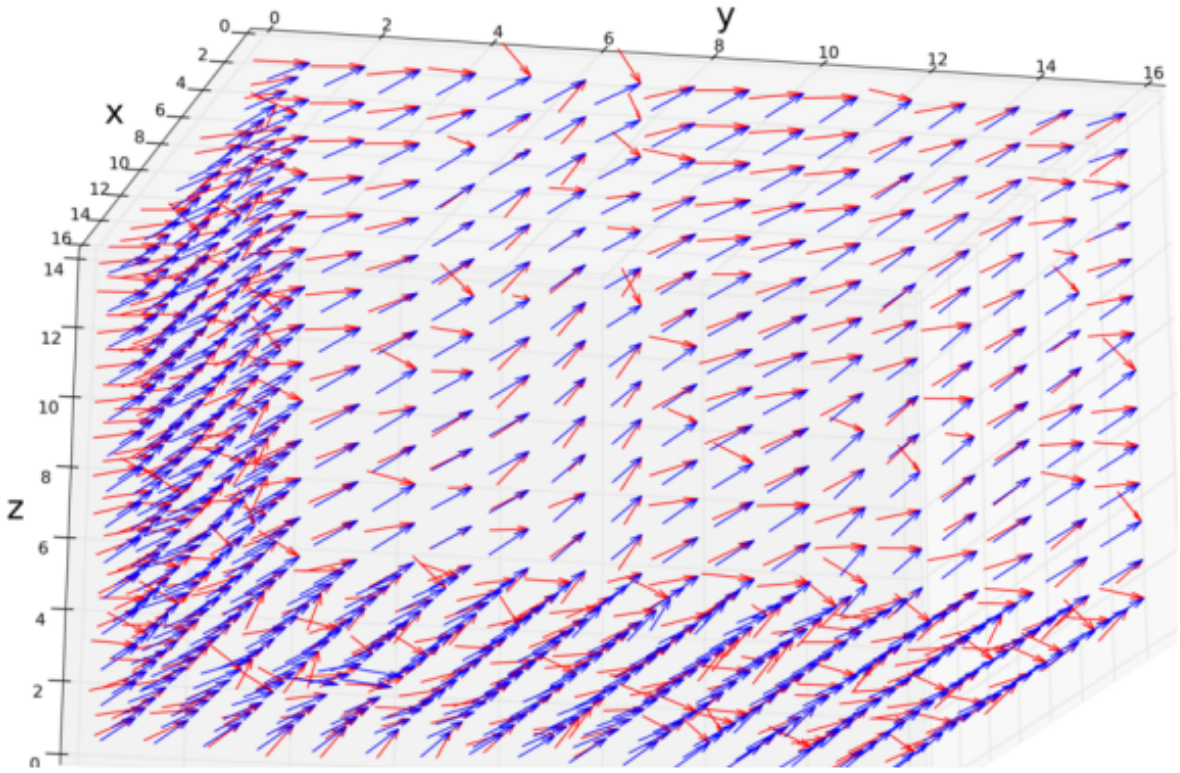

The correlation between the polarization gradients angles was obtained along different projections, therefore, the 3D angles distributions can be obtained. A paper regarding the morphology of the M_A has been prepared, together with other group members that have been applying for the first time the gradients technique to obtain information of 3D magnetic field in observations.

7.4 Synchrotron gradients angles distribution correlation with M_A in simulations with self-gravity

Simulations with M_A= 0.1 and M_A = 1.3, including self-gravity, with resolution of 512^3 cells were also investigated in this work, but with limited scope. The self-gravity could distort the alignment of gradients and influence estimates of M_A. Self-gravity is expected to modify the properties of the flow. The change in the properties of MHD turbulence within such regions is expected to produce changes on the gradients properties, in particular their alignment with the magnetic field. For sub-alfvénic cases, the alignment is still preserved. For super-alfvénic case, we found that the relevant correlations are lost for intensity and polarization synchrotron gradients direction. This is expected because for large M_A, the turbulent motions are not affected by magnetic cascades that drive the correlation between both quantities. This can also be seen on our previous results for M_A and, therefore, the technique is not efficient in regions where self-gravity is intense.

7.5 Use of gradients in astronomical observations

The techniques obtained on this thesis are important because they can be applied in multi-frequency regimes, under the influence of weak and strong Faraday depolarization. Therefore, both intensity and polarization synchrotron gradients angles distributions can be applicable on high resolution ISM data collected by the next generation of radio-telescopes, as the Low Frequency Array (LOFAR), the Australian Square Kilometre Array Pathfinder (ASKAP), and the Square Kilometre Array (SKA). This would be complemented by the higher frequencies coverage and smaller field-of-view instruments like the Atacama Large Millimeter Array (ALMA) and the Very Large Array (VLA), meaning that the combination of these resources can provide the magnetization levels for small and large scales of the ISM.

7.6 Future work

The main results presented in this thesis were published on the Astrophysical Journal by Carmo et al. (2020), entitled "*Synchrotron Intensity and Polarization Gradients: Tools to Obtain the Magnetization Level in a Turbulent Medium*". Another paper focused on the use of gradients to obtain the magnetization levels compared to LOFAR high resolution data of the diffuse interstellar medium is being finalized.

The current work has neglected so far the influence of synchrotron self-absorption and variations in the distribution of relativistic electrons on the polarization maps.

In general, Faraday rotation takes effect in relatively low frequency bands, exactly at same ranges where synchrotron self-absorption effect should is important for the astrophysical environments we are interested in. The influence of both effects is being analyzed and should be presented in the near future.

REFERENCES

ALFVÉN, H. Existence of electromagnetic-hydrodynamic waves. **Nature**, v. 150, p. 405–406, out. 1942. 30

ALVES, M.; FERRIERE, K. The interstellar magnetic field from galactic scales down to the heliosphere. In: EUROPEAN SPACE AGENCY, 42., 2018, Pasadena, United States. **42nd cospar scientific assembly**. Pasadena: ICI/IFSA, 2018. p. D1.2–2–18. 30

ANDERSSON, B.-G. Interstellar grain alignment - observational status. **ArXiv e-prints**, ago. 2012. 31, 32

ARMSTRONG, J. W.; RICKETT, B. J.; SPANGLER, S. R. Electron density power spectrum in the local interstellar medium. **The Astrophysical Journal**, v. 443, p. 209–221, abr. 1995. 12

BABCOCK, H. W. The Sun's magnetic field. **Annual Review**, v. 1, p. 41, jan. 1963. 29

BAMERT, K.; KALLENBACH, R.; ROUX, J. L.; HILCHENBACH, M.; SMITH, C.; WURZ, P. Evidence for iroshnikov-kraichnan-type turbulence in the solar wind upstream of interplanetary traveling shocks. **The Astrophysical Journal Letters**, v. 675, n. 1, p. L45, 2008. 24

BATSCHELET, E. **Circular statistics in biology**. 7. ed. New York: Academic press, 1981. 388 p. ISBN 23-85-546546-33-7. 82

BEATTIE, J. R.; FEDERRATH, C.; SETA, A. Magnetic field fluctuations in anisotropic, supersonic turbulence. **Monthly Notices of the Royal Astronomical Society**, v. 498, n. 2, p. 1593–1608, out. 2020. 43

BEATTIE, J. R.; KRUMHOLZ, M. R.; SKALIDIS, R.; FEDERRATH, C.; SETA, A.; CROCKER, R. M.; MOCZ, P.; KRIEL, N. Energy balance and Alfvén Mach numbers in compressible magnetohydrodynamic turbulence with a large-scale magnetic field. **arXiv e-prints**, fev. 2022. 68

BECK, R. Observations of magnetic fields in galaxies. In: DE GOUVEIA DAL PINO, E. M; LUGONES, G.; LAZARIAN, A. (ED.) UNIVERSIDADE DE SÃO PAULO, 1., 2012, Angra dos Reis, Brazil. **Magnetic fields in the universe: from laboratory and stars to primordial Structures.** Angra dos Reis: Springer, 2005. p. 343–353. 39

_____. Galactic and extragalactic magnetic fields. In: DE GOUVEIA DAL PINO, E. M; LUGONES, G.; LAZARIAN, A. (ED.) UNIVERSIDADE DE SÃO PAULO, 1085., 2012, Angra dos Reis, Brazil. **The astrophysics of galactic cosmic rays**. Angra dos Reis: Springer, 2008. p. 83–96. 50

_____. Measuring interstellar magnetic fields by radio synchrotron emission. In: STRASSMEIER, K. G.; KOSOVICHEV, A. G.; BECKMAN, J. E. (Ed.). **Cosmic magnetic fields: from planets, to stars and galaxies**. [S.l.: s.n.], 2009. v. 259, p. 3–14. 39

_____. Magnetic fields in spiral galaxies. **Astronomy and Astrophysics Reviews**, v. 24, p. 4, dez. 2015. 30, 39

BEL, N.; LEROY, B. Zeeman splitting in interstellar molecules. **Astronomy & Astrophysics**, v. 224, p. 206–208, out. 1989. 3

BELLAN, P. M. **Fundamentals of plasma physics**. [S.l.: s.n.], 2006. 7

BENZ, A. **Plasma astrophysics**. [S.l.: s.n.], 2002. 7

BERESNYAK, A. Spectral slope and kolmogorov constant of MHD Turbulence. **Physical Review Letters**, v. 106, n. 7, p. 075001, fev. 2011. 25

BERESNYAK, A.; LAZARIAN, A. Scaling laws and diffuse locality of balanced and imbalanced Magnetohydrodynamic Turbulence. **The Astrophysical Journal Letters**, v. 722, n. 1, p. L110–L113, out. 2010. 25

_____. **Turbulence in magnetohydrodynamics**. [S.l.: s.n.], 2019. 7, 43, 46

BEREZHKO, E.; VÖLK, H. The theory of synchrotron emission from supernova remnants. **Astronomy & Astrophysics**, v. 427, n. 2, p. 525–536, 2004. 39

BIERMANN, P. L.; STRITTMATTER, P. A. Synchrotron emission from shock waves in active galactic nuclei. **The Astrophysical Journal**, v. 322, p. 643, nov. 1987. 39

BIGOT, B.; GALTIER, S.; POLITANO, H. Development of anisotropy in incompressible magnetohydrodynamic turbulence. **Physical Review E**, v. 78, n. 6, p. 066301, 2008. 22

BISKAMP, D. **Magnetohydrodynamic turbulence**. [S.l.]: Cambridge University Press, 2003. 22

BODENHEIMER, P. **Numerical methods in astrophysics: an introduction**. [S.l.]: CRC Press, 2006. 60

BOLATTO, A. D.; LEROY, A. K.; ROSOLOWSKY, E.; WALTER, F.; BLITZ, L. The resolved properties of extragalactic giant molecular clouds. In: HUNT, L. K.; MADDEN, S. C.; SCHNEIDER, R. (Ed.). **Low-metallicity star formation: from the first stars to dwarf galaxies**. [S.l.: s.n.], 2008. v. 255, p. 274–277. 44

BOYD, T. J. M.; SANDERSO, J. J. **The physics of plasmas**. [S.l.: s.n.], 2003. 544 p. 15

BRANDENBURG, A.; LAZARIAN, A. Astrophysical hydromagnetic turbulence. **Space Science Reviews**, v. 178, p. 163–200, out. 2013. 22

BRANDENBURG, A.; NORDLUND, A. Astrophysical turbulence modeling. **Reports on Progress in Physics**, v. 74, n. 4, p. 046901, abr. 2011. 22

BRUNO, R.; CARBONE, V. The solar wind as a turbulence laboratory. **Living Reviews in Solar Physics**, v. 10, n. 1, p. 2, maio 2013. 12

BURKHART, B. Diagnosing turbulence in the neutral and molecular interstellar medium of galaxies. **arXiv e-prints**, p. arXiv:2106.02239, jun. 2021. 43, 46

BURKHART, B.; FALCETA-GONÇALVES, D.; KOWAL, G.; LAZARIAN, A. Density studies of MHD interstellar turbulence: statistical moments, correlations and bispectrum. **The Astrophysical Journal**, v. 693, n. 1, p. 250–266, mar. 2009. 3, 44, 69

BURKHART, B.; LAZARIAN, A. Statistical tools of interstellar turbulence: bridging the gap between numerics and observations. In: INTERNTAIONAL CONFERENCE OF NUMERICAL MODELING OF SPACE PLASMA FLOWS, 5., 2011, Alabama , United States. **5th International Conference of Numerical Modeling of Space Plasma Flows**. Alabama: Astronomical Society of the pacific Conference Series, 2011. p. 516–523. 3, 5, 44, 49

_____. The column density variance-{M}_s relationship. **The Astrophysical Journal**, v. 755, p. L19, Aug 2012. 3, 4, 47, 49, 51, 53

CARMO, L.; GONZÁLEZ-CASANOVA, D. F.; FALCETA-GONÇALVES, D.; LAZARIAN, A.; JABLONSKI, F.; ZHANG, J.-F.; FERREIRA, I.; CASTRO, M.; YANG, B. Synchrotron intensity and polarization gradients: tools to obtain the magnetization level in a turbulent medium. **The Astrophysical Journal**, v. 905, n. 2, p. 130, 2020. 71, 85, 98

CHANDRASEKHAR, S.; FERMI, E. Magnetic fields in spiral arms. **Astrophysical Journal**, v. 118, p. 113, jul. 1953. 34

CHEPURNOV, A.; GORDON, J.; LAZARIAN, A.; STANIMIROVIC, S. Topology of neutral hydrogen within the small magellanic cloud. **The Astrophysical Journal**, v. 688, p. 1021–1028, Dec 2008. 3, 49

CHO, J.; LAZARIAN, A. Compressible sub-Alfvénic MHD turbulence in low- β plasmas. **Physical Review Letters**, v. 88, n. 24, p. 245001, jun. 2002. 25, 67

_____. Galactic foregrounds: spatial fluctuations and a procedure for removal. **The Astrophysical Journal**, v. 720, n. 2, p. 1181–1201, Sep 2010. 69

CHO, J.; LAZARIAN, A.; VISHNIAC, E. T. MHD turbulence: scaling laws and astrophysical implications. In: _____. **Turbulence and magnetic fields in astrophysics**. [S.l.: s.n.], 2003. v. 614, p. 56–98. 26, 43, 46

CHO, J.; VISHNIAC, E. T. The anisotropy of magnetohydrodynamic alfvénic turbulence. **The Astrophysical Journal**, v. 539, p. 273–282, ago. 2000. 25

CHORIN, A. J. Lectures on turbulence theory. **NASA STI/Recon Technical Report**, v. 76, p. 15548, jan. 1975. 10

CHURCHWELL, E. Ultra-compact hii regions and massive star formation. **Annual Review of Astronomy and Astrophysics**, v. 40, n. 1, p. 27–62, 2002. 29

CLARK, B. G. An interferometer investigation of the 21-centimeter hydrogen-line Absorption. **Astrophysical Journal**, v. 142, p. 1398, nov. 1965. 28

CLAUSEN-BROWN, E.; LYUTIKOV, M.; KHARB, P. Signatures of large-scale magnetic fields in active galactic nuclei jets: transverse asymmetries. **Monthly Notices of the Royal Astronomical Society**, v. 415, n. 3, p. 2081–2092, ago. 2011. 39

CORDES, J. M.; LAZIO, T. J. W. NE2001. II. Using radio propagation data to construct a model for the galactic distribution of free electrons. **arXiv e-prints**, p. astro–ph/0301598, jan. 2003. 70

CORREIA, C.; LAZARIAN, A.; BURKHART, B.; POGOSYAN, D.; MEDEIROS, J. R. D. Principal component analysis studies of turbulence in optically thick gas. **The Astrophysical Journal**, v. 818, p. 118, Feb 2016. 3, 49

CRUTCHER, R. Interstellar magnetic fields. In: _____. **Encyclopedia of astronomy and astrophysics**. [S.l.: s.n.], 2000. p. 2777. 29

CRUTCHER, R. M. Magnetic fields in molecular clouds. **Annual Review of Astronomy and Astrophysics**, v. 50, p. 29–63, 2012. 29, 30, 35, 38

CRUTCHER, R. M.; KAZES, I.; TROLAND, T. H. Magnetic field strengths in molecular clouds. **Astronomy and Astrophysics**, v. 181, p. 119–126, jul. 1987. 12

CRUTCHER, R. M.; TROLAND, T. H.; GOODMAN, A. A.; HEILES, C.; KAZES, I.; MYERS, P. C. OH Zeeman observations of dark clouds. **Astrophysical Journal**, v. 407, p. 175–184, abr. 1993. 30, 37

CRUTCHER, R. M.; TROLAND, T. H.; LAZAREFF, B.; KAZES, I. Cn zeeman observations of molecular cloud cores. **The Astrophysical Journal**, v. 456, p. 217, 1996. 3, 38

CRUTCHER, R. M.; TROLAND, T. H.; LAZAREFF, B.; PAUBERT, G.; KAZÈS, I. Detection of the cn zeeman effect in molecular clouds. **The Astrophysical Journal Letters**, v. 514, n. 2, p. L121, 1999. 38

DAVIDSON, P. A. **Turbulence : an introduction for scientists and engineers**. [S.l.: s.n.], 2004. 11

DOBROWOLNY, M.; MANGENEY, A.; VELTRI, P. Fully developed anisotropic hydromagnetic turbulence in interplanetary space. **Physical Review Letters**, v. 45, n. 2, p. 144, 1980. 24

DOLGINOV, A. Z.; MITROFANOV, I. G. Orientation of cosmic dust grains. **Astrophysics and Space Science**, v. 43, p. 291–317, set. 1976. 32

DRAINE, B. T. **Physics of the Interstellar and Intergalactic Medium**. [S.l.: s.n.], 2011. 27, 30

DYSON, J. E.; WILLIAMS, D. A. **The physics of the interstellar medium**. [S.l.]: CRC Press, 2020. 27

ECK, C. L. V.; BROWN, J. C.; STIL, J. M.; RAE, K.; MAO, S. A.; GAENSLER, B. M.; SHUKUROV, A.; TAYLOR, A. R.; HAVERKORN, M.; KRONBERG, P. P.; MCCLURE-GRIFFITHS, N. M. Modeling the magnetic field in the Galactic disk using new rotation measure observations from the very large array. **The Astrophysical Journal**, v. 728, n. 2, p. 97, Feb 2011. 3

ELMEGREEN, B. G.; SCALO, J. Interstellar turbulence I: observations and processes. **Annual Review of Astronomy and Astrophysics**, v. 42, p. 211–273, set. 2004. 1, 43

ELSASSER, W. M. The hydromagnetic equations. **Physical Review**, v. 79, p. 183–183, jul. 1950. 21, 24

ENSOR, T.; CAMI, J.; BHATT, N. H.; SODDU, A. A principal component analysis of the diffuse interstellar bands. **The Astrophysical Journal**, v. 836, p. 162, Feb 2017. 3, 49

EVANS, C. R.; HAWLEY, J. F. Simulation of magnetohydrodynamic flows-a constrained transport method. **The Astrophysical Journal**, v. 332, p. 659–677, 1988. 64

FAISON, M.; GOSS, W. The structure of the cold neutral ism on 10-100 astronomical unit scales. **arXiv preprint astro-ph/0011460**, 2000. 28

FALCETA-GONÇALVES, D. Interstellar Turbulence. In: **Revista Mexicana de Astronomia y Astrofisica Conference Series**. [S.l.: s.n.], 2011. (Revista Mexicana de Astronomia y Astrofisica Conference Series, v. 40). 12, 13

FALCETA-GONÇALVES, D.; CAPRONI, A.; ABRAHAM, Z.; TEIXEIRA, D.; PINO, E. d. G. D. Precessing jets and x-ray bubbles from ngc 1275 (3c 84) in the perseus galaxy cluster: a view from three-dimensional numerical simulations. **The Astrophysical Journal Letters**, v. 713, n. 1, p. L74, 2010. 57

FALCETA-GONÇALVES, D.; KOWAL, G.; FALGARONE, E.; CHIAN, A. C.-L. Turbulence in the interstellar medium. **Nonlinear Processes in Geophysics**, v. 21, p. 587–604, maio 2014. 12, 30, 43, 47

FALCETA-GONÇALVES, D.; LAZARIAN, A.; KOWAL, G. Studies of regular and random magnetic fields in the ism: statistics of polarization vectors and the chandrasekhar-Fermi technique. **The Astrophysical Journal**, v. 679, p. 537–551, maio 2008. xii, 47, 69, 88

FALCETA-GONÇALVES, D.; PINO, E. d. G. D.; GALLAGHER, J.; LAZARIAN, A. Turbulence and the formation of filaments, loops, and shock fronts in ngc 1275. **The Astrophysical Journal Letters**, v. 708, n. 1, p. L57, 2009. 35, 57

FALGARONE, E.; PETY, J.; HILY-BLANT, P. Intermittency of interstellar turbulence: extreme velocity-shears and CO emission on milliparsec scale. **Astronomy and Astrophysics**, v. 507, n. 1, p. 355–368, nov. 2009. 44

FALGARONE, E.; PHILLIPS, T. A signature of the intermittency of interstellar turbulence-the wings of molecular line profiles. **The Astrophysical Journal**, v. 359, p. 344–354, 1990. 30

FALGARONE, E.; TROLAND, T.; CRUTCHER, R.; PAUBERT, G. Cn zeeman measurements in star formation regions. **Astronomy & Astrophysics**, v. 487, n. 1, p. 247–252, 2008. 38

FEDERRATH, C.; KLESSEN, R. S.; SCHMIDT, W. The density probability distribution in compressible isothermal turbulence: solenoidal versus compressive forcing. **The Astrophysical Journal**, v. 688, p. L79, Dec 2008. 3, 49

FERRIÈRE, K. The origin of galactic magnetic fields and their impact on the interstellar medium. In: CHYZY, K. T.; OTMIANOWSKA-MAZUR, K.; SOIDA, M.; DETTMAR, R.-J. (Ed.). **The magnetized plasma in galaxy evolution**. [S.l.: s.n.], 2005. p. 147–155. 30

FERRIÈRE, K.; WEST, J. L.; JAFFE, T. R. The correct sense of faraday rotation. **arXiv e-prints**, p. arXiv:2106.03074, jun. 2021. 42

FIELD, G. B. Thermal instability. **The Astrophysical Journal**, v. 142, p. 531, ago. 1965. 27

FIELD, G. B.; GOLDSMITH, D. W.; HABING, H. J. Cosmic-ray heating of the interstellar gas. **The Astrophysical Journal Letter**, v. 155, p. L149, mar. 1969. 28

FINLAY, C. C.; MAUS, S.; BEGGAN, C. D.; BONDAR, T. N.; CHAMBODUT, A.; CHERNOVA, T. A.; CHULLIAT, A.; GOLOVKOV, V. P.; HAMILTON, B.; HAMOUDI, M.; HOLME, R.; HULOT, G.; KUANG, W.; LANGLAIS, B.; LESUR, V.; LOWES, F. J.; LÜHR, H.; MACMILLAN, S.; MANDEA, M.; MCLEAN, S.; MANOJ, C.; MENVIELLE, M.; MICHAELIS, I.; OLSEN, N.; RAUBERG, J.; ROTHER, M.; SABAKA, T. J.; TANGBORN, A.; TØFFNER-CLAUSEN, L.; THÉBAULT, E.; THOMSON, A. W. P.; WARDINSKI, I.; WEI, Z.; ZVEREVA, T. I. International geomagnetic reference field: the eleventh generation. **Geophysical Journal International**, v. 183, n. 3, p. 1216–1230, dez. 2010. 29

FISHER, N. I. **Statistical analysis of circular data**. [S.l.]: Cambridge University Press, 1995. 82

FLETCHER, A.; SHUKUROV, A. Canals in Milky Way radio polarization maps. **Monthly Notices of the Royal Astronomical Society: Letters**, v. 371, n. 1, p. L21–L25, set. 2006. 50

FRISCH, P. C. **Interstellar gas in our galaxy**. [S.l.: s.n.], 2001. 29

FRISCH, U. **Turbulence. the legacy of A.N. Kolmogorov**. [S.l.: s.n.], 1995. 10, 11, 12, 48

FURLANETTO, S. R.; LOEB, A. Intergalactic magnetic fields from quasar outflows. **The Astrophysical Journal**, v. 556, n. 2, p. 619–634, ago. 2001. 29

GAENSLER, B. M.; HAVERKORN, M.; BURKHART, B.; NEWTON-MCGEE, K. J.; EKERS, R. D.; LAZARIAN, A.; MCCLURE-GRIFFITHS, N. M.; ROBISHAW, T.; DICKEY, J. M.; GREEN, A. J. Low-Mach-number turbulence in interstellar gas revealed by radio polarization gradients. **Nature**, v. 478, p. 214–217, out. 2011. 4, 48, 50, 51, 52, 53

GALTIER, S. Wave turbulence in magnetohydrodynamics. **ArXiv e-prints**, jan. 2012. 22

_____. **Introduction to modern magnetohydrodynamics**. [S.l.: s.n.], 2016. 22

GARDNER, F. F.; WHITEOAK, J. B. The polarization of cosmic radio waves. **Annual Review of Astronomy and Astrophysics**, v. 4, p. 245, jan. 1966. 41

GHOSH, S.; MATTHAEUS, W. H. Relaxation processes in a turbulent compressible magnetofluid. **Physics of Fluids B**, v. 2, n. 7, p. 1520–1534, jul. 1990. 12

GINZBURG, V. L.; SYROVATSKII, S. I. Cosmic magnetobremsstrahlung (synchrotron Radiation). **Annual Review of Astron and Astrophys**, v. 3, p. 297, 1965. 39

GIRART, J. M.; RAO, R.; MARRONE, D. P. Magnetic fields in the formation of sun-like stars. **Science**, v. 313, n. 5788, p. 812–814, ago. 2006. 3

GLOVER, S. C. O.; CLARK, P. C. Is molecular gas necessary for star formation? **Monthly Notices of the Royal Astronomical Society**, v. 421, p. 9–19, mar. 2012. 28

GOLDREICH, P.; SRIDHAR, S. Toward a theory of interstellar turbulence. 2: strong alfvenic turbulence. **The Astrophysical Journal**, v. 438, p. 763–775, jan. 1995. 25, 53, 54, 55

GONZÁLEZ-CASANOVA, D. F.; LAZARIAN, A. Velocity gradients as a tracer for magnetic fields. **The Astrophysical Journal**, v. 835, p. 41, jan. 2017. 4, 30, 53, 54, 55, 90

_____. Mapping of the structure of the galactic magnetic field with velocity gradients: test using star light polarization. **The Astrophysical Journal**, v. 874, n. 1, p. 25, Mar 2019. 4

GONZÁLEZ-CASANOVA, D. F.; LAZARIAN, A.; BURKHART, B. Velocity centroid gradients for absorbing media. **Monthly Notices of the Royal Astronomical Society**, v. 483, n. 1, p. 1287–1294, 2019. 4

GONZÁLEZ-CASANOVA, D. F.; LAZEARIAN, A.; CHO, J. Effects of the magnetic field direction on the Tsallis statistic. **Monthly Notices of the Royal Astronomical Society**, v. 475, p. 3324–3330, Apr 2018. 3, 49

GOODMAN, A. A. The future of magnetic field mapping in the interstellar medium. In: HAAS, M. R.; DAVIDSON, J. A.; ERICKSON, E. F. (Ed.). **From gas to stars to dust**. [S.l.: s.n.], 1995. (Astronomical Society of the Pacific Conference Series, v. 73), p. 45–52. 30

GOODMAN, A. A.; BASTIEN, P.; MYERS, P. C.; MENARD, F. Optical polarization maps of star-forming regions in perseus, taurus, and ophiuchus. **Astrophysical Journal**, v. 359, p. 363, ago. 1990. 31

GOOSSENS, M. **An introduction to plasma astrophysics and magnetohydrodynamics**. [S.l.: s.n.], 2003. 7

GOVONI, F.; FERETTI, L. Magnetic fields in clusters of galaxies. **International Journal of Modern Physics D**, v. 13, n. 8, p. 1549–1594, jan. 2004. 29, 39

GREEN, J. A.; MCCLURE-GRIFFITHS, N. M.; CASWELL, J. L.; ROBISHAW, T.; HARVEY-SMITH, L. MAGMO: coherent magnetic fields in the star-forming regions of the Carina-Sagittarius spiral arm tangent. **Monthly Notices of the Royal Astronomical Society**, v. 425, n. 4, p. 2530–2547, Oct 2012. 3

GREENAWALT, B.; WALTERBOS, R.; BRAUN, R. Optical spectroscopy of diffuse ionized gas in m31. **The Astrophysical Journal**, v. 483, n. 2, p. 666, 1997. 29

GREENBERG, J. M.; MIDDLEHURST, B. M.; ALLER, L. H. **Nebulae and interstellar matter**. [S.l.: s.n.], 1968. 90

HALE, G. E. On the probable existence of a magnetic field in sun-spots. **The Astrophysical Journal**, v. 28, p. 315, nov. 1908. 37

HALL, J. S. Observations of the polarized light from stars. **Science**, v. 109, n. 2825, p. 166–167, fev. 1949. 31

HAN, J. L. Magnetic Fields in our galaxy: how much do we know? III. progress in the last decade. **Chinese Journal of Astronomy and Astrophysics Supplement**, v. 6, n. S2, p. 211–217, dez. 2006. 30

HARDCASTLE, M. J. Synchrotron and inverse-Compton emission from radio galaxies with non-uniform magnetic field and electron distributions. **Monthly Notices of the Royal Astronomical Society**, v. 433, n. 4, p. 3364–3372, ago. 2013. 39

HAVERKORN, M. Magnetic fields in the milky Way. In: LAZARIAN, A.; PINO, E. M. de G. D.; MELIOLI, C. (Ed.). **Magnetic fields in diffuse Media**. [S.l.: s.n.], 2015. v. 407, p. 483. 29, 39

HAVERKORN, M.; BROWN, J.; GAENSLER, B.; MCCLURE-GRIFFITHS, N. The outer scale of turbulence in the magnetoionized galactic interstellar medium. **The Astrophysical Journal**, v. 680, n. 1, p. 362, 2008. 50

HAVERKORN, M.; KATGERT, P.; BRUYN, A. G. de. Structure in the polarized Galactic synchrotron emission, in particular "depolarization canals". **Astronomy & Astrophysics**, v. 427, p. 549–559, Nov 2004. 50, 72

HAVERKORN, M.; SPANGLER, S. R. Plasma diagnostics of the interstellar medium with radio Astronomy. **Space Science Reviews**, v. 178, n. 2-4, p. 483–511, out. 2013. 39

HAWLEY, J. F.; STONE, J. M. Mocct: a numerical technique for astrophysical mhd. **Computer Physics Communications**, v. 89, n. 1-3, p. 127–148, 1995. 57

HAYES, J. C.; NORMAN, M. L.; FIEDLER, R. A.; BORDNER, J. O.; LI, P. S.; CLARK, S. E.; DOULA, A. ud; LOW, M.-M. M. Simulating radiating and magnetized flows in multiple dimensions with ZEUS-MP. **The Astrophysical Journal Supplement Series**, v. 165, n. 1, p. 188–228, jul. 2006. 61

HEALD, G.; BRAUN, R. Magnetic fields in nearby galaxies. In: INTERNATIONAL FUZZY SYSTEMS ASSOCIATION WORLD CONGRESS, 47., 2009, Netherlands, Holland. **Panoramic radio astronomy: wide-field 1-2**

GHz research on galaxy evolution. Netherlands: University of Groningen, 2009. p. 47. 29

HEILES, C. The local direction and curvature of the galactic magnetic field derived from starlight polarization. **The Astrophysical Journal**, v. 462, p. 316, May 1996. 3

HEILES, C.; HAVERKORN, M. Magnetic fields in the multiphase interstellar medium. **Space Science Reviews**, v. 166, n. 1-4, p. 293–305, 2012. 72

HEILES, C.; TROLAND, T. H. The millennium Arecibo 21 centimeter absorption-line survey. I. techniques and gaussian fits. **The Astrophysical Journal Supplement Series**, v. 145, n. 2, p. 329–354, abr. 2003. 28, 30

HEITSCH, F.; ZWEIBEL, E. G.; LOW, M.-M. M.; LI, P.; NORMAN, M. L. Magnetic field diagnostics based on far-infrared polarimetry: tests using numerical simulations. **The Astrophysical Journal**, v. 561, n. 2, p. 800–814, nov. 2001. 35

HELLINGER, P.; TRÁVNÍČEK, P. M.; ŠTVERÁK, Š.; MATTEINI, L.; VELLI, M. Proton thermal energetics in the solar wind: Helios reloaded. **Journal of Geophysical Research: Space Physics**, v. 118, n. 4, p. 1351–1365, 2013. 24

HENNEBELLE, P.; FALGARONE, E. Turbulent molecular clouds. **Astronomy and Astrophysics Reviews**, v. 20, p. 55, nov. 2012. 43

HERRON, C. A.; BURKHART, B.; GAENSLER, B. M.; LEWIS, G. F.; MCCLURE-GRIFFITHS, N. M.; BERNARDI, G.; CARRETTI, E.; HAVERKORN, M.; KESTEVEN, M.; POPPI, S.; STAVELEY-SMITH, L. Advanced diagnostics for the study of linearly polarized emission. II. application to diffuse interstellar radio synchrotron emission. **The Astrophysical Journal**, v. 855, p. 29, Mar 2018. 4, 52

HERRON, C. A.; GAENSLER, B. M.; LEWIS, G. F.; MCCLURE-GRIFFITHS, N. M. Advanced diagnostics for the study of linearly polarized emission. I: derivation. **The Astrophysical Journal**, v. 853, p. 9, Jan 2018. 4, 52

HERZBERG, G.; SPINKS, J. W. T. **Molecular spectra and molecular structure: diatomic molecules**. [S.l.]: Van Nostrand, 1950. 36

HEYER, M.; GONG, H.; OSTRIKER, E.; BRUNT, C. Magnetically aligned velocity anisotropy in the Taurus molecular cloud. **The Astrophysical Journal**, v. 680, p. 420–427, Jun 2008. 3

HEYER, M.; KRAWCZYK, C.; DUVAL, J.; JACKSON, J. M. Re-examining Larson's scaling relationships in Galactic molecular clouds. **The Astrophysical Journal**, v. 699, n. 2, p. 1092–1103, jul. 2009. 44

HEYER, M. H.; BRUNT, C. M. The universality of turbulence in Galactic molecular clouds. **The Astrophysical Journal**, v. 615, n. 1, p. L45–L48, nov. 2004. 44

HEYER, M. H.; SCHLOERB, F. P. Application of principal component analysis to large-scale spectral line imaging studies of the interstellar medium. **The Astrophysical Journal**, v. 475, p. 173–187, Jan 1997. 3, 49

HILL, A. S.; BENJAMIN, R. A.; KOWAL, G.; REYNOLDS, R. J.; HAFFNER, L. M.; LAZARIAN, A. The turbulent warm ionized medium: emission measure distribution and MHD simulations. **The Astrophysical Journal**, v. 686, p. 363–378, out. 2008. 2, 29, 69

HILLEBRANDT, W.; KUPKA, F. An introduction to turbulence. In: _____. **Interdisciplinary aspects of turbulence**. [S.l.: s.n.], 2009. v. 756, p. 1. 9

HILTNER, W. A. Polarization of light from distant stars by interstellar medium. **Science**, v. 109, p. 165, fev. 1949. 31

HO, K. W.; YUEN, K. H.; LEUNG, P. K.; LAZARIAN, A. A comparison between faraday tomography and synchrotron polarization gradients. **arXiv e-prints**, p. arXiv:1901.07731, Jan 2019. 5

HOCUK, S.; CAZAUX, S.; SPAANS, M.; CASELLI, P. How chemistry influences cloud structure, star formation, and the imf. **Monthly Notices of the Royal Astronomical Society**, v. 456, n. 3, p. 2586–2610, 2015. 28

HOERNER, S. von. Internal structure of globular clusters. **Astrophysical Journal**, v. 125, p. 451, mar. 1957. 1

HORBURY, T. S.; FORMAN, M.; OUGHTON, S. Anisotropic scaling of magnetohydrodynamic turbulence. **Physical Review Letters**, v. 101, n. 17, p. 175005, 2008. 25

HOUDE, M.; VAILLANCOURT, J. E.; HILDEBRAND, R. H.; CHITSAZZADEH, S.; KIRBY, L. Dispersion of magnetic fields in molecular clouds. II. **Astrophysical Journal**, v. 706, n. 2, p. 1504–1516, dez. 2009. 35

HOYLE, F.; ELLIS, G. On the existence of an ionized layer about the galactic plane. **Australian Journal of Physics**, v. 16, n. 1, p. 1–7, 1963. 29

HSIEH, C.-h.; HU, Y.; LAI, S.-P.; YUEN, K. H.; LIU, S.-Y.; HSIEH, I. T.; HO, K. W.; LAZARIAN, A. Tracing magnetic field morphology using the velocity gradient technique in the presence of CO self-absorption. **The Astrophysical Journal**, v. 873, n. 1, p. 16, Mar 2019. 4

HU, Y.; LAZARIAN, A. Probing three-dimensional magnetic fields: I – polarized dust emission. **arXiv e-prints**, p. arXiv:2203.09745, mar. 2022. xiv, 97

HU, Y.; YUEN, K. H.; LAZARIAN, A. Intensity gradients technique: synergy with velocity gradients and polarization studies. **arXiv e-prints**, p. arXiv:1908.09488, Aug 2019. 4, 95

HU, Y.; YUEN, K. H.; LAZARIAN, A.; FISSEL, L. M.; JONES, P. A.; CUNNINGHAM, M. R. Tracing multi-scale magnetic field structure using multiple chemical tracers in giant molecular clouds. **arXiv e-prints**, p. arXiv:1904.04391, Apr 2019. 4, 77, 95

HU, Y.; YUEN, K. H.; LAZARIAN, V.; HO, K. W.; BENJAMIN, R. A.; HILL, A. S.; LOCKMAN, F. J.; GOLDSMITH, P. F.; LAZARIAN, A. Magnetic field morphology in interstellar clouds with the velocity gradient technique. **Nature Astronomy**, v. 3, p. 776–782, Jun 2019. 4, 77

HUGHES, A.; MEIDT, S. E.; COLOMBO, D.; SCHINNERER, E.; PETY, J.; LEROY, A. K.; DOBBS, C. L.; GARCÍA-BURILLO, S.; THOMPSON, T. A.; DUMAS, G.; SCHUSTER, K. F.; KRAMER, C. A comparative study of giant molecular clouds in M51, M33, and the large magellanic cloud. **The Astrophysical Journal**, v. 779, n. 1, p. 46, dez. 2013. 45

HULL, C. L. H.; ZHANG, Q. Interferometric observations of magnetic fields in forming stars. **Frontiers in Astronomy and Space Sciences**, v. 6, p. 3, mar. 2019. 3

IACOBELLI, M. et al. Studying galactic interstellar turbulence through fluctuations in synchrotron emission-first lofar galactic foreground detection. **Astronomy & astrophysics**, v. 558, p. A72, 2013. 39, 47, 52

IROSHNIKOV, P. Turbulence of a conducting fluid in a strong magnetic field. **Soviet Astronomy**, v. 7, p. 566, 1964. 24

JACKSON, T.; WERNER, M.; GAUTIER T. N., I. A catalog of bright filamentary structures in the interstellar medium. **The Astrophysical Journal Supplement Series**, v. 149, n. 2, p. 365–373, dez. 2003. 1

KALBERLA, P. M. W.; KERP, J. The HI distribution of the milky way. **Annual Review of Astronomy Astrophysics**, v. 47, n. 1, p. 27–61, set. 2009. 44

KALBERLA, P. M. W.; MCCLURE-GRIFFITHS, N. M.; PISANO, D. J.; CALABRETTA, M. R.; FORD, H. A.; LOCKMAN, F. J.; STAVELEY-SMITH, L.; KERP, J.; WINKEL, B.; MURPHY, T.; NEWTON-MCGEE, K. GASS: the Parkes Galactic all-sky survey. II. stray-radiation correction and second data release. **Astronomy & Astrophysics**, v. 521, p. A17, out. 2010. 28

KASPI, V. M.; BELOBORODOV, A. M. Magnetars. **Annual Review of Astronomy and Astrophysics**, v. 55, n. 1, p. 261–301, ago. 2017. 29

KASTLER, A. The zeeman-effect and the intensity and polarization of resonance and fluorescence radiation. **Physica**, v. 12, n. 9-10, p. 619–626, 1946. 37

KLEIN, U.; GRAEVE, R. Multi-frequency radio continuum observations of dwarf irregular galaxies. **Astronomy & Astrophysics**, v. 161, p. 155–168, jun. 1986. 39

KLESSEN, R. S. The relation between interstellar turbulence and star formation. **arXiv preprint astro-ph/0402673**, 2004. 43

_____. Star formation in molecular clouds. In: CHARBONNEL, C.; MONTMERLE, T. (Ed.). **EAS publications series**. [S.l.: s.n.], 2011. (EAS publications series, v. 51), p. 133–167. 1

KOLMOGOROV, A. The local structure of turbulence in incompressible viscous fluid for very large reynolds' numbers. **Akademiia Nauk SSSR Doklady**, v. 30, p. 301–305, 1941. 1, 10, 11

KOTHES, R.; LANDECKER, T. L.; WILLIS, A. G. **The dynamic interstellar medium: a celebration of the canadian Galactic plane survey**. [S.l.: s.n.], 2010. 3

KOWAL, G.; FALCETA-GONÇALVES, D. A.; LAZARIAN, A. Turbulence in collisionless plasmas: statistical analysis from numerical simulations with pressure anisotropy. **New Journal of Physics**, v. 13, p. 053001, maio 2011. 57

KOWAL, G.; LAZARIAN, A.; BERESNYAK, A. Density fluctuations in mhd turbulence: spectra, intermittency, and topology. **The Astrophysical Journal**, v. 658, n. 1, p. 423, 2007. 44, 57, 68

KOWAL, G.; LAZARIAN, A.; VISHNIAC, E. T.; OTMIANOWSKA-MAZUR, K. Numerical tests of fast reconnection in weakly stochastic magnetic fields. **The Astrophysical Journal**, v. 700, n. 1, p. 63–85, jul. 2009. 49, 57

KOWAL, G.; PINO, E. M. d. G. D.; LAZARIAN, A. Particle acceleration in turbulence and weakly stochastic reconnection. **Physical Review Letters**, v. 108, n. 24, p. 241102, 2012. 57

KRAICHNAN, R. H. Inertial-range spectrum of hydromagnetic turbulence. **The Physics of Fluids**, v. 8, n. 7, p. 1385–1387, 1965. 24

KRITSUK, A. G.; NORDLUND, r.; COLLINS, D.; PADOAN, P.; NORMAN, M. L.; ABEL, T.; BANERJEE, R.; FEDERRATH, C.; FLOCK, M.; LEE, D.; LI, P. S.; MÜLLER, W.-C.; TEYSSIER, R.; USTYUGOV, S. D.; VOGEL, C.; XU, H. Comparing numerical methods for isothermal magnetized supersonic turbulence. **The Astrophysical Journal**, v. 737, n. 1, p. 13, ago. 2011. 58

KRITSUK, A. G.; USTYUGOV, S. D.; L., N. M. The structure and statistics of interstellar turbulence. **New Journal of Physics**, v. 19, n. 6, p. 065003, jun. 2017. 43

KRUMHOLZ, M. R.; BURKHART, B. Is turbulence in the interstellar medium driven by feedback or gravity? an observational test. **Monthly Notices of the Royal Astronomical Society**, v. 458, n. 2, p. 1671–1677, maio 2016. 48

KULESZA-ŻYDZIK, B.; KULPA-DYBEŁ, K.; OTMIANOWSKA-MAZUR, K.; KOWAL, G.; SOIDA, M. Formation of gaseous arms in barred galaxies with dynamically important magnetic field: 3d mhd simulations. **Astronomy & Astrophysics**, v. 498, n. 2, p. L21–L24, 2009. 57

KULPA-DYBEŁ, K.; OTMIANOWSKA-MAZUR, K.; KULESZA-ŻYDZIK, B.; HANASZ, M.; KOWAL, G.; WÓLTAŃSKI, D.; KOWALIK, K. Global simulations of the magnetic field evolution in barred galaxies under the influence of the cosmic-ray-driven dynamo. **The Astrophysical Journal Letters**, v. 733, n. 2, p. L18, 2011. 57

KULSRUD, R. M. **Plasma physics for astrophysics**. [S.l.: s.n.], 2004. 13

KULSRUD, R. M.; ZWEIBEL, E. G. On the origin of cosmic magnetic fields. **Reports on Progress in Physics**, v. 71, n. 4, p. 046901, 2008. 22

LADA, E. A.; II, N. J. E.; FALGARONE, E. Physical properties of molecular cloud cores in l1630 and implications for star formation. **The Astrophysical Journal**, v. 488, n. 1, p. 286, 1997. 29

LANDAU, L. D.; LIFSHITZ, E. M. **Fluid mechanics**. [S.l.: s.n.], 1959. 1, 7, 9

LARSON, R. B. Turbulence and star formation in molecular clouds. **Monthly Notices of the Royal Astronomical Society**, v. 194, n. 4, p. 809–826, 1981. 12, 44

LAZARIAN, A. Astrophysical Implications of Turbulent Reconnection: from cosmic rays to star formation. In: PINO, E. M. de Gouveia dal; LUGONES, G.; Lazarian, A. (Ed.). **Magnetic fields in the universe: from laboratory and stars to primordial structures.** [S.l.: s.n.], 2005. (American Institute of Physics Conference Series, v. 784), p. 42–53. 22

LAZARIAN, A.; HOANG, T. Radiative torques: analytical model and basic properties. **Monthly Notices of the Royal Astronomical Society**, v. 378, p. 910–946, jul. 2007. 49

LAZARIAN, A.; POGOSYAN, D. Velocity modification of the power spectrum from an absorbing medium. **The Astrophysical Journal**, v. 616, p. 943–965, dez. 2004. 3, 49

_____. Studying turbulence using doppler-broadened lines: velocity coordinate spectrum. **The Astrophysical Journal**, v. 652, p. 1348–1365, dez. 2006. 2, 3, 22, 32

_____. Statistical description of synchrotron intensity fluctuations: studies of astrophysical magnetic turbulence. **The Astrophysical Journal**, v. 747, p. 5, mar. 2012. 3, 4, 47, 50, 71

_____. Spectrum and anisotropy of turbulence from multi-frequency measurement of synchrotron polarization. **The Astrophysical Journal**, v. 818, n. 2, p. 178, 2016. 4, 49, 50, 55

LAZARIAN, A.; PRUNET, S. Polarized microwave emission from dust. In: CECCHINI, S.; CORTIGLIONI, S.; SAULT, R.; SBARRA, C. (Ed.). **Astrophysical polarized backgrounds**. [S.l.: s.n.], 2002. (American Institute of Physics Conference Series, v. 609), p. 32–43. 31, 33

LAZARIAN, A.; VISHNIAC, E. T. Reconnection in a weakly stochastic field. **The Astrophysical Journal**, v. 517, n. 2, p. 700–718, Jun 1999. 53, 54

LAZARIAN, A.; YUEN, K. H. Gradients of synchrotron polarization: tracing 3d distribution of magnetic fields. **The Astrophysical Journal**, v. 865, n. 1, p. 59, 2018. xiv, 5, 53, 56, 68, 74, 76, 77, 96, 97

LAZARIAN, A.; YUEN, K. H.; HO. 30, 53, 56, 74

LAZARIAN, A.; YUEN, K. H.; LEE, H.; CHO, J. Synchrotron intensity gradients as tracers of interstellar magnetic fields. **The Astrophysical Journal**, v. 842, p. 30, Jun 2017. 4, 30, 53, 56, 68, 74, 75, 77, 90

LEAL, L. G. Particle motions in a viscous fluid. **Annual Review of Fluid Mechanics**, v. 12, p. 435–476, jan. 1980. 8

LEE, H.; LAZARIAN, A.; CHO, J. Polarimetric studies of magnetic turbulence with an interferometer. **The Astrophysical Journal**, v. 831, p. 77, Nov 2016. 51, 74

LEER, B. van. Towards the ultimate conservative difference Scheme. IV. a new approach to numerical convection. **Journal of Computational Physics**, v. 23, p. 276, mar. 1977. 58

LEQUEUX, J. **The interstellar medium**. [S.l.: s.n.], 2005. 30

LESIEUR, M. Turbulence in fluids: stochastic and numerical modelling. **NASA STI/Recon Technical Report A**, v. 87, p. 50635, jun. 1987. 9

LI, H.-b.; DOWELL, C. D.; GOODMAN, A.; HILDEBRAND, R.; NOVAK, G. Anchoring magnetic field in turbulent molecular clouds. **The Astrophysical Journal**, v. 704, p. 891–897, out. 2009. 32, 34

MADSEN, G. J.; REYNOLDS, R. J.; HAFFNER, L. M. A multiwavelength optical emission line survey of warm ionized gas in the Galaxy. **The Astrophysical Journal**, v. 652, n. 1, p. 401–425, nov. 2006. 29

MAGUIRE, C. A.; CARLEY, E. P.; MCCAULEY, J.; GALLAGHER, P. T. Evolution of the Alfvén Mach number associated with a coronal mass ejection shock. **Astronomy Astrophysics**, v. 633, p. A56, jan. 2020. 5

MAGYAR, N.; DOORSSELAERE, T. V.; GOOSSENS, M. The Nature of Elsässer variables in compressible MHD. **The Astrophysical Journal**, v. 873, n. 1, p. 56, mar. 2019. 22

MAKARENKO, I.; BUSHBY, P.; FLETCHER, A.; HENDERSON, R.; MAKARENKO, N.; SHUKUROV, A. Topological data analysis and diagnostics of compressible magnetohydrodynamic turbulence. **Journal of Plasma Physics**, v. 84, n. 4, p. 735840403, ago. 2018. 49

MAO, S.; ZWEIBEL, E.; FLETCHER, A.; OTT, J.; TABATABAEI, F. Properties of the magneto-ionic medium in the halo of m51 revealed by wide-band polarimetry. **arXiv preprint arXiv:1412.8320**, 2014. 3

MAO, S. A.; MCCLURE-GRIFFITHS, N. M.; GAENSLER, B. M.; BROWN, J. C.; ECK, C. L. van; HAVERKORN, M.; KRONBERG, P. P.; STIL, J. M.; SHUKUROV, A.; TAYLOR, A. R. New constraints on the Galactic halo magnetic field using rotation measures of extragalactic Sources toward the Outer Galaxy. **The Astrophysical Journal**, v. 755, n. 1, p. 21, Aug 2012. 3

MARON, J.; GOLDREICH, P. Simulations of incompressible magnetohydrodynamic turbulence. **The Astrophysical Journal**, v. 554, p. 1175–1196, jun. 2001. 25

MARSCH, E.; MANGENEY, A. Ideal MHD equations in terms of compressive Elsaesser variables. **Journal of Geophysical Research**, v. 92, p. 7363–7367, jul. 1987. 21

MATHIEU, J.; SCOTT, J. **An introduction to turbulent flow**. [S.l.: s.n.], 2000. 8

MATTHAEUS, W. H.; GOLDSTEIN, M. L. Measurement of the rugged invariants of magnetohydrodynamic turbulence in the solar wind. **Journal of Geophysical Research: Space Physics**, v. 87, n. A8, p. 6011–6028, 1982. 24

MATTHAEUS, W. H.; ZANK, G. P.; SMITH, C. W.; OUGHTON, S. Turbulence, spatial transport, and heating of the solar wind. **Physical Review Letters**, v. 82, n. 17, p. 3444, 1999. 24

MCCLURE-GRIFFITHS, N. M.; GREEN, A. J.; DICKEY, J. M.; GAENSLE, B. M.; HAYNES, R. F.; WIERINGA, M. H. The southern galactic plane survey: the test region. **The Astrophysical Journal**, v. 551, n. 1, p. 394–412, abr. 2001. 51

MCCOMB, W. D. **The physics of fluid turbulence**. [S.l.: s.n.], 1990. 7

MCKEE, C. F.; OSTRIKER, E. C. Theory of Star Formation. **Annual Review of Astronomy and Astrophysics**, v. 45, p. 565–687, set. 2007. 2, 27

MCKEE, C. F.; OSTRIKER, J. P. A theory of the interstellar medium: three components regulated by supernova explosions in an inhomogeneous substrate. **The Astrophysical Journal**, v. 218, p. 148–169, Nov 1977. 27

MIYOSHI, T.; KUSANO, K. A multi-state HLL approximate Riemann solver for ideal magnetohydrodynamics. **Journal of Computational Physics**, v. 208, n. 1, p. 315–344, set. 2005. 58, 66, 67

MO, H.; BOSCH, F. C. van den; WHITE, S. **Galaxy formation and evolution**. [S.l.: s.n.], 2010. 2, 27

MONIN, A. S.; YAGLOM, A. M.; ABLOW, C. M. Statistical fluid mechanics: the mechanics of turbulence. **American Journal of Physics**, v. 45, n. 10, p. 1010–1010, out. 1977. 13

MÜLLER, W.-C.; BUSSE, A. Recent developments in the theory of magnetohydrodynamic turbulence. In: SHAIKH, D.; ZANK, G. P. (Ed.). **Turbulence and nonlinear processes in astrophysical plasmas**. [S.l.: s.n.], 2007. (American Institute of Physics Conference Series, v. 932), p. 52–57. 22

NG, C.; BHATTACHARJEE, A.; MUNSI, D.; ISENBERG, P.; SMITH, C. Kolmogorov versus iroshnikov-kraichnan spectra: consequences for ion heating in the solar wind. **Journal of Geophysical Research: Space Physics**, v. 115, n. A2, 2010. 24

NORMAN, M.; WILSON, J.; BARTON, R. A new calculation on rotating protostar collapse. **The Astrophysical Journal**, v. 239, p. 968–981, 1980. 57, 68

OBEROI, D.; LONSDALE, C. J. **Radio Science**, v. 47, n. 6, p. RS0K08, dez. 2012. 41

ORKISZ, J. H.; PETY, J.; GERIN, M.; BRON, E.; GUZMÁN, V. V.; BARDEAU, S.; GOICOECHEA, J. R.; GRATIER, P.; PETIT, F. L.; LEVRIER, F.; LISZT, H.; ÖBERG, K.; PERETTO, N.; ROUEFF, E.; SIEVERS, A.; TREMBLIN, P. Turbulence and star formation efficiency in molecular clouds: solenoidal versus compressive motions in Orion B. **Astronomy and Astrophysics**, v. 599, p. A99, mar. 2017. 2

OSSENKOPF, V.; KRIPS, M.; STUTZKI, J. Structure analysis of interstellar clouds. I. improving the Δ-variance method. **Astronomy & Astrophysics.**, v. 485, p. 917–929, Jul 2008. 3, 49

OSTRIKER, E. C. Developing diagnostics of molecular clouds using numerical MHD simulations. In: FALGARONE, E.; PASSOT, T. (Ed.). **Turbulence and magnetic fields in astrophysics**. [S.l.: s.n.], 2003. (Lecture Notes in Physics, Berlin Springer Verlag, v. 614), p. 252–270. 35

PADOAN, P.; NORDLUND, Å. A super-alfvénic model of dark clouds. **The Astrophysical Journal**, v. 526, n. 1, p. 279, 1999. 43

PARKER, E. N. Magnetic fields in the cosmos. **Scientific American**, v. 249, p. 44–54, ago. 1983. 13

PEREYRA, A.; MAGALHÃES, A. M. Polarimetry toward the Musca dark cloud. I. the catalog. **The Astrophysical Journal**, v. 603, n. 2, p. 584–594, mar. 2004. xii, 47

PEWSEY, A.; NEUHÄUSER, M.; RUXTON, G. D. **Circular statistics in R**. [S.l.]: Oxford University Press, 2013. 82

PEZZI, O.; PARASHAR, T.; SERVIDIO, S.; VALENTINI, F.; VASCONEZ, C.; YANG, Y.; MALARA, F.; MATTHAEUS, W.; VELTRI, P. Colliding alfv\'enic wave packets in mhd, hall and kinetic simulations. **arXiv preprint arXiv:1702.01030**, 2017. 24

PFROMMER, C.; DURSI, L. J. Detecting the orientation of magnetic fields in galaxy clusters. **Nature Physics**, v. 6, n. 7, p. 520–526, jul. 2010. 39

PINO, E. d. G. D.; FALCETA-GONÇALVES, D.; GALLAGHER, J.; MELIOLI, C.; D'ERCOLE, A.; BRIGHENTI, F. The role of sn-driven turbulence on the formation of outflows, inflows and cooling flows: from galaxies to clusters of galaxies. **Proceedings of the International Astronomical Union**, v. 5, n. H15, p. 452–453, 2009. 57

PROSEKIN, A. Y.; KELNER, S. R.; AHARONIAN, F. A. Polarization of radiation of electrons in highly turbulent magnetic fields. **Physical Review D**, v. 94, n. 6, p. 063010, set. 2016. 47

PURCELL, E. M. Suprathermal rotation of interstellar grains. **Astrophysical Journal**, v. 231, p. 404–416, jul. 1979. 32

PUZZARINI, C. Prebiotic molecules in interstellar space: rotational spectroscopy and quantum chemistry. In: SALAMA, F.; LINNARTZ, H. (Ed.). **Laboratory astrophysics: from observations to interpretation**. [S.l.: s.n.], 2020. v. 350, p. 65–70. 27

PYNZAR', A. V. The electron density in clouds of turbulent interstellar plasma. **Astronomy Reports**, v. 60, n. 3, p. 332–343, mar. 2016. 70

RAMOS, A. A.; BUENO, J. T. Theory and modeling of the zeeman and paschen-back effects in molecular lines. **The Astrophysical Journal**, v. 636, n. 1, p. 548, 2006. 37

RAO, R.; CRUTCHER, R. M.; PLAMBECK, R. L.; WRIGHT, M. C. H. High-resolution millimeter-wave mapping of linearly polarized dust emission: magnetic field structure in orion. **Astrophysical Journal Letter**, v. 502, n. 1, p. L75–L78, jul. 1998. 32

REYNOLDS, R.; HAFFNER, L.; TUFTE, S. Evidence for an additional heat source in the warm ionized medium of galaxies. **The Astrophysical Journal Letters**, v. 525, n. 1, p. L21, 1999. 29

RICHARDSON, L. F. **Weather prediction by numerical process, first edition**. [S.l.]: Cambridge University Press, 1922. 10

ROBERGE, W. G.; JONES, D.; LEPP, S.; DALGARNO, A. Interstellar photodissociation and photoionization rates. **The Astrophysical Journal Letter**, v. 77, p. 287, out. 1991. 28

ROHLFS, K.; WILSON, T. L. **Tools of radio astronomy**. [S.l.]: Springer Science & Business Media, 2013. 27

ROMAN-DUVAL, J.; FEDERRATH, C.; BRUNT, C.; HEYER, M.; JACKSON, J.; KLESSEN, R. S. The turbulence spectrum of molecular clouds in the Galactic ring survey: a density-dependent principal component analysis calibration. **The Astrophysical Journal,**, v. 740, n. 2, p. 120, out. 2011. 44

RYAN, S. G. Big bang nucleosynthesis, polulation iii, and stellar genetics in the galactic halo. **Publications of the Astronomical Society of Australia**, v. 19, n. 2, p. 238–245, 2002. 27

RYBICKI, G. B.; LIGHTMAN, A. P. **Radiative processes in astrophysics**. [S.l.: s.n.], 1979. 39, 72

SAIKIA, D. J.; SALTER, C. J. Polarization properties of extragalactic radio sources. **Annual Review of Astronomy and Astrophysics**, v. 26, p. 93–144, jan. 1988. 41

SALVATIER, J.; WIECKI, T. V.; FONNESBECK, C. Probabilistic programming in python using pymc3. **PeerJ Computer Science**, v. 2, p. e55, abr. 2016. ISSN 2376-5992. Disponível em: <https://doi.org/10.7717/peerj-cs.55>. 80

SANTOS-LIMA, R.; PINO, E. d. G. D.; LAZARIAN, A. The role of turbulent magnetic reconnection in the formation of rotationally supported protostellar disks. **The Astrophysical Journal**, v. 747, n. 1, p. 21, 2012. 57

SCALO, J.; ELMEGREEN, B. G. Interstellar turbulence II: implications and effects. **Annual Review of Astronomy and Astrophysics**, v. 42, n. 1, p. 275–316, set. 2004. 43

SCHEKOCHIHIN, A. A.; COWLEY, S. C. Turbulence and magnetic fields in astrophysical plasmas. In: _____. **Magnetohydrodynamics: historical evolution and Trends**. [S.l.: s.n.], 2007. p. 85. 7, 46

SCHMIDT, W.; FEDERRATH, C.; HUPP, M.; KERN, S.; NIEMEYER, J. C. Numerical simulations of compressively driven interstellar turbulence. I. isothermal gas. **Astronomy and Astrophysicss**, v. 494, n. 1, p. 127–145, jan. 2009. 43

SCHNEIDER, N.; OSSENKOPF, V.; CSENGERI, T.; KLESSEN, R. S.; FEDERRATH, C.; TREMBLIN, P.; GIRICHIDIS, P.; BONTEMPS, S.; ANDRÉ, P. Understanding star formation in molecular clouds-i. effects of line-of-sight contamination on the column density structure. **Astronomy & Astrophysics**, EDP Sciences, v. 575, p. A79, 2015. 44, 45

SCHWABL, F. **Advanced quantum mechanics**. [S.l.]: Springer Science & Business Media, 2005. 37

SEATON, M. The chemical composition of the interstellar gas. **Monthly Notices of the Royal Astronomical Society**, v. 111, n. 4, p. 368–376, 1951. 27

SHAIKH, D.; ZANK, G. P. The turbulent density spectrum in the solar wind plasma. **Monthly Notices of the Royal Astronomical Society**, v. 402, n. 1, p. 362–370, fev. 2010. 12

SHARMA, S. Markov chain monte carlo methods for bayesian data analysis in astronomy. **Annual Review of Astronomy and Astrophysics**, v. 55, n. 1, p. 213–259, ago. 2017. 79, 80

SHETTY, R.; BEAUMONT, C. N.; BURTON, M. G.; KELLY, B. C.; KLESSEN, R. S. The linewidth-size relationship in the dense interstellar medium of the

Central Molecular Zone. **Monthly Notices of the Royal Astronomical Society**, v. 425, n. 1, p. 720–729, set. 2012. 45

SHU, F. H. Self-similar collapse of isothermal spheres and star formation. **Astrophysical Journal**, v. 214, p. 488–497, jun. 1977. 50

SHUKUROV, A. Mesoscale magnetic structures in spiral galaxies. In: _____. **Cosmic magnetic fields**. [S.l.: s.n.], 2005. v. 664, p. 113. 39

SOLER, J. D.; HENNEBELLE, P.; MARTIN, P. G.; MIVILLE-DESCHÊNES, M. A.; NETTERFIELD, C. B.; FISSEL, L. M. An imprint of molecular cloud magnetization in the morphology of the dust polarized emission. **The Astrophysical Journal**, v. 774, n. 2, p. 128, Sep 2013. 4, 55, 75, 76

SOLOMON, P. M.; RIVOLO, A. R.; BARRETT, J.; YAHIL, A. Mass, luminosity, and line width relations of Galactic molecular clouds. **Astrophysical Journal**, v. 319, p. 730, ago. 1987. 44

SOMOV, B. V. **Plasma astrophysics, part I: fundamentals and practice**. [S.l.: s.n.], 2006. 7

SPITZER, L. **Physical processes in the interstellar medium**. [S.l.: s.n.], 1978. 41

SPITZER LYMAN, J.; TUKEY, J. W. A Theory of interstellar polarization. **Astrophysical Journal**, v. 114, p. 187, set. 1951. 32

SRIDHAR, S. Magnetohydrodynamic turbulence in a strongly magnetised plasma. **Astronomische Nachrichten**, v. 331, n. 1, p. 93–100, 2010. 22

SRINIVASAN, S. K. Theory of turbulence. **Zeitschrift fur Physik**, v. 205, n. 3, p. 221–225, jun. 1967. 9

STARK, A. A. Kinematics of molecular clouds.I. velocity dispersion in the solar neighborhood. **The Astrophysical Journal**, v. 281, p. 624–633, jun. 1984. 44

STONE, J. M. **Radiation and optics**. [S.l.: s.n.], 1963. 41

STONE, J. M.; GARDINER, T. A.; TEUBEN, P.; HAWLEY, J. F.; SIMON, J. B. Athena: a new code for astrophysical MHD. **Astrophysical Journal Supplement**, v. 178, n. 1, p. 137–177, set. 2008. 59

STONE, J. M.; MIHALAS, D.; NORMAN, M. L. ZEUS-2D: A radiation magnetohydrodynamics code for astrophysical flows in two space dimensions. III. the radiation hydrodynamic algorithms and tests. **Astrophysical Journal Supplement**, v. 80, p. 819, jun. 1992. 57

STONE, J. M.; NORMAN, M. L. ZEUS-2D: A radiation magnetohydrodynamics code for astrophysical flows in two space dimensions. I. the hydrodynamic algorithms and tests. **Astrophysical Journal Supplement**, v. 80, p. 753, jun. 1992. 57, 58

_____. ZEUS-2D: A radiation magnetohydrodynamics code for astrophysical flows in two space dimensions. II. the magnetohydrodynamic algorithms and tests. **Astrophysical Journal Supplement**, v. 80, p. 791, jun. 1992. 57, 58

STUTZKI, J.; BENSCH, F.; HEITHAUSEN, A.; OSSENKOPF, V.; ZIELINSKY, M. On the fractal structure of molecular clouds. **Astronomy and Astrophysics**, v. 336, p. 697–720, ago. 1998. 3, 49

TABATABAEI, F. S.; BECK, R.; KRÜGEL, E.; KRAUSE, M.; BERKHUIJSEN, E. M.; GORDON, K. D.; MENTEN, K. M. High-resolution radio continuum survey of M 33. II. thermal and nonthermal emission. **Astronomy and Astrophysics**, v. 475, n. 1, p. 133–143, nov. 2007. 39

TAUBER, J. A.; GOLDSMITH, P. F.; DICKMAN, R. L. The smoothness of CO line profiles in Orion: implications for clumpiness. **The Astrophysical Journal**, v. 375, p. 635, jul. 1991. 48

TIELENS, A. G. G. M. **The physics and chemistry of the interstellar medium**. [S.l.: s.n.], 2005. 27

TOBIAS, S. M.; CATTANEO, F.; BOLDYREV, S. MHD Dynamos and turbulence. **ArXiv e-prints**, mar. 2011. 22

TOFFLEMIRE, B. M.; BURKHART, B.; LAZARIAN, A. Interstellar sonic and alfvénic mach numbers and the tsallis distribution. **The Astrophysical Journal**, v. 736, n. 1, p. 60, jul. 2011. 5, 48, 49

TORO, E. F. **Riemann solvers and numerical methods for fluid dynamics: a practical introduction**. [S.l.]: Springer Science & Business Media, 2013. 58, 60, 65, 67

TREUMANN, R. A.; BAUMJOHANN, W.; NARITA, Y. On the ion-inertial-range density-power spectra in solar wind turbulence. **Annales Geophysicae**, v. 37, n. 2, p. 183–199, abr. 2019. 12

TRIPPE, S. [Review] Polarization and polarimetry. **Journal of Korean Astronomical Society**, v. 47, n. 1, p. 15–39, fev. 2014. 41

TRITTON, D. J. **Physical fluid dynamics**. [S.l.: s.n.], 1988. 8

VELLI, M.; GRAPPIN, R.; MANGENEY, A. Turbulent cascade of incompressible unidirectional alfvén waves in the interplanetary medium. **Physical Review Letters**, v. 63, n. 17, p. 1807, 1989. 24

VINK, J.; LAMING, J. M. On the magnetic fields and particle acceleration in Cassiopeia A. **The Astrophysical Journal**, v. 584, n. 2, p. 758–769, fev. 2003. 39

WAELKENS, A.; SCHEKOCHIHIN, A.; ENSSLIN, T. Probing magnetic turbulence by synchrotron polarimetry: statistics and structure of magnetic fields from stokes correlators. **Monthly Notices of the Royal Astronomical Society**, v. 398, n. 4, p. 1970–1988, 2009. 72, 74

WEIZSÄCKER, C. F. von. The evolution of galaxies and stars. **The Astrophysical Journal**, v. 114, p. 165, set. 1951. 1

_____. _____. **The Astrophysical Journal**, v. 114, p. 165, set. 1951. 42

WHITTET, D. i. The observed properties of interstellar dust in the infrared. **Dust in the universe**, p. 25–53, 1988. 27

WIELEBINSKI, R. Magnetic fields in the milky way, derived from radio continuum observations and faraday rotation Studies. In: _____. **Cosmic magnetic fields**. [S.l.: s.n.], 2005. v. 664, p. 89. 39

WIMMER-SCHWEINGRUBER, R. In-situ investigation of the interstellar medium. In: **COSPAR SCIENTIFIC ASSEMBLY, 42.,**. [S.l.: s.n.], 2018. v. 42, p. PIR.1–32–18. 29

WOLFIRE, M. G.; CASSINELLI, J. P. The temperature structure in accretion flows onto massive protostars. **The Astrophysical Journal**, v. 310, p. 207, nov. 1986. 28

WOLFIRE, M. G.; MCKEE, C. F.; HOLLENBACH, D.; TIELENS, A. G. G. M. Neutral atomic phases of the interstellar medium in the Galaxy. **The Astrophysical Journal**, v. 587, n. 1, p. 278–311, abr. 2003. 28

WOLLEBEN, M.; FLETCHER, A.; LANDECKER, T. L.; CARRETTI, E.; DICKEY, J. M.; GAENSLER, B. M.; HAVERKORN, M.; MCCLURE-GRIFFITHS, N.; REICH, W.; TAYLOR, A. R. Antisymmetry in the faraday rotation sky caused by a nearby magnetized bubble. **The Astrophysical Journal Letter**, v. 724, n. 1, p. L48–L52, Nov 2010. 3

WOOD, K.; MATHIS, J. S. Monte Carlo photoionization simulations of diffuse ionized gas. **Monthly Notices of the Royal Astronomical Society**, v. 353, n. 4, p. 1126–1134, out. 2004. 29

WU, Q.; KIM, J.; RYU, D. Magnetic field and faraday rotation measure in a turbulent warm ionized medium. **Nature**, v. 34, p. 21–26, jan. 2015. 3

YUEN, K. H.; LAZARIAN, A. Tracing interstellar magnetic field using velocity gradient technique: application to atomic hydrogen data. **The Astrophysical Journal Letters**, v. 837, n. 2, p. L24, 2017. 68, 76, 77, 81, 96

ZEEMAN, P. On the influence of magnetism on the nature of the light emitted by a substance. **Astrophysical Jornal**, v. 5, p. 332, maio 1897. 36

ZHANG, J.-F.; LAZARIAN, A.; HO, K. W.; YUEN, K. H.; YANG, B.; HU, Y. Tracing magnetic field with synchrotron polarization gradients: parameter study. **Monthly Notices of the Royal Astronomical Society**, v. 486, n. 4, p. 4813–4822, jul. 2019. 4, 77, 88, 90, 95, 96

ZHANG, J.-F.; LAZARIAN, A.; LEE, H.; CHO, J. Studying magnetohydrodynamic turbulence with synchrotron polarization dispersion. **The Astrophysical Journal**, v. 825, p. 154, Jul 2016. 51, 72

ZHANG, J.-F.; LIU, Q.; LAZARIAN, A. Tracing magnetic fields by the synergies of synchrotron emission gradients. **The Astrophysical Journal**, v. 886, n. 1, p. 63, nov. 2019. 95

PUBLICAÇÕES TÉCNICO-CIENTÍFICAS EDITADAS PELO INPE

Teses e Dissertações (TDI)

Teses e Dissertações apresentadas nos Cursos de Pós-Graduação do INPE.

Notas Técnico-Científicas (NTC)

Incluem resultados preliminares de pesquisa, descrição de equipamentos, descrição e ou documentação de programas de computador, descrição de sistemas e experimentos, apresentação de testes, dados, atlas, e documentação de projetos de engenharia.

Propostas e Relatórios de Projetos (PRP)

São propostas de projetos técnico-científicos e relatórios de acompanhamento de projetos, atividades e convênios.

Publicações Seriadas

São os seriados técnico-científicos: boletins, periódicos, anuários e anais de eventos (simpósios e congressos). Constam destas publicações o Internacional Standard Serial Number (ISSN), que é um código único e definitivo para identificação de títulos de seriados.

Pré-publicações (PRE)

Todos os artigos publicados em periódicos, anais e como capítulos de livros.

Manuais Técnicos (MAN)

São publicações de caráter técnico que incluem normas, procedimentos, instruções e orientações.

Relatórios de Pesquisa (RPQ)

Reportam resultados ou progressos de pesquisas tanto de natureza técnica quanto científica, cujo nível seja compatível com o de uma publicação em periódico nacional ou internacional.

Publicações Didáticas (PUD)

Incluem apostilas, notas de aula e manuais didáticos.

Programas de Computador (PDC)

São a seqüência de instruções ou códigos, expressos em uma linguagem de programação compilada ou interpretada, a ser executada por um computador para alcançar um determinado objetivo. Aceitam-se tanto programas fonte quanto os executáveis.